Long-Term Monitoring and Evaluation of the Varina-Enon Bridge

Ankuj Dahiya

Thesis submitted to the faculty of the Virginia Polytechnic Institute and State University in partial fulfillment of the requirements for the degree of

Master of Science
In
Civil Engineering

Carin L. Roberts-Wollman, Chair
Iaonnis Koutromanos
Rodrigo Sarlo

February 19, 2021
Blacksburg, Virginia

Keywords: Post-tensioned concrete, Prestress loss, Varina-Enon Bridge, Finite element modeling, Creep, Shrinkage, Thermal gradient

Long-Term Monitoring and Evaluation of the Varina-Enon Bridge.

Ankuj Dahiya

ACADEMIC ABSTRACT

To make sound decisions about the remaining life of a structure, the precise calculation of the prestress losses is very important. In post-tensioned structures, the prestress losses due to creep and shrinkage can cause serviceability issues and can reduce flexural capacity.

The Varina-Enon Bridge is a cable-stayed, precast, segmental, post-tensioned box girder bridge located in Richmond, Virginia. Observation of flexural cracks in the bridge by inspectors promoted a study regarding long-term prestress losses in the structure. For understanding and sustaining the structure throughout its remaining service life, accurately quantifying prestress losses is important.

Two approaches are used to predict long-term prestress losses on the Varina-Enon Bridge. The first approach involves a finite element computer model of the bridge which run a time-dependent staged-construction analysis to obtain predicted prestress losses using the CEB-FIP ’90 code expressions for creep and shrinkage. The second approach involves the compilation of data from instrumentation mounted in the bridge to back calculate the effective prestress force.

The analysis using the computer model predicted the prestress losses as 44.6 ksi in Span 5, 47.9 ksi in Span 6, 45.3 ksi in Span 9, and 45.9 ksi in Span 11. The prestress losses estimated from field data were 50.0 ksi in Span 5, 48.0 ksi in Span 6, 46.7 ksi in Span 9, and 49.1 ksi in Span 11. It can be seen that relative to the results of field data estimations, the finite element analyses underestimated prestress loss, but given the degree of uncertainty in each form of estimation, the results are considered to fit well.

Long-Term Monitoring and Evaluation of the Varina-Enon Bridge.

Ankuj Dahiya

GENERAL AUDIENCE ABSTRACT

In order to apply a precompression force to concrete structures, post-tensioned concrete employs stressed steel strands. To construct lighter, stiffer structures, this popular building technology can be used. The steel strands undergo a reduction in force known as prestress losses over time. To make good decisions about the remaining life of a structure, the precise calculation of the prestress losses is very important.

The Varina-Enon Bridge is a post-tensioned concrete box-girder bridge in Richmond Virginia. In July of 2012, observation of flexural cracks in the bridge by the inspectors promoted a study regarding long-term prestress losses in the structure. Two techniques are used to predict long-term prestress losses for this bridge. A computer model of the bridge is used in the first method to calculate losses using the design code. In order to measure prestress losses, the second technique used data from sensors mounted on the bridge.

It was found that the estimation of losses closely matched those predicted at the time of the bridge construction and the computer model results. Based on this the final conclusion is made that the prestress loss in the Varina-Enon Bridge is not significantly more than expected.

ACKNOWLEDGEMENTS

I would like to provide my sincere acknowledgement to my committee members for continued support and encouragement: Dr. Roberts-Wollman, my committee chair; Dr. Koutromanos; and Dr. Rodrigo Sarlo. Thanks a lot for providing all the learning opportunities during the course of project. I would also like to thank VDOT for their support during the project. I would like to thank the Virginia Department of Transportation for their support on this project, including providing documentation regarding the design and construction of the Varina-Enon Bridge. Thank you to Rachel Brodsky also, whose previous work, thesis, and guidance helped a lot during the project.

My deepest gratitude to my ever-supportive roommate Chirag also who helped me during the rough times. Finally, thanks to my family also to support me during these unprecedented times.

TABLE OF CONTENTS

TABLE OF CONTENTS v
LIST OF FIGURES vii
LIST OF TABLES ix
Chapter 1. Introduction 1
1.1 Motivation 1
1.2 Varina-Enon Bridge Overview 1
1.2.1 Project Background 5
1.3 Purpose and Scope 5
Chapter 2. Literature Review 7
2.1 Computer Modeling 8
2.1.1 Veterans' City Glass Skyway Modeling 9
2.1.2 Varina-Enon Bridge Modeling 9
2.2 Creep and Shrinkage 10
2.2.1 Sunshine Skyway Bridge Creep and Shrinkage Models 11
2.2.2 Varina-Enon Bridge Creep and Shrinkage 12
2.2.3 CEB-FIP '90 Creep and Shrinkage Model 12
2.3 Prestress Losses 14
2.3.1 Varina-Enon Bridge Prestress Losses 14
2.4 Thermal Gradient 15
2.4.1 Veterans' Glass City Skyway Thermal Gradient 16
2.4.2 Sunshine Skyway Bridge Thermal Gradient 17
2.4.3 Varina-Enon Bridge Thermal Gradient 18
2.5 Summary of the Literature 19
Chapter 3. Methodology 20
3.1 Data Acquisition 20
3.1.1 Spans 5 and 6 Instrumentation 20
3.1.2 Span 9 and span 11 Instrumentation 22
3.1.3 Data Collection 24
3.2 Data Processing 25
3.3 Finite Element Model 27

3.3.1 Finite Element Model Overview 27
3.3.2 Staged Construction Analysis 29
3.1.4 Prestress Losses 29
3.4 Effective Prestress Calculations from Field Data 30
3.4.1 Overview 30
3.4.2 Section Properties and Momnets 32
3.4.3 Creep, Shrinkage, and Secondary Prestress Axial Forces and Moments 35
3.4.4 Self-Equilibrating Stresses 36
3.4.5 Thermal Continuity Forces 37
3.5 Validation of FE Model 37
Chapter 4. Results and Discussion 40
4.1 Validation of Finite Element Model 40
4.1.1 Approach Span Validation 43
4.1.2 Main Span Validation 40
4.2 Finite Element and Field Data Results Results .....
4.2.1 Span 5 Effective Prestress from Field Data 48
4.2.2 Span 6 Effective Prestress from Field Data 50
4.2.3 Span 9 Effective Prestress from Field Data 51
4.2.4 Span 11 Effective Prestress from Field Data 55
4.2.5 Field Data Results Summary 55
4.3 Comparison of as designed and as behaving 56
4.4 Finite Element and Field Data Comparison 60
Chapter 5. Summary, Conclusions, and Recommendations for Future Work 61
5.1 Summary 61
5.2 Conclusions 62
5.3 Recommendations for Future Work 63
BIBLIOGRAPHY 64
Appendix A. Original Drawings of Tendon Profiles 66
Appendix B. Original Main Span Construction Drawings 76

LIST OF FIGURES

Figure 1.1: Aerial View of Varina-Enon Bridge....2
Figure 1.2: Elevation of Approach Spans 1-6 (Lindley 2019, with permission)....2
Figure 1.3: Typical Segment Dimensions (Lindley 2019, with permission)....3
Figure 1.4: Pier Segment Dimensions....3
Figure 1.5: Longitudinal Post-Tensioning Layout in Span 6 (Lindley 2019, with permission)....3
Figure 1.6: Elevation of Main Span Unit....4
Figure 1.7: Delta Frame Behavior Under Stay Force and Self-Weight....4
Figure 1.8: Longitudinal External Post-Tensioning Layout in Main Span 16....5
Figure 2.1: Artistic Rendering of Veterans' Glass City Skyway (Helmicki et al. 2012, public domain)…..9
Figure 2.2: VGCS Main Span Finite Element Model (Helmicki et al. 2012, public domain)……..10
Figure 2.3: VGCS Delta Frame in Finite Element Model (Helmicki et al. 2012, public domain)……..12
Figure 2.4: Isotropic View of Varina-Enon Bridge Approach Spans 1-6 FE Model (Lindley 2019, with permission)……13
Figure 2.5: Creep and Shrinkage Strains Over Time (reprinted by permission from Springer Nature Customer Service Centre GmbH: Springer Nature Basic Properties of Concrete Creep, Shrinkage, and Drying by Bažant and Jirásek 2018)……14
Figure 2.6: Elevation View of Sunshine Skyway Bridge (Shahawy and Arockiasamy 1996b, with permission from ASCE)……..15
Figure 2.7: Environmental Factors Affecting Thermal Gradients (Lindley 2019, with permission)…….16
Figure 2.8: Crack-Temperature-Strain Plot for 2013 Crack Opening Events (Maguire et al. 2014, with permission)……..17
Figure 3.1: Sensor Layout in Span 6 (Lindley 2019, with permission)....21
Figure 3.2: Sensor Layout in Span 5....21
Figure 3.3: Section A-A Sensor Layout (Lindley 2019, with permission)....21
Figure 3.4: Sensor Layout in Span 9....23
Figure 3.5: Sample Plot of Spans 5 and 6 Event Data Without Moving Average Filter....26
Figure 3.6: Sample Plot of Spans 5 and 6 Event Data With Moving Average Filter....26
Figure 3.7: Isometric View of Varina-Enon Bridge Full FE Model....28
Figure 3.8: Cross Section of Delta Frame in FE Model....28
Figure 3.9: Tendon S6-T9L Stress Profile....30
Figure 3.10: Cracked Section Used in the Analysis (Lindley 2019, with permission)……31
Figure 3.11: Spans 5 and 6 Dead Load Moment....32

Figure 3.12: Span 9 Dead Load Moment 33
Figure 3.13: Spans 5 and 6 Envelope of Maximum Moments 34
Figure 3.14: Span 9 Envelope of Maximum Moments 35
Figure 3.15: Thermal Continuity Moment as a Fraction of Applied Moment, Spans 1-6 37
Figure 3.16: Thermal Continuity Moment as a Fraction of Applied Moment, Spans 7-12 37
Figure 4.1: Measured and Computed Strains Throughout the Depth of the Box Girder Cross-Section at the Mid-span of Span 5 44
Figure 4.2: Measured and Computed Strains Throughout the Depth of the Box Girder Cross-Section at Section A-A in Span 6 45
Figure 4.3: Span 5 Average Tendon Profiles 46
Figure 4.4: Span 6 Average Tendon Profiles 46
Figure 4.5: Span 9 Average Tendon Profiles 47
Figure 4.6: Effective Prestress vs. Crack Displacement for all Span 5 Events 48
Figure 4.7: Histogram of Prestress Values for all Span 5 Events 49
Figure 4.8: Effective Prestress vs. Crack Displacement for Span 5 Events with Corresponding Crack Openings of 0.004 in. or Greater 49
Figure 4.9: Effective Prestress vs. Crack Displacement for all Span 6 Events 50
Figure 4.10: Histogram of Prestress Values for all Span 6 Events 50
Figure 4.11: Effective Prestress vs. Crack Displacements for Span 6 Events with Corresponding Crack Openings of 0.002 in. or Greater 51
Figure 4.12: Effective Prestress vs. Crack Displacement for all Span 9 Events 52
Figure 4.13: Histogram of Prestress Values for all Span 9 Events 52
Figure 4.14: Effective Prestress vs. Crack Displacement for Span 9 Events with Corresponding Crack Openings of 0.005 in. or Greater 53

LIST OF TABLES

Table 2.1: Coefficient s Based on Cement Type and Compressive Strength (ACI 209 2008, with permission)……..…11
Table 2.2: Effect of Aggregate Type on Modulus of Elasticity (ACI 209 2008, with permission)…….…5
Table 2.3: Coefficient Based on Type of Cement (ACI 209 2008, with permission)……..7
Table 2.4: Summary of Temperature Induced Thermal Stresses (Lindley 2019, with permission)……....12
Table 2.5: AASHTO Design Gradients……13
Table 3.1: Thermocouple Locations and Tributary Areas (Lindley 2019, with permission)..... 22
Table 3.2: Material Properties for Finite Element Model..... 29
Table 3.3: Creep, Shrinkage, and Secondary Prestress Effects at Instrumented Joint Openings..... 35
Table 4.1: Measured and Computed Span 5 Mid-span Deflections…….37
Table 4.2: Measured and Computed Lower Flange Strains in Segment 33..... 40
Table 4.3: Measured and Computed Upper Flange Strains in Segment 62 41
Table 4.4: Prestress Losses per FE Model..... 47
Table 4.5: Prestress Losses per Calculations From Field Data..... 55
Table 4.6: Finite Element and Field Data Comparison..... 60

Chapter 1. Introduction

This chapter offers a summary of the motivation for study, major principles, and the intent of the project. In order to provide context for the research motivation, the first section explains the principles of prestressed concrete and prestress losses. The concerns about the Varina-Enon Bridge, and a summary of previous research work are described in the second section followed by the purpose and scope of the project in the third section.

1.1 Motivation

Prestressed concrete is a composite material in which a precompression is provided to concrete structures using stressed steel strands. This technique of construction leads to much lighter, stiffer and more durable structures. With the invention of high-strength steels, beginning in the 1940s, the use of prestressed concrete became common in Europe and America. Prestressed concrete is now a very effective construction technique for bridges.

However, as the infrastructure ages, it is critical that professionals are able to measure the remaining service life of prestressed bridges accurately. The precise prediction of prestress losses is one main feature of the structural assessment of prestressed bridges. In addition, for systems with *unbonded* tendons, prestress losses can negatively impact the flexural strength. One type of unbonded tendon is external to the concrete cross-section, so the forces are transferred only at the anchors and deviators rather than throughout the length of the prestressing strands.

1.2 Varina-Enon Bridge Overview

Located on Interstate 295, The Varina-Enon Bridge is a cable-stayed, segmental, precast, post-tensioned box girder bridge which spans and spans the James River in Richmond, Virginia. As seen in Figure 1.1, the bridge has two parallel box girders which carry six lanes of traffic. The total length of the bridge is 4,680 ft and it consists of 28 spans. Twenty-one are *approach spans*, six are *transition spans*, and one is the *main span*.

Figure 1.1: Aerial View of Varina-Enon Bridge (open source)

As Figure 1.2 shows, each approach spans is 150 ft in length with seven 20-ft precast *typical segments* between the piers. These segments were match-cast in a long-run configuration and 9 ft long *pier segments* with 6 in. cast-in-place closure joints on either side of the pier segments.

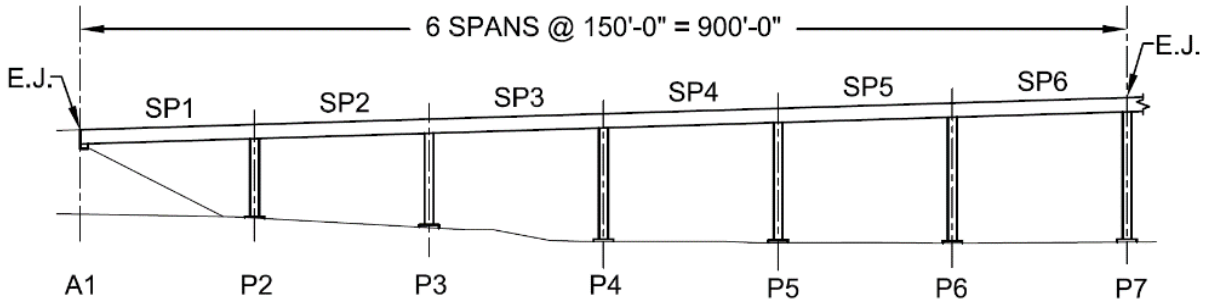

Figure 1.2: Elevation of Approach Spans 1-6 (Lindley 2019, with permission)

Figure 1.3 and Figure 1.4 show the dimensions of the typical segments and of the pier segments, respectively. Each box girder contains transverse internal post-tensioning. Additional transverse internal post-tensioning is used in the diaphragms which accommodate the anchors for the longitudinal tendons.

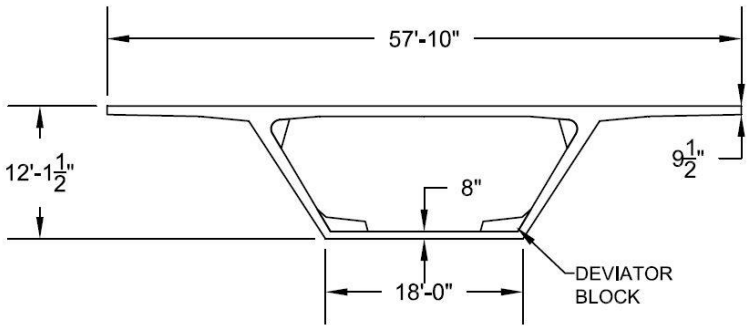

Figure 1.3: Typical Segment Dimensions (Lindley 2019, with permission)

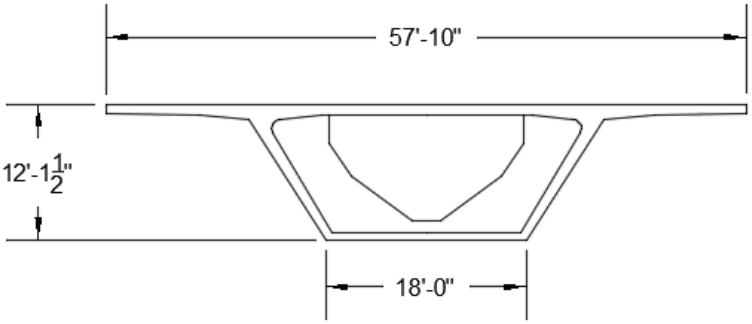

Figure 1.4: Pier Segment Dimensions (Lindley 2019, with permission)

As shown in Figure 1.5, there is external longitudinal post-tensioning of each approach span consisting of eight tendons located in the hollow interior of the segments. Each tendon contains 19 each 0.6 in. diameter strands. Tendons are located inside the box girder cell and are redirected at the bottom of the section through deviation blocks, as seen in Figure 1.5. Overlapping of tendons over the piers ensures continuity between the spans. Design drawings for all approach span longitudinal post-tensioning layouts can be found in Appendix A.

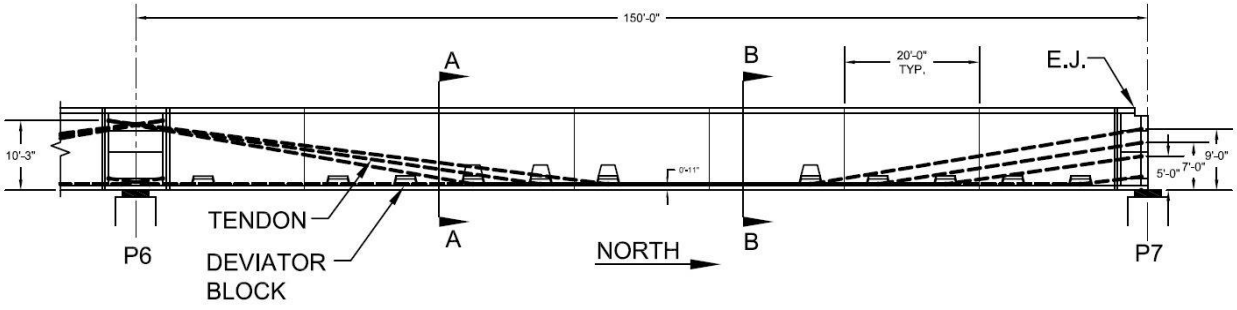

Figure 1.5: Longitudinal Post-Tensioning Layout in Span 6 (Lindley 2019, with permission)

As seen from Figure 1.6, the main span unit consists of three transition spans similar to the approaches on either side and one span which is completely cable stayed. The main span is 630 ft long with 10-ft typical segments. Using a beam and winch system, starting at Piers 16 and 17 and ending where the segments meet at midspan, it was constructed with the cantilever process. See Appendix B for the original drawings outlining the construction process of the main span unit. A closure pour connects the northbound and southbound sides of the main span unit

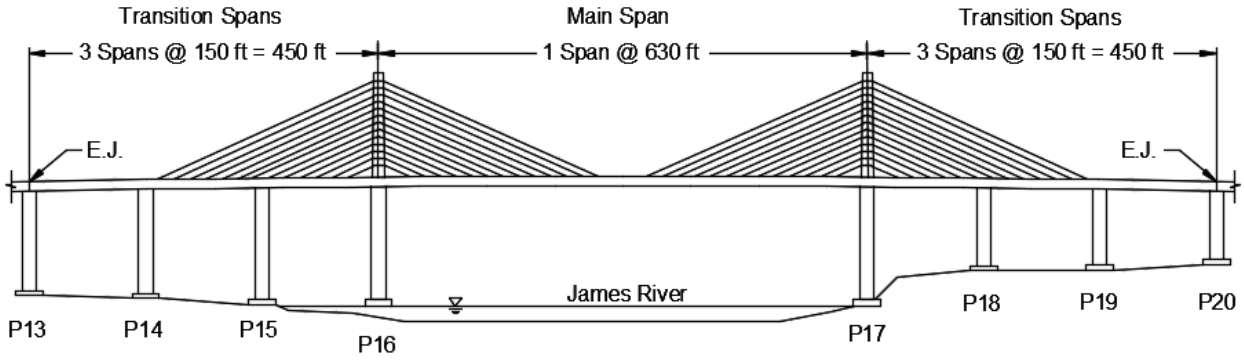

Figure 1.6: Elevation of Main Span Unit

The stay cables shown in Figure 1.6 meet the structure at the closure pour and, a *delta frame.* The delta frame has internal post tensioning and distributes the stay force with a truss-like behavior at each location where a stay cable meets the superstructure. Figure 1.7 shows the expected behavior of the delta frames under the stay force and dead load only.

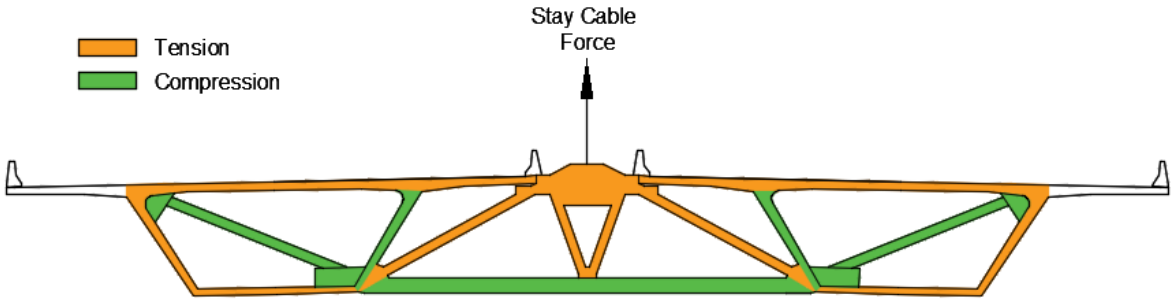

Figure 1.7: Delta Frame Behavior Under Stay Force and Self-Weight

Both internal and external longitudinal post-tensioning are used in the main span unit. The internal longitudinal post-tensioning runs through the box girders' top and bottom slabs as well as through the closure pours between north-bound and south-bound lanes.. The internal longitudinal tendons in the

transition spans consist of four each 0.6 in. strands, while those in the main span and closure pour contain 12 each 0.6 in. strands. A unique external longitudinal post-tensioning layout is used for the main span which can be seen in Figure 1.8. These tendons contain 12 each 0.6 in. strands. The stay cables consist of 0.6 in. strands varying in number from 80 to 90. In Appendix A, design drawings can be found for both external and internal longitudinal post-tensioning layouts of the main span unit.

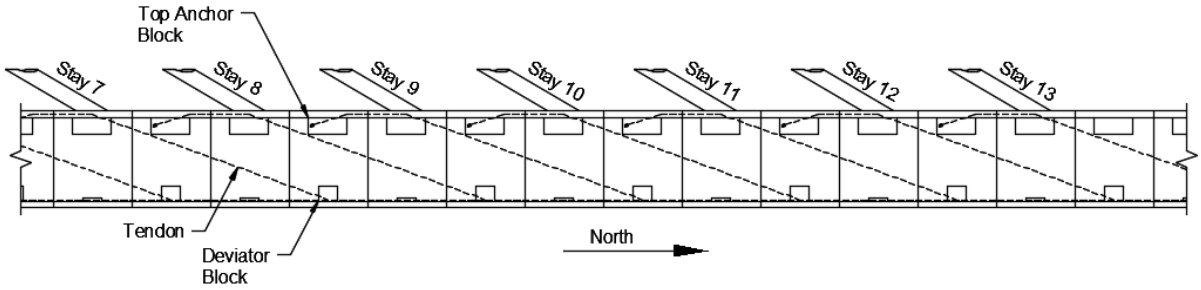

Figure 1.8: Longitudinal External Post-Tensioning Layout in Main Span 16 (Brodsky 2020, with permission)

1.2.1 Project Background

In July 2012, inspectors visually detected a joint opening up to 1/16 in. in the bottom flange in Section A-A in Figure 1.5. under large truck loads. This may suggest unanticipated high-tension levels in the bottom flange that would not be expected for a highly prestressed structure. Although this could be partially due to large thermal gradients or, it could also mean greater losses of prestress than expected.

A long-term monitoring system measuring the joint opening as well as the thermal gradient at that location was installed by Maguire et al. (2014. He concluded that crack openings are influenced by both traffic and thermal loads. An unpublished study was conducted in 2017 to study effective prestress force in Span 6 using joint opening data. Lindley (2019) reinstalled the original long-term monitoring system and refined the effective prestress evaluation in Span 6. Rachel Brodsky (2020) expanded the instrumentation in Span 9 and Span 14. These previous research projects are discussed in greater detail in the Literature Review.

1.3 Purpose and Scope

The objective of this research is to investigate the longitudinal flexural behavior of the Varina-Enon Bridge including the influence of time dependent effects. The goal is to use existing flexural cracks to estimate the longitudinal prestress loss and to equate these losses with those calculated by a finite element model.

The scope of this report involves,

- Estimation of longitudinal prestress losses using data collected from the field.

- Evaluate, reinstall and expand instrumentation on the Varina Enon Bridge
- Use already developed finite element model to evaluate predicted prestress losses using standard models for creep and shrinkage and to examine other aspects of the bridge's actions, such as super load response.
- Validation of FE model under super loads.
- Compare predicted bottom slab tension using the as designed criteria and compare to calculated tension using more recent creep and shrinkage models and design thermal gradients.
- Comparison of original LVDTs on top of bottom slab to newly installed LVDTs on the bottom of the bottom slab to further validate method to back calculate effective prestress.
- Provide recommendations for continued research on the Varina-Enon Bridge.

Chapter 2. Literature Review

This chapter discusses previous studies of the Varina-Enon Bridge and also other research conducted on several bridges that are similar to it. This chapter is divided into four major sections, which are, computer modeling, creep and shrinkage, prestress losses, and thermal gradients. A brief overview is provided for each section. Additionally, the methods used by previous researchers to address these topics are discussed.

2.1 Computer Modeling

With the advancement of technology, computation time has decreased significantly. As a result, finite element analysis has become much more efficient and refined. Finite element models of structures are powerful tools that are useful for analysis of existing structures. Finite element analysis software envisions how a system will behave mathematically. The user must provide needed inputs to the system, such as the geometry, material properties, and the loads which include physical loading of a structure, as well as environmental loads such as temperature and time-dependent effects such as creep and shrinkage, in order to obtain the response. The finite element analysis response after the simulation includes valuable information such as member stresses, strains, and deflections.

2.1.1 Veterans' City Glass Skyway Modeling

The Veterans' Glass City Skyway (VGCS) is a precast, segmental concrete bridge. This bridge is similar to the Varina-Enon Bridge. It is located on I-280 in Toledo, Ohio and carries three lanes of traffic in each direction. It has 56 approach spans which totals 7,273 ft and has one cable-stayed main span on the unit that totals 1,525 ft. (Helmicki et al.2012) provides a view of the bridge.

Figure 2.1: Artistic Rendering of Veterans' Glass City Skyway (Helmicki et al. 2012, public domain)

The main span of the VCGS was modeled three-dimensionally using LARSA 4D. Figure 2.2 shows a schematic overview of the model. Linear behavior was assumed for the model. The contribution of the delta frames to the longitudinal stiffness of the structure was neglected. In addition, it was assumed that the elastomeric bearings at the superstructure to substructure connections only contribute to vertical stiffness. The longitudinal stiffness of the elastomeric bearing was neglected (Helmicki et al. 2012).

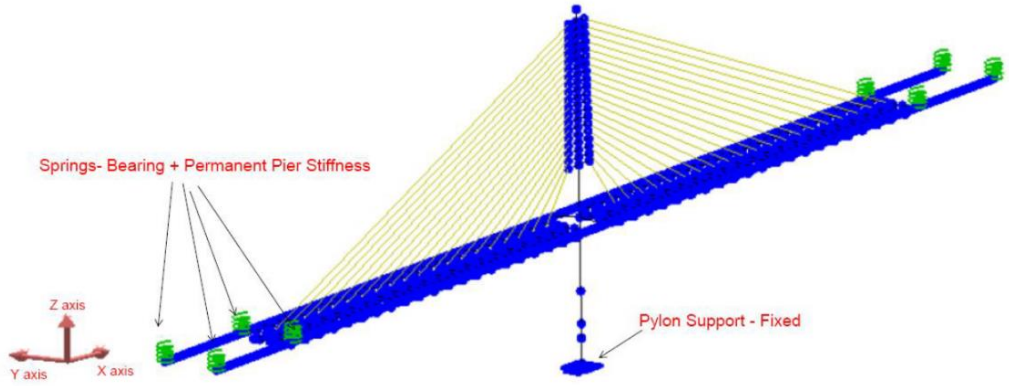

Figure 2.2: VGCS Main Span Finite Element Model (Helmicki et al. 2012, public domain)

The model consisted of three types of elements, which are namely, beam elements, cable elements, and spring elements. The stays for the VGCS are modeled in such a way that there are two separate stays being stressed at the same time. The cable elements' properties require non-linear analysis. But since the bridge's weight itself is very heavy, the cables are expected to be in tension, and there should not be a live load large enough to reverse the stresses. Therefore, stress stiffening properties of the cables were ignored. The elastomeric bearings were modeled as spring elements. The box girders and delta frame members were modeled as beam elements (Helmicki et al. 2012). Figure 2.3 shows the arrangement of the delta frames.

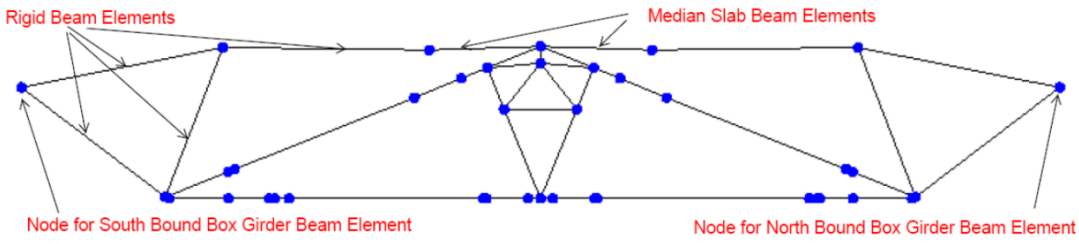

Figure 2.3: VGCS Delta Frame in Finite Element Model (Helmicki et al. 2012, public domain)

The measured strains obtained from dynamic load tests using segment haulers and static load tests were compared to the results predicted from the model. A further validation of the model was conducted by a truck test on the VGCS and then the measured data was compared against the analytically obtained values. For collection of data from the dynamic truck tests, electrical-resistance strain gages were used, and for the static truck tests, both vibrating wire and electrical-resistance strain gages were used. Influence lines

for both the dynamic truck tests and the model were obtained and compared. Additionally, the locations of maximum response were compared (Helmicki et al. 2012).

Strains in the delta frame members were measured, during initial and final post-tensioning, and then compared against the prediction results from the model. To convert the stresses obtained by the prediction of the model, a stress-to-strain transformation was used so that the strain values could be compared. It was concluded that the finite element model accurately represented the behavior of VGCS (Nimse et al. 2015).

2.1.2 Illinois Tollway

It is a 294-mile system which comprised of 5 tollways and carries 1.6 million vehicles per day. It is in Downers Grove on I-355 on Finlay road in Illinois. It was constructed in 1988. It consists seven span and is 908-ft long. The substructure of the bridge is normally reinforced with pier height of upto 50 ft. The super structure is built with match cast segments with longitudinal post-tensioning. Span by span balanced cantilever method of construction was used. Load rating for the substructure and superstructure was done using in depth post-tensioning evaluation. Six tendons were tested using vibration tests using vibrating wire gages to estimate prestress forces and FE model in LARSA 4D was created for comparison which used time dependent analysis. The model consisted of three types of elements, which are namely, beam elements, cable elements, and spring elements. These tests were conducted in 2003 after 15 years of creep and shrinkage losses. It was concluded that the FE model accurately represented the behavior of the tollway bridge.

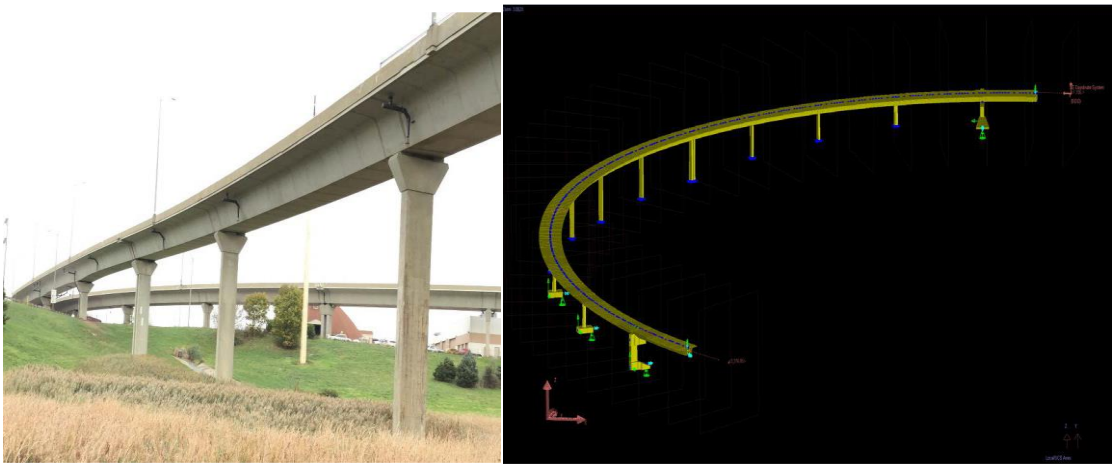

Figure 2.4: Illinois Tollway bridge in Finite Element Model (Ciorba Group, public domain)

2.1.3 Varina-Enon Bridge Modeling

Lindley (2019) created a three-dimensional finite element model of the northbound approach Spans 1-6 of the Varina-Enon Bridge using LARSA4D, as seen in Figure 2.4. The box girders and piers of the model were made of beam elements, and the bearing pads were modeled as spring elements. In the model, springs had translational stiffness in the Z and X-directions, and rotational stiffness about the Y-axis. As for the remaining three degrees of freedom, they were fixed. The stiffness values of the springs were validated by live load tests conducted by Maguire et. al (2014). The model also include the longitudinal external post-tensioning tendons and the self-weights of the tendon deviator blocks and barrier rails. The model of the bridge was validated against the deflection data collected from live load tests conducted by Maguire et al. (2014). The deflections measured due to different load configurations when compared to the predicted deflection by the model were found to match reasonably well (Lindley 2019).

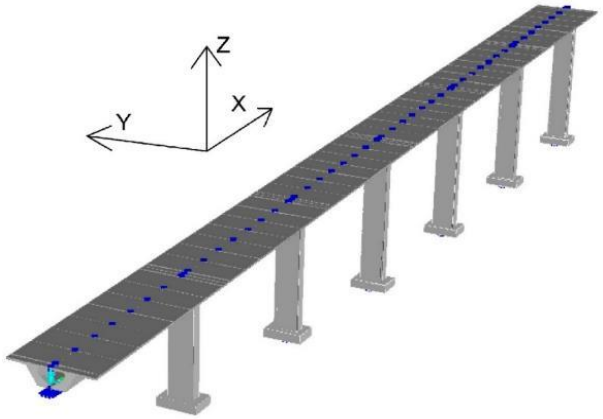

Figure 2.5: Isotropic View of Varina-Enon Bridge Approach Spans 1-6 FE Model (Lindley 2019, with permission)

2.2 Creep and Shrinkage

The tendency to continue to deform under a sustained load over a long period of time is called creep. Shrinkage is the change in volume of material due to loss of moisture. According to most traditional creep and shrinkage models, stresses and strains due to creep and shrinkage increase over time and approach an asymptotic value (see Figure 2.6). It can also seen that after unloading, there is recovery of all elastic strain and some creep strain. Various creep and shrinkage models are currently in use, such as CEB-FIP ’78, CEB-FIP ’90, ACI 209, AASHTO, and B3. Each model requires material properties and environmental conditions as inputs, but uses different functions to quantify the progression of creep and shrinkage over time (Lindley 2019).

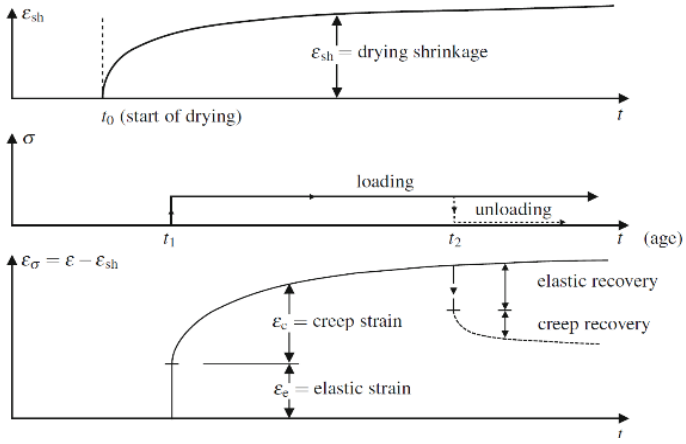

Figure 2.6: Creep and Shrinkage Strains Over Time (reprinted by permission from Springer Nature Customer Service Centre GmbH: Springer Nature Basic Properties of Concrete Creep, Shrinkage, and Drying by Bažant and Jirásek 2018)

2.2.1 Sunshine Skyway Bridge Creep and Shrinkage Models

The Sunshine Skyway Bridge is a prestressed, concrete, cable-stayed bridge. It is located on I-275 in Florida. It has four types of spans, which are, trestle approach spans, low-level approach spans, high-level approach spans, and three cable-stayed spans. The main cable-stayed spans consist of single-cell precast box segments (Shahawy and Arockiasamy 1996a). Figure 2.7 shows the elevation of the main cable-stayed span.

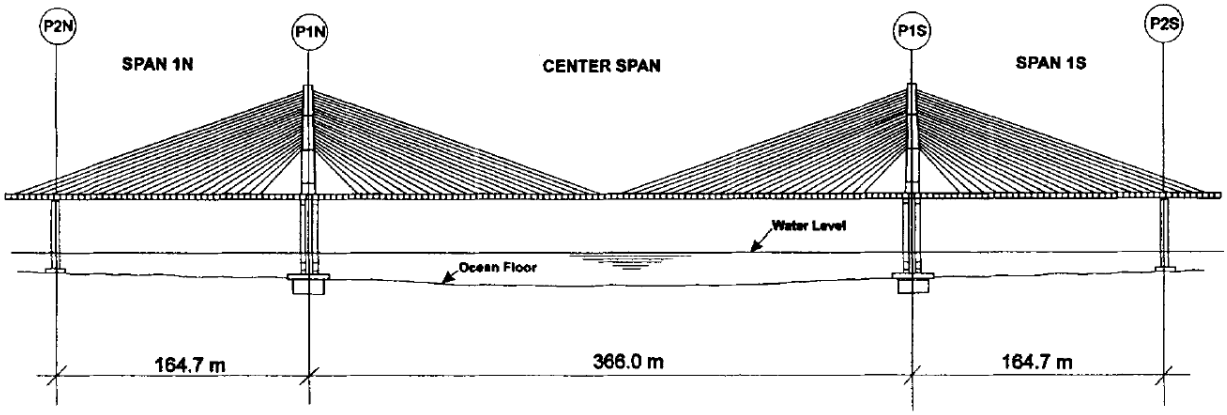

Figure 2.7: Elevation View of Sunshine Skyway Bridge (Shahawy and Arockiasamy 1996b, with permission from ASCE)

Shahawy and Arocklasamy (1996) developed an analytical model for prediction of time-dependent strain histories throughout all construction stages of the Sunshine Skyway Bridge. Strain gages were used to instrument the box girder. The data was collected, and it was used to calibrate the analytical computer

model. For the calculation of creep and shrinkage strains, the age-adjusted effective-modulus method was employed. According to this method, an aging coefficient, which accounts for aging, is used on the ultimate value of creep after the application of a load. Since the value also depends on ambient relative humidity, volume to surface ratio, and temperature, a correction factor that accounts for these was also used. For each construction stage, the stresses and the strains were calculated using an iterative process. During the construction stage, the aging coefficient was changed since the loading was also changed. However, from the study, it was determined that the time-dependent strains due to the construction sequence based on a constant aging coefficient gave similar results when compared with results from a varying aging coefficient. Therefore, a constant aging coefficient was determined to be adequate for analysis (Shahawy and Arockiasamy 1996b).

2.2.2 Varina-Enon Bridge Creep and Shrinkage

For prediction of prestress losses, three different creep and shrinkage models were considered: CEB-FIP ’78, CEB-FIB ’90, and AASHTO. The bridge was designed using the CEB-FIB ’78 model code, but when the calculated effective prestress was compared against field data, it was found that the CEB-FIP ’90 most closely matched the performance (Lindley 2019). Therefore, for the purposes of this thesis, CEB-FIP ’90 is used to calculate the creep and shrinkage effects.

2.2.3 CEB-FIP ’90 Creep and Shrinkage Model

The CEB-FIP ’90 model code was published by the Comité Euro-International Du Béton in 1990 as an update to the CEB-FIP ’78 model code. According to this model, creep and shrinkage are represented as hyperbolic over time. The ultimate values are corrected for mixture proportions and environmental conditions. The parameters required to implement the model are: the age of the concrete when drying starts, the age of the concrete at the time of loading, the mean 28-day compressive strength of concrete, the relative humidity, the volume-surface ratio of the member, and the type of cement (ACI 209 2008). The CEB-FIP ’90 calculations for creep and shrinkage per ACI 209 (2008) are described below. The unit system is lb. and in.

The creep effect is defined by the compliance function given by Equation (2-1), which describes the total stress-dependent strain because of a unit stress.

$$J(t,t_o) = \frac{1}{E_{cmto}} + \frac{\Phi_{28}(t,t_o)}{E_{cm28}} \qquad (2\text{-}1)$$

E_{cmto} is the modulus of elasticity at the time of loading t_o, which is calculated according to (2-2).

$$E_{cmt} = E_{cm28} exp\left[\frac{s}{2}\left(1 - \sqrt{\frac{28}{t/t_1}}\right)\right] \qquad (2\text{-}2)$$

t_1 = 1 day, and s is a coefficient which is dependent on the type of cement and compressive strength of concrete taken from Table 2.1.

Table 2.1: Coefficient s Based on Cement Type and Compressive Strength (ACI 209 2008, with permission)

f_{cm28}	Type of cement	s
≤60 MPa (8700 psi)	RS (rapid hardening high-strength cement)	0.20
	N or R (normal or rapid hardening cements)	0.25
	SL (slowly-hardening cement)	0.38
>60 MPa (8700 psi)*	All types	0.20

*Case not considered in CEB MC90.

E_{cm28} is the mean 28-day modulus of elasticity. It is calculated according to Equations (2-2) and (2-3).

$$E_{cm28} = \alpha_E 3{,}118{,}310_3 \sqrt{\frac{f_{cm28}}{f_{cmo}}} \qquad (2\text{-}2)$$

$$f_{cm28} = f'_c + 1160psi \qquad (2\text{-}3)$$

Here, f_{cmo} is taken as 1450 psi, and α_E is a value that depends on the type of aggregate taken from Table 2.2. f'_c is the compressive characteristic cylinder strength which is defined as the strength below which only 5% of all possible strength measurements are expected to fall.

Table 2.2: Effect of Aggregate Type on Modulus of Elasticity (ACI 209 2008, with permission)

Aggregate type	α_E
Basalt, dense limestone aggregates	1.2
Quartzitic aggregates	1.0
Limestone aggregates	0.9
Sandstone aggregates	0.7

Φ_{28} is the 28-day creep coefficient calculated in Equations (2-4) through (2-10).

$$\Phi_{28}(t, t_o) = \Phi_o \beta_c (t - t_o) \qquad (2\text{-}4)$$

$$\Phi_o = \Phi_{RH}(h)\beta(f_{cm28})\beta(t_o) \qquad (2\text{-}5)$$

$$\Phi_{RH}(h) = \left[1 + \frac{1 - h/h_0}{\sqrt[3]{0.1[(V/S)/(V/S)_0]}}\alpha_1\right]\alpha_2 \qquad (2\text{-}6)$$

$$\beta(f_{cm28}) = \frac{5.3}{\sqrt{f_{cm28}/f_{cmo}}} \qquad (2\text{-}7)$$

$$\beta(t_o) = \frac{1}{0.1 + (t_o/t_1)^{0.2}} \qquad (2\text{-}8)$$

$$\alpha_1 = \left[\frac{3.5 f_{cmo}}{f_{cm28}}\right]^{0.7} \quad (2\text{-}9)$$

$$\alpha_2 = \left[\frac{3.5 f_{cmo}}{f_{cm28}}\right]^{0.2} \quad (2\text{-}10)$$

Here, h is the ambient relative humidity in decimals, h_o = 1, V/S is the volume-surface ratio, and $(V/S)_o$ = 2 in. The coefficient $\beta_c(t\text{-}t_o)$ represents the development of creep over time after loading. It can be calculated with Equations (2-11) through (2-13).

$$\beta_c(t - t_o) = \left[\frac{(t-t_o)/t_1}{\beta_H + (t-t_o)/t_1}\right]^{0.3} \quad (2\text{-}11)$$

$$\beta_H = 150[1 + (1.2h/h_o)^{18}](V/S)/(V/S)_o + 250\alpha_3 \leq 1500\alpha_3 \quad (2\text{-}12)$$

$$\alpha_3 = \left[\frac{3.5 f_{cmo}}{f_{cm28}}\right]^{0.5} \quad (2\text{-}13)$$

The shrinkage strains are calculated as per Equation (2-14).

$$\varepsilon_{sh}(t, t_c) = \varepsilon_{cso}\beta_s(t - t_c) \quad (2\text{-}14)$$

t is the age of the concrete (days) and t_c is the age of the concrete (days) when it starts drying. ε_{cso} is the notional shrinkage coefficient which can be obtained from equations (2-15) through (2-18).

$$\varepsilon_{cso} = \varepsilon_s(f_{cm28})\beta_{RH}(h) \quad (2\text{-}15)$$

$$\varepsilon_s(f_{cm28}) = [160 + 10\beta_{sc}(9 - f_{cm28}/f_{cmo})]10^{-6} \quad (2\text{-}16)$$

$$\beta_{RH}(h) = -1.55\left[1 - \left(\frac{h}{h_o}\right)^3\right] \; for \; 0.4 \leq h < 0.99 \quad (2\text{-}17)$$

$$\beta_{RH}(h) = 0.25 \; for \; h \geq 0.99 \quad (2\text{-}18)$$

The coefficient β_{sc} depends on the type of cement and can be taken from Table 2.3.

Table 2.3: Coefficient Based on Type of Cement (ACI 209 2008, with permission)

Type of cement according to EC2	β_{sc}
SL (slowly-hardening cements)	4
N and R (normal or rapid hardening cements)	5
RS (rapid hardening high-strength cements)	8

$\beta_{sc}(t\text{-}t_c)$ gives the development of shrinkage with time and is given by Equation (2-19).

$$\beta_s(t - t_c) = \left[\frac{(t-t_c)/t_1}{350[(V/S)/(V/S)_o]^2 + (t-t_c)/t_1}\right]^{0.5} \quad (2\text{-}19)$$

2.3 Prestress Losses

Total prestress losses can be calculated as the sum of immediate and time-dependent losses, as shown in Equation (2-20) (Lindley 2019). Immediate prestress losses occur due to seating and friction (⊿

f_{pFS}) and also because of elastic shortening (Δf_{pES}). However, the time-dependent prestress losses which include those due to creep (Δf_{pCR}) and shrinkage (Δf_{pSH}) of the concrete as well as relaxation of the steel strands (Δf_{pRE}) are much more significant.

$$\Delta f_{pT} = \underbrace{\Delta f_{pFS} + \Delta f_{pES}}_{\text{Short-term losses}} + \underbrace{\Delta f_{pCR} + \Delta f_{pSH} + \Delta f_{pRE}}_{\text{Long-term losses}} \qquad (2\text{-}20)$$

There are several methods available for calculating long-term prestress losses, but they have varying degree of accuracy. One of those, the lump-sum method, depends only the level of stress in the steel and concrete. Another one of the simplified method estimates the long-term losses due to creep, shrinkage, and relaxation individually using factors which depend on various properties such as type of concrete, age at loading, and type of prestressing steel. However, the most accurate methods out of all these are time-step methods and age-adjusted effective modulus methods. These methods directly consider the creep, shrinkage, and relaxation models for the materials being used. For detailed overview on these, refer ACI 423.10R *Guide to Estimating Prestress Losses* (ACI 423 2016), and Lindley (2019).

2.3.1 Varina-Enon Bridge Prestress Losses

Lindley (2019) studied prestress losses in Span 6 of the northbound side of the Varina-Enon Bridge. Data obtained from the joint opening at Section A-A in Figure 1.5 was used to calculate the effective prestress force at the same location. Under the assumption that there is no stress at the crack when it opens, the effective prestress force was back-calculated from the field data. The LARSA-4D finite element model as described in Section 2.1.3, predicted the prestress losses and were compared against those calculated from field data. In 2013, the average prestress loss was calculated as 47.3 ksi, while the LARSA-4D model predicted losses of 43.3 ksi. Therefore, the prestress losses in reality were 8.4% greater than those predicted by the model (Lindley 2019).

2.4 Thermal Gradient

As mentioned in the Introduction, *thermal gradients* are the temperature differences throughout the depth of a structure. Figure 2.8 shows the various factors that impact the temperature distribution. These factors include solar radiation, ambient temperature, wind, and humidity (Xu et al. 2019). In the case of large box girders, since the wide top flange is exposed to solar radiation while the rest of the girder is in shade, there is a development of thermal gradients. (Lindley 2019).

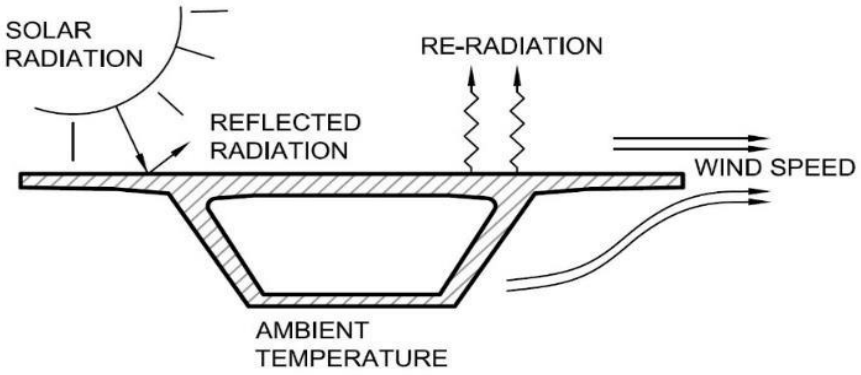

Figure 2.8: Environmental Factors Affecting Thermal Gradients (Lindley 2019, with permission)

In the case of Varina-Enon Bridge, non-linear thermal gradients develop on days with large temperature fluctuations and high solar radiations. These thermal gradients induce: *self-equilibrating stresses* and *continuity stresses*. Self-equilibrating stresses are the stresses induced when the configuration of a simply-supported beam is considered. Continuity stresses arise from the effects of the non-linear thermal gradient on the redundant structure (Lindley 2019). Table 2.4 gives a brief summary of the types of temperature induced thermal stresses. For a more detailed description, see Lindley (2019). See Sections 3.4.4 and 3.4.5 of this thesis for descriptions of the calculations for self-equilibrating stress and continuity stress.

Table 2.4: Summary of Temperature Induced Thermal Stresses (Lindley 2019, with permission)

	Determinate	Indeterminate
	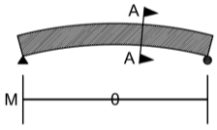	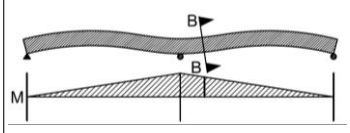
Linear Thermal Gradient 	Stresses @ A-A 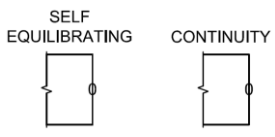	Stresses @ B-B 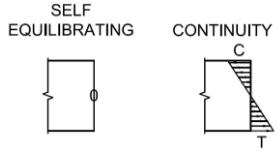
Non-Linear Thermal Gradient 	Stresses @ A-A 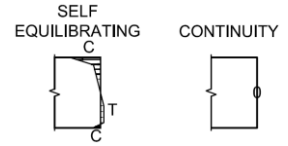	Stresses @ B-B 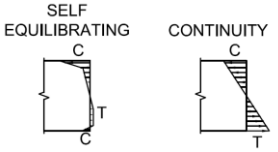

2.4.1 Veterans' Glass City Skyway Thermal Gradient

Helmicki et al. (2012) studied thermal gradients, both positive and negative, inside the concrete box girders of the VGCS. Positive thermal gradients means that the topmost section has higher temperature than the rest, and the negative gradient is the opposite. Negative thermal gradients during the day can lead to cracking of the top slab, which in turn would allow moisture to seep in and ultimately result in corrosion of reinforcing steel and prestressing strands (Helmicki et al. 2012).

The aim of the study was to see whether the actual thermal gradients were consistent with the AASHTO design code. Table 2.5 shows many AASHTO positive and negative design gradients. For the purpose of the study, eight full months of temperature data were collected using thermistors. It was concluded that the positive thermal gradient was consistent in shape throughout the duration of eight months and that the positive gradients typically were in the range of AASHTO design code. Due to negative gradients not being a daily occurrence, only two months of data showed negative thermal gradients, It was concluded that they were not a large concern. Nonetheless, from the study it was found that the negative gradients were not very consistent as compared to the positive gradients. Regardless, they still typically fell within the range of AASHTO design code (Helmicki et al. 2012).

Table 2.5: AASHTO Design Gradients

Design Code	AASHTO 89	AASHTO 94	AASHTO 98
Positive Gradients	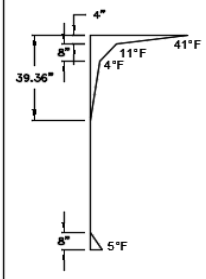	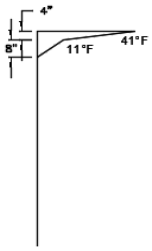	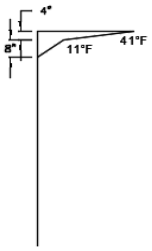
Negative Gradients	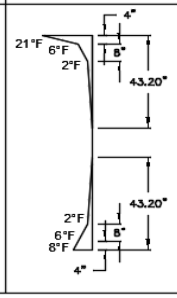	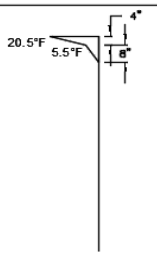	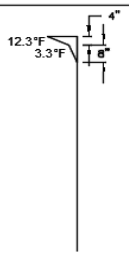

2.4.2 Varina-Enon Bridge Thermal Gradient

Maguire et. al (2014) studied on the thermal gradient of the Varina-Enon Bridge. For the study, the temperature data was collected using thermocouples which were installed throughout the depth of the box

girder. The study was done to fulfill the objesvive of determining whether the measured thermal gradient fell within the close range of AASHTO design code, as well as to correlate the thermal gradient and the observed joint opening at Section A-A in Figure 1.5.

From the study, it was concluded that the measured thermal gradient was similar in shape to the design gradient, but it was significantly smaller in magnitude. In addition to that, it was also concluded from the study that the crack opening in Span 6 was influenced by both heavy truck loads as well as the large thermal gradients. As we can see in Figure 2.9, during the period of time when the weather was warmer, there were more crack opening events, and the crack displacements were larger. (Maguire et al. 2014).

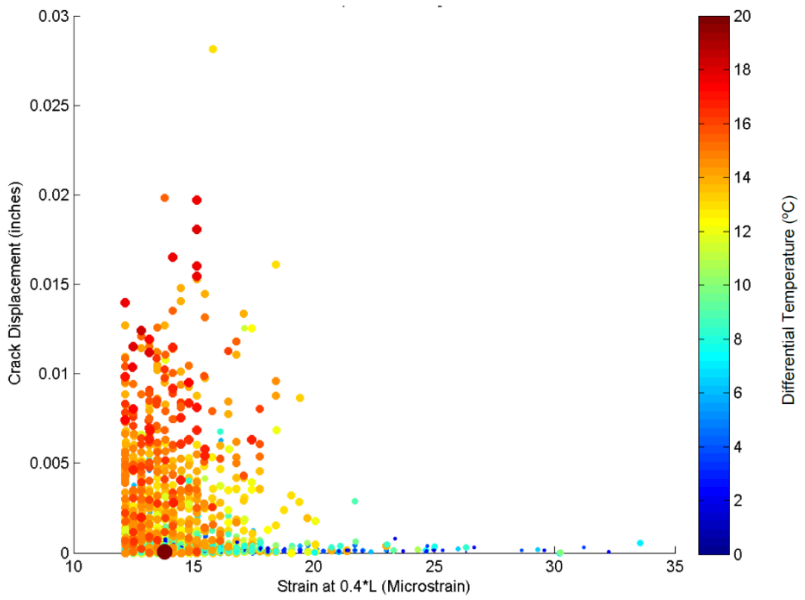

Figure 2.9: Crack-Temperature-Strain Plot for 2013 Crack Opening Events (Maguire et al. 2014, with permission)

2.5 Summary of the Literature

In numerous studies, finite element modeling (FEM) has been used for mathematical analysis. The FEM is also used in the case of multiple precast box girder bridges in order to predict the mathematical behavior during staged-construction and also for time-dependent behavior including creep, shrinkage, and prestress losses. A FEM model of the Varina-Enon Bridge was created in LARSA4D to obtain predicted prestress losses. The model ultimately also helped in various calculations such as the calculations of prestress losses from measured data. FEM modeling is an important tool as it can be used to obtain valuable information regarding the behavior of a structure.

The time-dependent effects of creep and shrinkage have a significant impact on a structure's long-term behavior. There is also a need to understand them in order to obtain the predicted prestress losses. There are several different models in current use that predict creep and shrinkage strains over time. In the case of the Sunshine Skyway Bridge, an analytical model with time-dependent creep and shrinkage strains used the age-adjusted effective modulus method. Although, there are multiple creep and shrinkage models to choose from to predict prestress losses in the Varina-Enon Bridge, ultimately it was concluded that the CEB-FIP '90 model provided the most accurate prediction.

The understanding and calculation of time-dependent prestress losses plays a major role in understanding the serviceability of a structure. The computation of prestress losses measured in northbound Span 6 of the Varina-Enon Bridge was done with the measured data at the location of the observed joint opening. After that, the calculated prestress losses were compared against the prestress losses obtained from the finite element model. It was concluded that, the actual prestress losses were 8.4% greater than the losses predicted by the model.

Thermal gradients played an important role in the development of internal stresses in large box girders. A study on the VGCS was done to check whether the thermal gradients fell within the AASHTO design code. Similarly, a study on the Varina-Enon Bridge was also done and it was conducted that the measured gradient indeed fell within the design code. In addition, it was also concluded that the larger thermal gradients lead to larger crack openings.

The work presented in later chapters of this thesis further validates the finite element model and take forward the results obtained at various crack locations. It also helps to understand the issues with design leading to the cracks in the Bridge.

Chapter 3. Methodology

After the discovery of cracking in Span 6 of the northbound approach unit, the durability of the Varina-Enon Bridge (VEB) came into question. Sensors were installed by Maguire et al. (2014) at the crack position to monitor thermal gradients and crack openings. This chapter describes the procedures and measures taken to fulfill the purpose of the project to estimate the effective prestress force from field data collected at multiple joint opening locations in the Varina-Enon Bridge and to compare the results with those obtained from a complete structure finite element model.

The first section describes how the data was collected from instrumentation in northbound spans 5, 6, 9 and 11. The second section describes how the data was processed in order to obtain main interest measurements. The third section offers a summary of the computer model and explains how time-dependent effects have been taken into consideration. The fourth section of the chapter describes the methods used for validation of the finite element model.

3.1 Data Acquisition

3.1.1 Spans 5 and 6 Instrumentation.

To continue the original research, Lindley (2019) reinstalled the original long-term monitoring system which was earlier installed by Maguire et al. (2014) for the main purpose of measuring the crack opening and thermal gradients at joint openings in Span 6. Lindley (2019) also extended instrumentation into Span 5, location of another crack opening, for the evaluation of the effective prestress force. The sensors in this long-term monitoring system include Transtek Linear Variable Differential Transformers (LVDTs), Bridge Diagnostics Inc. (BDI) strain transducers, and thermocouples (TCs). Figure 3.1 and Figure 3.2 shows the locations of the sensors in Span 6 and Span 5, respectively. Later, instrumentation was extended to bottom of the bottom flange in Span 6 to have better understanding of the behavior.

The strain transducers measured live load strains on the bottom of top flange and top of bottom flange of the box girders. In Span 6, Segment B-B shown in Figure 3.1, which is 0.4 times the span length of Pier 7, Gage ST01 was located at the place of the highest anticipated live load moment to serve as trigger gage. Trigger gage is the gage located at the location in a particular span where maximum strain is expected ($0.4*L_{span}$). At the top of the bottom flange adjacent to the opening joint in Span 6, Gage ST02 measured the strain. The LVDTs at Section A-A shown in Figure 3.1 for Span 6 and Section C-C shown in Figure 3.2 for span 5 have LVDTs installed to measure the crack displacements at the joint openings.

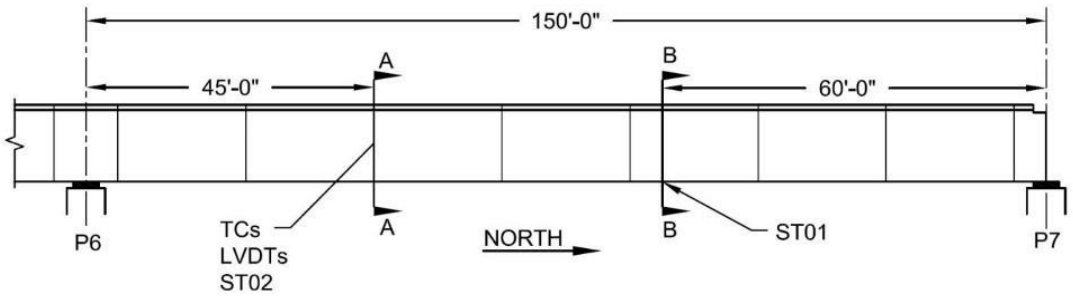

Figure 3.1: Sensor Layout in Span 6 (Lindley 2019, with permission)

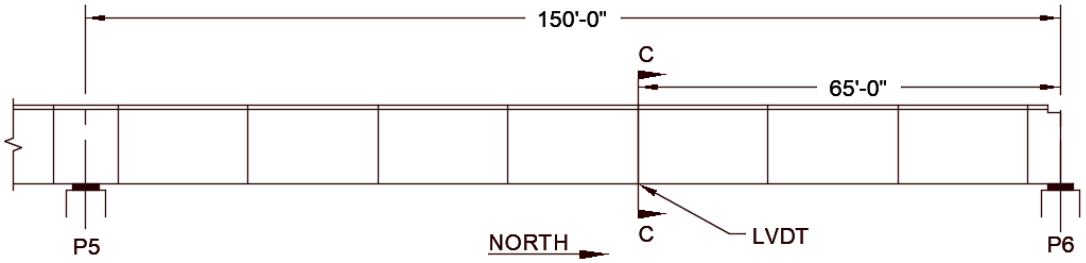

Figure 3.2: Sensor Layout in Span 5

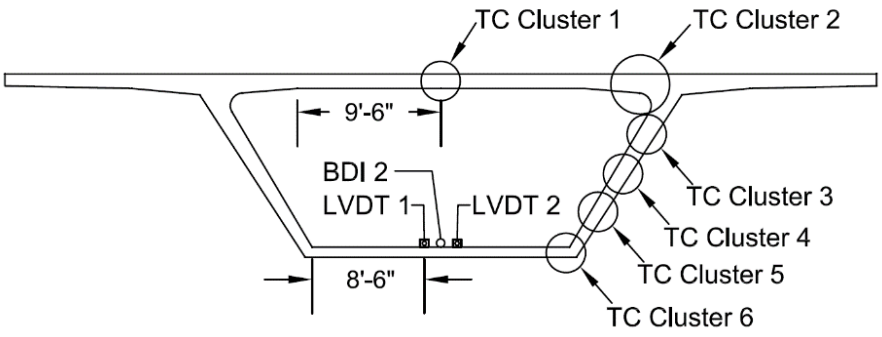

Figure 3.3: Section A-A Sensor Layout (Lindley 2019, with permission)

Thermocouples were installed in clusters throughout the depth of the box girder at Section A-A as shown in Figure 3.3. In some locations, thermocouples were placed in the section at about the same depth. For the purpose of calculating the restraint force and moment from the thermal gradient so their measurements of temperature were combined and viewed as one measurement. Table 3.1 summarizes the position of each thermocouple. It was assumed that the measured thermal gradient at Section A-A is representative of the thermal gradient along the full length of the Varina-Enon Bridge (Maguire et al. 2014). More explanation about thermal restraint moments and axial forces is presented in section 2.4 and Lindley(2019).

Table 3.1: Thermocouple Locations and Tributary Areas (Lindley 2019, with permission)

TC	Elev. from top of wearing surface, in.	CG from the bottom, in.	Tot area, in.^{2}	Area*cg(from bottom of section), in.^{3}
1	140.0	8.1	1,086.8	8,838.8
2	142.3	3.2	496.5	1,602.6
3	144.5	1.1	457.5	481.4
4,5	108.8	35.8	754.9	27,043.1
	110.8			
6,7	78.0	66.2	848.4	56,156.3
	80.6			
8,9	48.5	97.5	1,030.0	100,394.8
	51.1			
10	15.8	122.9	667.5	82,040.1
11	13.8	131.8	317.2	41,810.9
12	11.8	133.9	673.2	90,158.4
13	9.8	135.3	713.9	96,594.5
19	9.5	136.2	692.9	94,363.8
14	7.8	137.6	1,041.0	143,241.6
15	6.5	138.9	798.1	110,876.0
16,21	5.5	140.0	694.0	97,160.0
	5.5			
17,22	4.5	141.0	694.0	97,854.0
	4.5			
18,23	3.5	142.0	694.0	98,548.0
	3.5			
24	2.5	143.7	957.7	137,614.8
99	0.8	145.6	1,131.2	164,666.0

See Maguire et al. (2015), Lindley (2019) and Brodsky (2020) for more information about the types and positions of sensors mounted in Spans 5 and 6 of the Varina-Enon Bridge.

3.1.2 Span 9 and Span 11 Instrumentation

A mobile data acquisition system which was intended to be moved to different locations of the bridge was installed at another joint of interest in Span 9. As shown in Figure 3.4, Transtek LVDTs and BDI strain transducers were mounted to track the joint opening under heavy live loads and determine the effective prestress force for that span. Gage ST04, located at section E-E at midspan, served as the trigger

gage for the data acquisition system in Span 9. Two LVDTs and gage ST03 were installed at section D-D to measure crack displacements and strain at that location. After collecting sufficient data from Span 9, this mobile data acquisition system was later moved to a joint opening in Span 11. As shown in Figure 3.5, Similar installation was done in this span where Section F-F shows the location of trigger gage and Section G-G shows the location of crack.

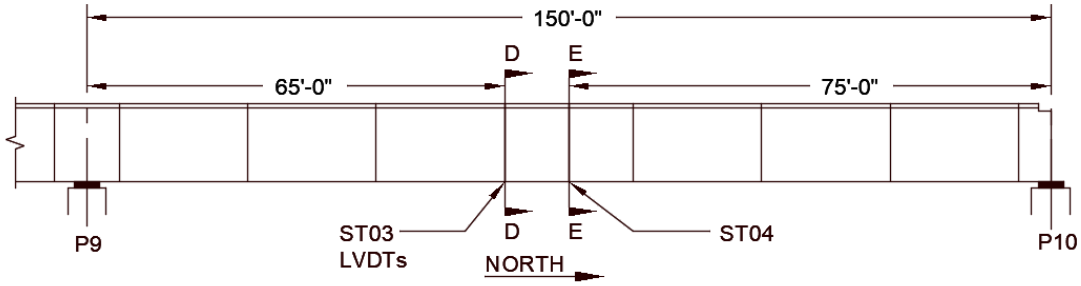

Figure 3.4: Sensor Layout in Span 9 (Brodsky 2020, with permission)

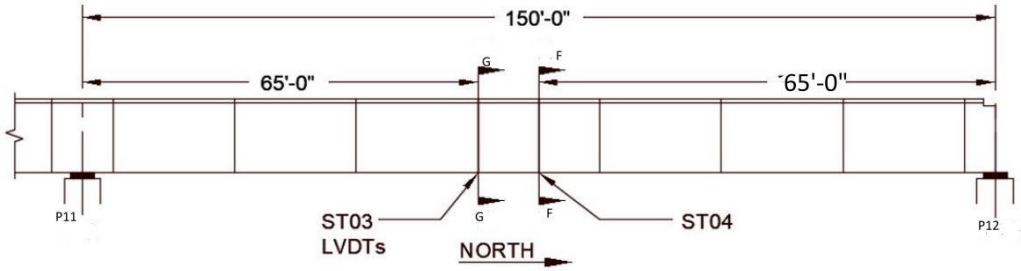

Figure 3.5: Sensor Layout in Span 11

3.1.3 Span 14 Instrumentation.

The data acquisition system set up in the north bound lane of Span 14 of the Varina- Enon had multiple functions. The first was to measure uplift deflections. This was done using a taut-wire measuring system (1 Wenglor Laser displacement sensor (LDS)). The second function was to measure the opening of shear cracks which have formed in the south end of this span as an apparent result of this uplift (2 LVDTs spanning the shear crack). The last function was to measure the transverse delta-frame behaviour (5 BDI strain transducers located at interior of delta frame). Figure 3.6, and Figure 3.7 depicts the instrumentation in Span 14.

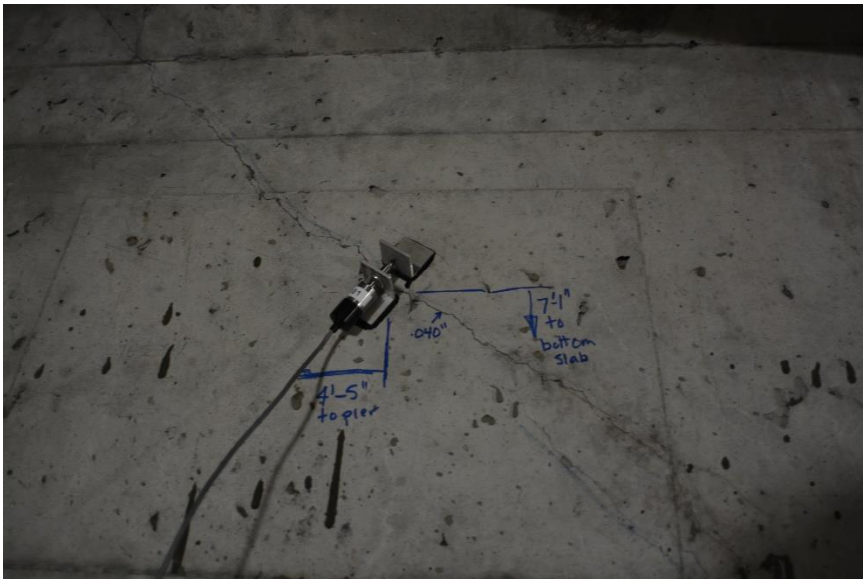

Figure 3.6: LVDT on shear crack in main Span

Figure 3.7: BDI gage along the delta frame

3.1.3 Data Collection

Campbell Scientific data acquisition systems were used to collect data from the sensors. In Spans 5 and 6, two CR1000 dataloggers obtained the data from the sensors. For a 3.6 second event, one gathered the strain transducer and LVDT data at a 33 Hz sample rate when the strain measurement from the trigger

gage, ST01, exceeded 11 με. The other collected the data from the thermocouple at a 2-minute continuous sample rate. A CR1000X datalogger collected the strain transducer and LVDT data in Span 9 in the same manner as the CR1000 in Span 6. In the same fashion, A CR1000X datalogger collected data from span 14. In this case, data was collected when the strain measurement from the trigger gage, ST04, exceeded 11με. Every 24 hours, four different data files were downloaded from the dataloggers: one with Spans 5 and 6 strain transducer and LVDT data, one with Span 6 thermocouple data, one with mobile strain transducer and LVDT data and one for strain transducer and LVDT data of Span 14.

3.2 Data Processing

MATLAB codes were used to measure and process the temperature and corresponding strain and displacement data collected for the Varina-Enon Bridge for each "event." "Bad" incidents were excluded by a set of exclusionary parameters ensuring that at least 11 με were assessed by the trigger strain gages, and that the time difference was less than 2 hours between the measurements of strain and temperature. While it would not be anticipated that the time difference would be more than 2 minutes, this condition was included since a difference of up to 2 hours would be deemed appropriate. The events were also ensured to be sufficiently small to insure no continued drift in the trigger gauge. Furthermore, it was assured that there was no unreasonable shift in strain arising from a 'jump' in the measurements of strain. Moving average filter was used to smoothen the event curves and eradicate the noise. Figure 3.8 and Figure 3.9 shows plots of same event before and after using a five-point moving average filter. Figure 3.10 shows plot of typical event in Span 14. Matlab code outputs an excel spreadsheet consisting of all the values of focus used for effective prestress calculations from field data.

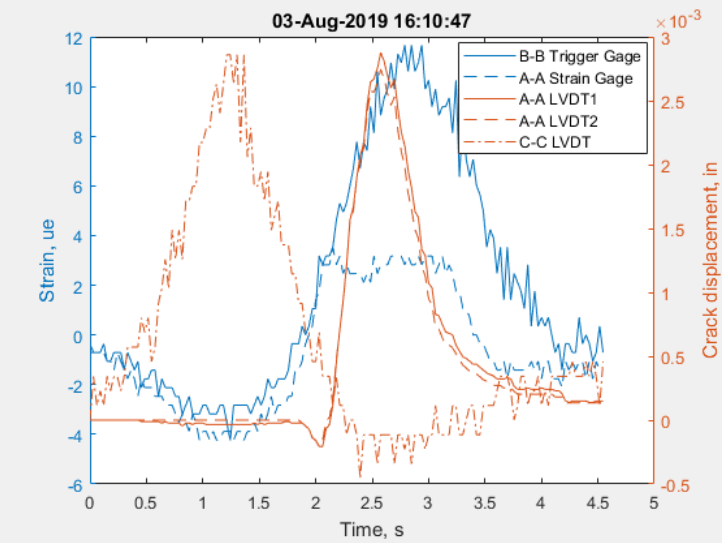

Figure 3.8: Spans 5 and 6 Event Data Without Moving Average Filter

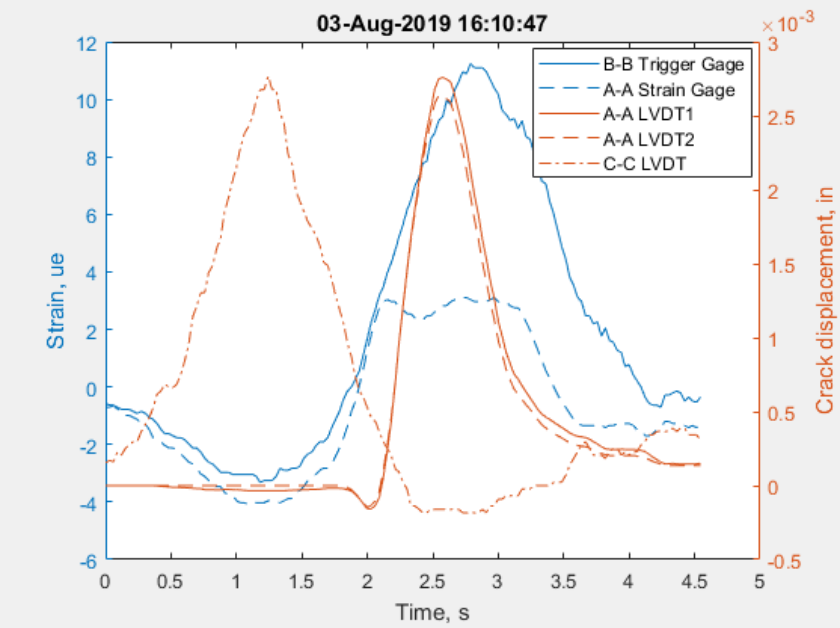

Figure 3.9: Spans 5 and 6 Event Data with Moving Average Filter

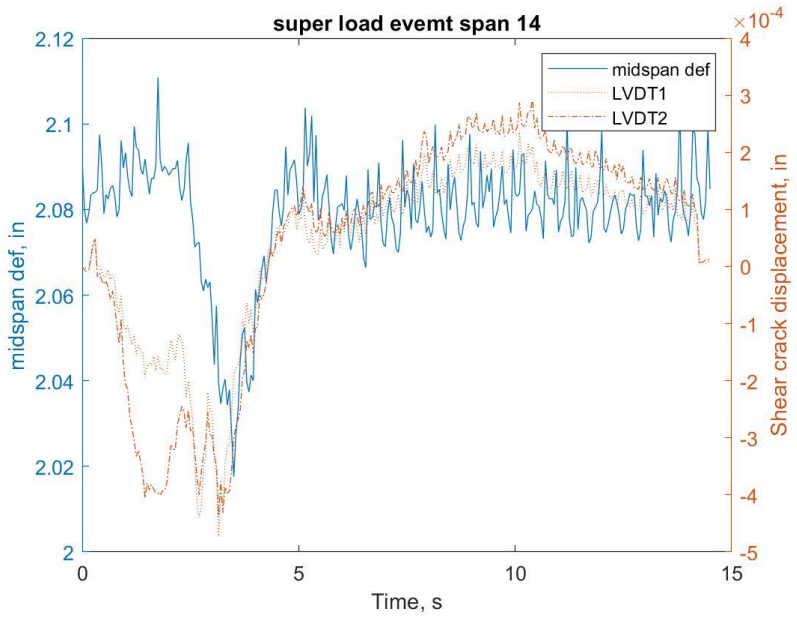

Figure 3.10: Typical event plot for Span 14.

3.3 Finite Element Model

3.3.1 Finite Element Model Overview

Using LARSA 4D, a finite element model shown in Figure 3.11 was generated of the complete Varina-Enon Bridge. Two parallel box girders were modelled on the bridge. For the main span, the substructure, box girders, closure pours, and rigid connections that provided ties between different elements were modeled using beam elements. Stay cables were modeled using cable elements while the delta frames were modeled using truss elements to avoid their participation in longitudinal strength. Although the stays are actually continuous over the pylons via a cradle, two different prestressed cable elements were used for modeling. Stress-stiffening properties have been overlooked because the bridge's high dead load makes stress reversal impossible due to live loads. To model the pot bearings at each end of the main span, spring elements were used. Figure 3.12 shows the FE model properties for delta frame. All the approach spans were also modeled in similar fashion.

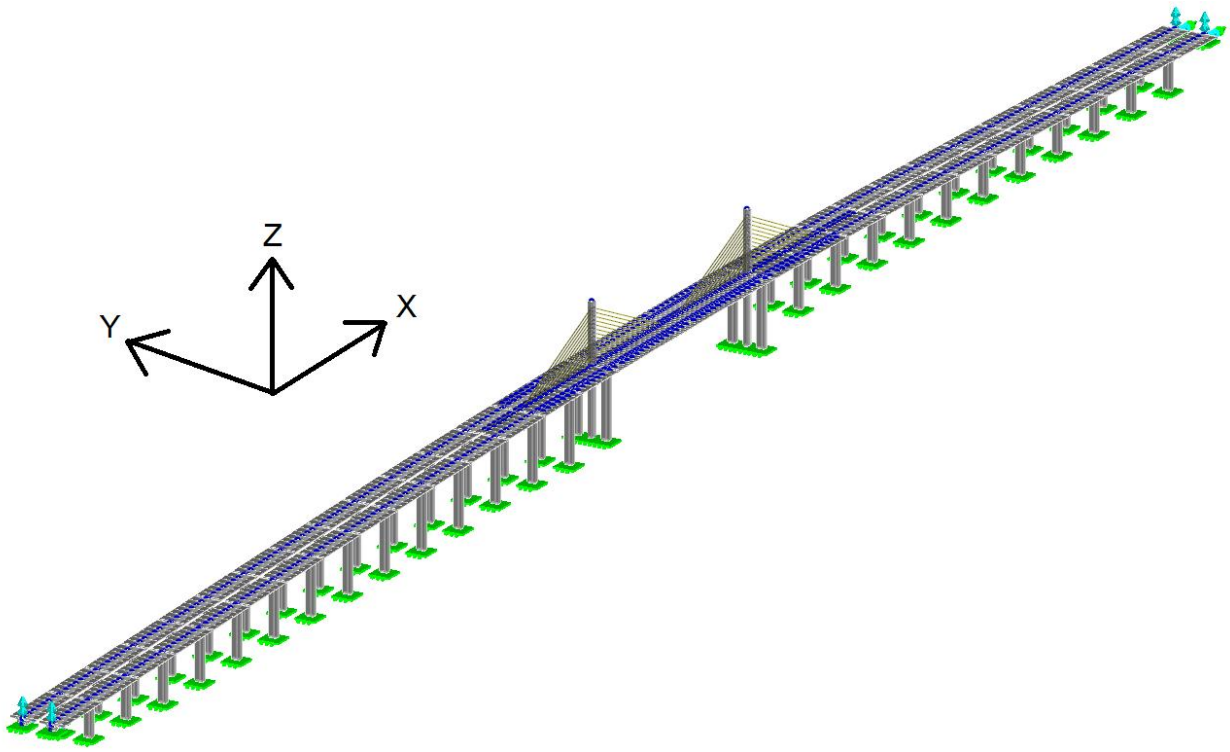

Figure 3.11: Isometric View of Varina-Enon Bridge Full FE Model

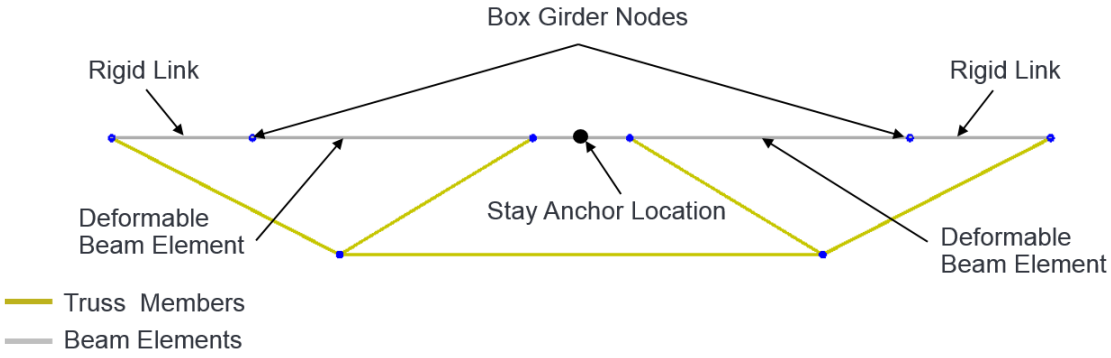

Figure 3.12: Cross Section of Delta Frame in FE Model (Brodsky 2020, with permission)

The model included all longitudinal post-tensioning using the geometry and jacking forces from the design drawings in Appendix A. Table 3.2 shows the material properties used for the model.

Table 3.2: Material Properties for Finite Element Model (Brodsky 2020, with permission)

Property	Value	Source
Concrete Elastic Modulus	5000 ksi	Verified by live load tests (Maguire et al. 2014)
Concrete Strength	6600 psi	Assumed
Tendon Tensile Strength	270 ksi	Design Drawings
Tendon Elastic Modulus	27,400 ksi	As-Built Testing (F&M Engineers 1993)

3.3.2 Staged Construction Analysis

To reflect the segmental construction of the Varina-Enon Bridge, *a time-dependent* staged construction analysis was used. The effect of the placement and stressing of each span as well as the time-dependent effects due to creep, shrinkage, and relaxation were accounted for in this study. Construction phases were broken down into steps and activities in this study. One step representing individual analysis can be broken down into multiple activities like load applying or stressing a tendon.

The full scaled model of Varina-Enon bridge consist of 88 stages in total. Where one stage represented one span the of approach spans and the transition spans. The construction of the main span cantilever was broken into 30 stages according to original construction drawings in shown Appendix B.

In order to account for time-dependent effects, each box girder was incorporated with a casting day into the model. April 29, 1986 was defined as day zero since casting of first girder took place on this day. The year 2019 was represented by Day 12,000 in order to compare the prestress losses expected by the model with those estimated from field data from 2019 and 2020.

3.3.3 Short-Term Prestress Losses

Before the construction stage study, short-term prestress losses are integrated into the FE model. The sum of friction, seating, and elastic shortening losses are presented as these losses. Such losses depend on both the stressing operation and the elastic modulus of the concrete at the time of stressing. Both *curvature friction* and *wobble friction* contribute to friction losses. At the curved portion of a duct, curvature friction is caused when the tendons come into contact with the duct during tensioning. Wobble friction arises when prestressing tendons deviates from defined path. As measured during construction, 0.25 was taken as curvature coefficient (F&M Engineers 1993) while the wobble friction coefficient was assumed as 0.0002 for the internal longitudinal tendons in the main span. Seating losses due to slip of the anchorage when force is transferred from jack to permanent wedges, the slip is user defined. For the Varina-Enon Bridge, from as-built drawings, the anchor set was taken as 3/8 in. (F&M Engineers 1993).

The loss due elastic shortening occurs due to precompression of concrete. It depends on both the total number of tendons in the segment and the stressing sequence. The elastic shortening losses were calculated during the staged construction analysis where the stressing sequence was defined.

3.3.4 Long-term Prestress Losses

Using the CEB-FIP ’90 code expression, the long-term losses using the finite element model were computed during the staged construction analysis (Larsa 4D 2019). The change in strain at each time step were used to calcite the losses due to creep and shrinkage. Depending on the stress distribution, the change in creep strains varies by the depth of the segment, but prestress losses due to creep are determined based on the average change in creep strain over the cross-section depth (Note that this is only because the tendons are unbonded). In the same way as creep losses, shrinkage losses are calculated. Similarly relaxation losses are also calculated during the staged construction analysis (Larsa 4D 2019). Figure 3.13 provides an example of a tendon force profile computed by the finite element model during jacking, after seating, and in 2019 after long-term losses.

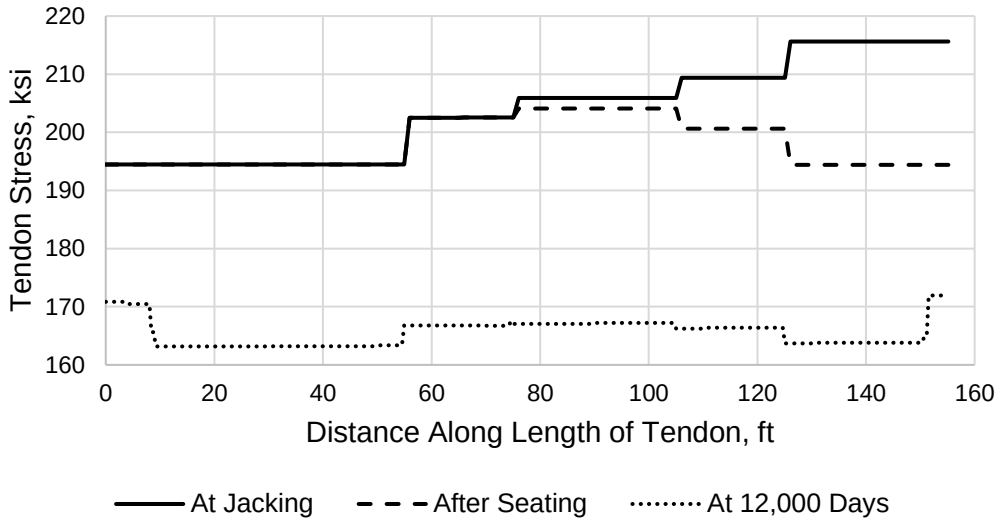

Figure 3.13: Tendon S5-T9L Stress Profile

For more detailed description for the finite element model, refer to Brodsky (2020).

3.4 Effective Prestress Calculations from Field Data

3.4.1 Overview

Data collected from the field was used to calculate the effective prestress in Spans 5, 6, 9, and 11 using the equation (3-1). The calculations were done under the assumption that the total stress at the location of a joint opening is zero.

$$\sigma = -\left(\frac{P_e}{A}\right) - \left(\frac{P_e ey}{I}\right) + \left(\frac{My}{I}\right) + \sigma_{temp} \qquad (3\text{-}1)$$

Where:

P_e = effective prestress force

A = Cross-section area

e = tendon eccentricity from centroid of section

y = centroid of section

I = moment of inertia of section

M = Net moments due to self-weight, live load, secondary prestress, creep, and shrinkage

σ_{temp} = stresses arising from forces due to thermal gradients

Setting the above equation equal to zero, rearranging and further breaking down above equation gives the Equation (3-2), used to calculate the effective prestress from field data (Lindley 2019).

$$P_e = \left(-\sigma_{SE} + \sigma_{con} + \frac{\left(M_{sw} + M_{live} + M_{other}\right)y}{I_{cr}} + \frac{P_{sw} + P_{other}}{A_{cr}}\right)\left(A_{cr} + \frac{I_{cr}}{e_{cr} y_{cr}}\right) \qquad (3\text{-}2)$$

Where:

P_e = effective prestress force

σ_{SE} = self-equilibrating stress at the bottom flange due to thermal gradients

σ_{con} = continuity stress associated with thermal moments

M_{sw} = self-weight moment

M_{live} = live-load moment

M_{other} = moment due to secondary effects from prestressing, creep, and shrinkage

I_{cr} = cracked transformed moment of inertia of the box girder

P_{sw} = axial force due to the self-weight of the structure and restraint of movement at bearings

P_{other} = axial force due to secondary effects from prestressing, creep, and shrinkage

A_{cr} = cracked transformed area of the box girder

e_{cr} = tendon eccentricity from the cracked centroid

y_{cr} = distance from the cracked centroid to the top of the bottom flange of the section

y = distance from the uncracked centroid to the top of the bottom flange of the section

All of the terms on the right-hand-side of the equation were obtained from either field data, known section properties, or a staged construction analysis in the finite element model. The processes of computing

these values are described in the following sections. See Lindley (2019) for sample calculations following these procedures.

3.4.2 Section Properties and Moments

In the calculation of effective prestress force, transformed, partially cracked section properties are used. In the transformed portion, mild steel is not considered because it does not extend through epoxy joints.

Staged construction analysis of the finite element model was used to calculate the dead load moment. The values of dead load moment at Section C-C and Section A-A in Span 5 and 6, Section D-D in span 9 and at section G-G in span 11 are indicated in Figure 3.14, Figure 3.15, and Figure 3.16.

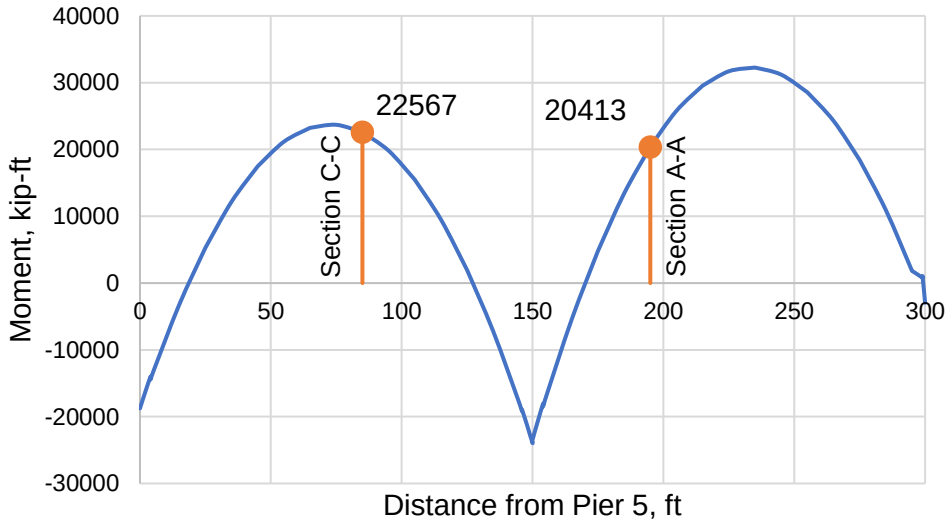

Figure 3.14: Spans 5 and 6 Dead Load Moment

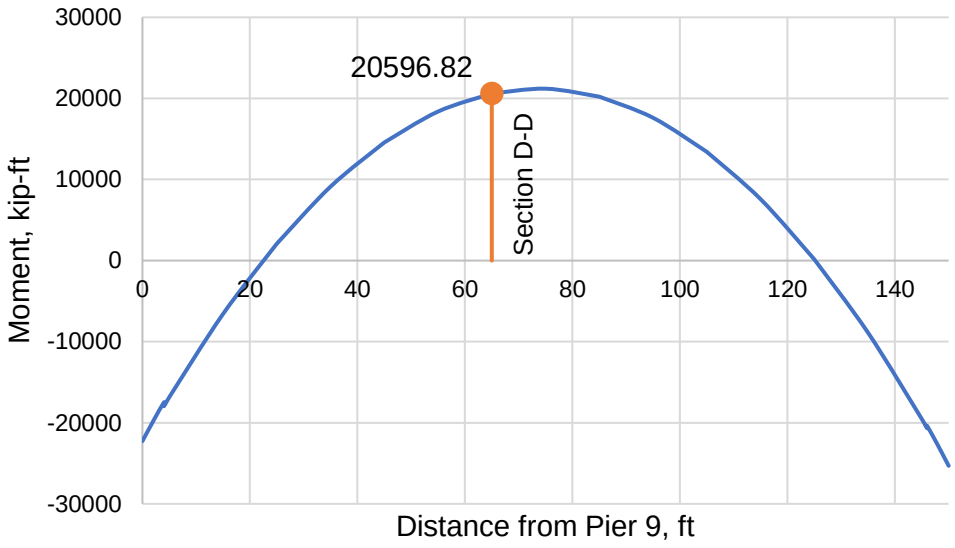

Figure 3.15: Span 9 Dead Load Moment

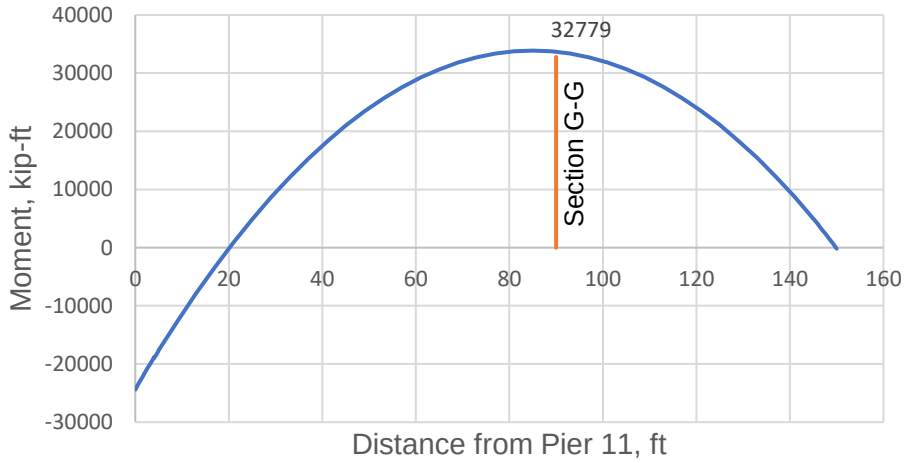

Figure 3.16: Span 11 Dead Load Moment

An influence line analysis in the finite element model was conducted to calculate the live load moments at the locations of interest. This influence line analysis was used to correlate the live load strain measured at the trigger gage to the strains at joint openings. Strain at trigger gage location was measured using strain gages at that location. This strain was used to calculate stress at that location which in turn was used to calculate the moment at that location. The influence line was then used to correlate this moment at trigger gage to find the moment at crack location. Instead of measuring the live load strain directly from the strain measurements adjacent to the opening joints, this approach was used because the bottom flange

could not carry any tension force after it decompressed during a crack-opening event. In the strain calculation, this produced a "plateau" effect which can be seen in Figure 3.6.

The coefficients indicated in Figure 3.17, Figure 3.18 and Figure 3.19 were used to scale the live load strains and obtain the live load moments at the sections of interest.

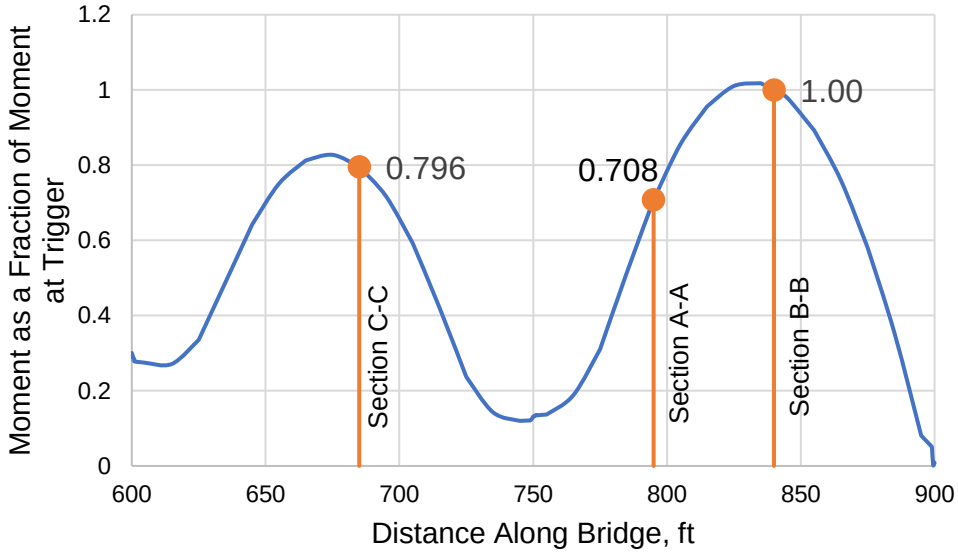

Figure 3.17: Spans 5 and 6 Envelope of Maximum Moments

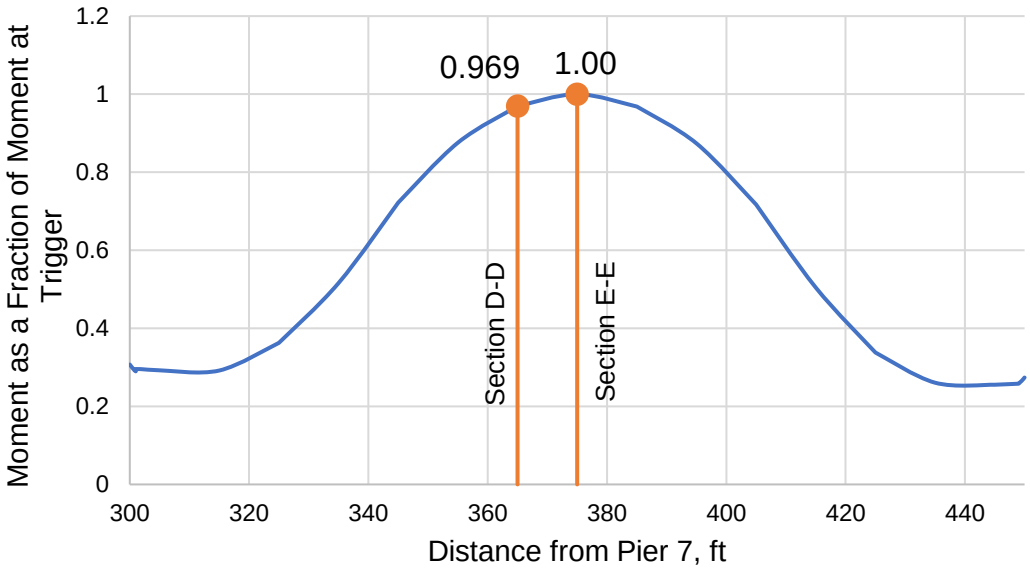

Figure 3.18: Span 9 Envelope of Maximum Moments

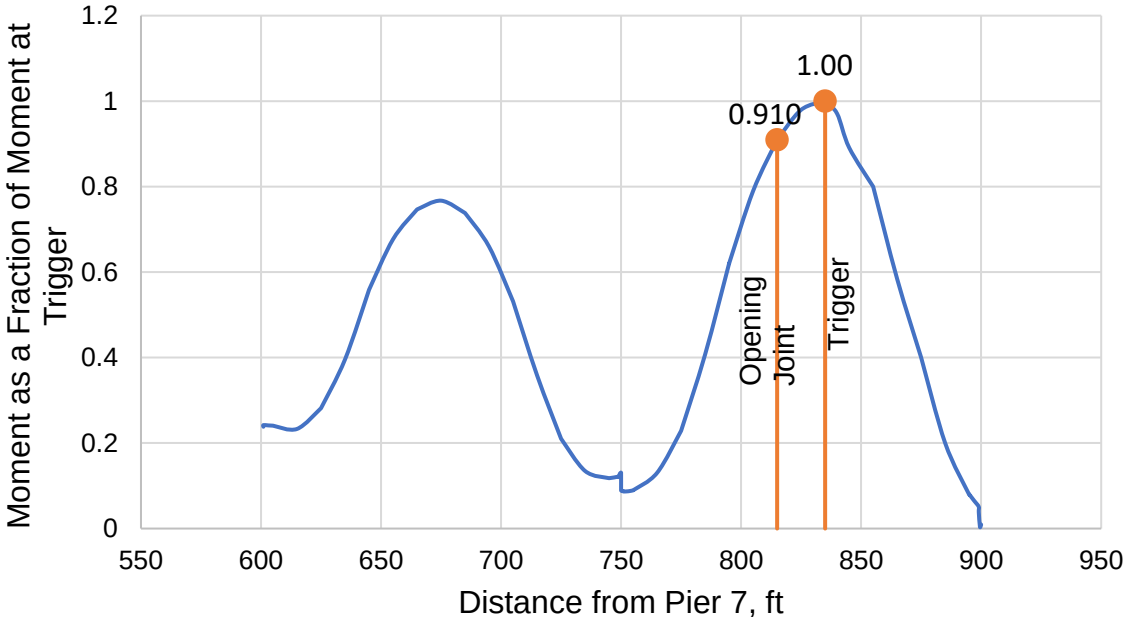

Figure 19: Span 11 Envelope of Maximum Moments

3.4.3 Creep, Shrinkage, and Secondary Prestress Axial Forces and Moments

Prestressing, creep and shrinkage are known as applied structural deformations which lead to both moments and axial forces due redundancies in the structure. In the finite element model, both axial forces and moments at points of interest due to these effects were calculated from a staged construction analysis and can be seen in Table 3.3. The finite element model takes creep and shrinkage factors as input which are used to calculate the axial forces and moments. The primary prestress force gives rise to the secondary prestress force. The creep and shrinkage factors were determined to each be 1.85 using an iteration technique until effective prestress from field and model aligned closely.

Table 3.3: Creep, Shrinkage, and Secondary Prestress Effects at Instrumented Joint Openings

Force/Moment	Section C-C (Span 5)	Section A-A (Span 6)	Section D-D (Span 9)	Section G-G (Span 11)
M_{cr}	1,623 kip-ft	1,960 kip-ft	749.2 kip-ft	1704 kip-ft
P_{cr}	56.10 kip	172.4 kip	-34.90 kip	68.2 kip
M_{sh}	-487.6 kip-ft	310.1 kip-ft	588.9 kip-ft	438.9 kip-ft
P_{sh}	842.7 kip	661.2 kip	839.4 kip	839.4 kip
M_2	20,150 kip-ft	15,830 kip-ft	23,280 kip-ft	26,887 kip-ft
P_2	166.7 kip	163.6 kip	261.2 kip	192.2 kip

3.4.4 Self-Equilibrating Stresses

As discussed in Section 2.5, nonlinear thermal gradients lead to stresses in structures which can be defined as into both self-equilibrating (SE) stresses and thermal continuity stresses.

Self-equilibrating stresses occur due to difference between thermal strains due free expansion of a section and the resultant plane section. The SE stresses can be understood as stresses caused by a thermal gradient in an artificially restrained system plus the stresses caused by the axial load and moment needed to remove the artificial constraints. Calculating SE stresses at the top of the bottom flange by this method begins by eliminating all the inner supports and then artificially restraining the approach structure (Lindley 2019). Thermally induced stresses in the bottom flange was calculated with equation (3-3) (Lindley 2019).

$$\sigma_{t1} = -E\alpha\Delta T_1 \qquad (3\text{-}3)$$

Where:

σ_{t1} = thermally induced stress in the bottom flange when fully restrained

E = modulus of elasticity

α = coefficient of thermal expansion

ΔT_1 = difference in temperature between the coolest location, and TC_1 (Thermocouple at the bottom flange)

To artificially restrain the structure, Equations (3-4) and (3-5) were used to calculate the axial force and moments applied at ends of structure. (Lindley 2019).

$$P = \sum_{i=1}^{18} E\alpha\Delta T_i A_i \qquad (3\text{-}4)$$

$$M = \sum_{i=1}^{18} E\alpha\Delta T_i A_i Y_i \qquad (3\text{-}5)$$

Where:

ΔT_i = difference in temperature between TC_i, and TC_{cool}

A_i = tributary area of thermocouple i, as presented in Table 3.1

Y_i = distance of thermocouple i from the center of gravity of the section(Table 3.1)

Finally, by taking a summation of the thermally induced stress in the lower flange, the stress due to the restraining axial force, and the stress due to the restraining axial moment, the total self-equilibrating stresses were determined. Equation (3-6) regulated this calculation (Lindley 2019).

$$\sigma_{SE} = \sigma_t + \frac{P}{A} + \frac{My}{I} \qquad (3\text{-}6)$$

3.4.5 Thermal Continuity Forces

As discussed in Section 2.4, the application of a non-linear thermal gradient on a redundant structure, develops thermal continuity stress in structure. Therefore, these forces were calculated considering the internal supports. Since a large number of thermal gradients is being considered, In the finite element model, a constant unit moment and axial force at the ends of Spans 1-6 and Spans 7-12 were applied and the equation (3-4) and equation (3-5) were scaled using the coefficients obtained for sections of interest. The bending moment diagrams along with the coefficients used to scale in Span 5, 6, 9, and 11 are shown in Figure 3.20 and Figure 3.21.

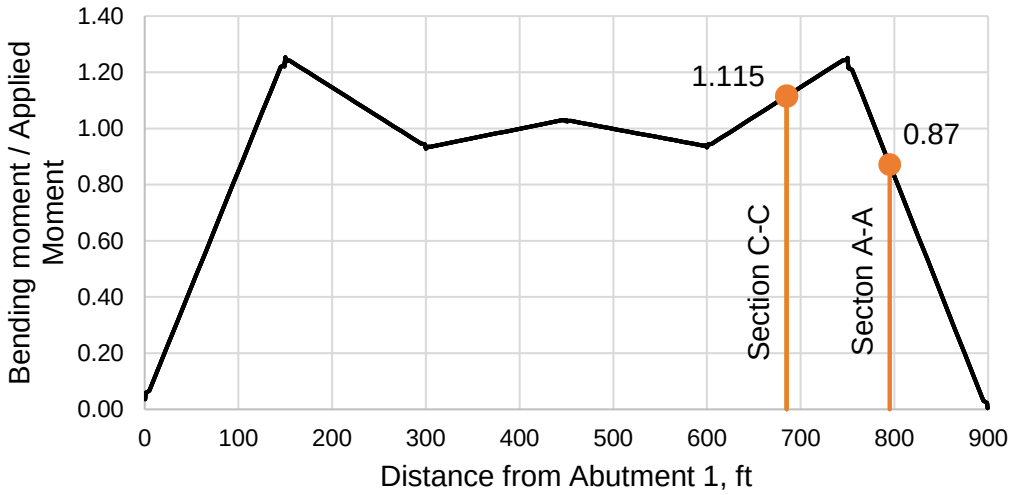

Figure 3.20: Thermal Continuity Moment as a Fraction of Applied Moment, Spans 1-6

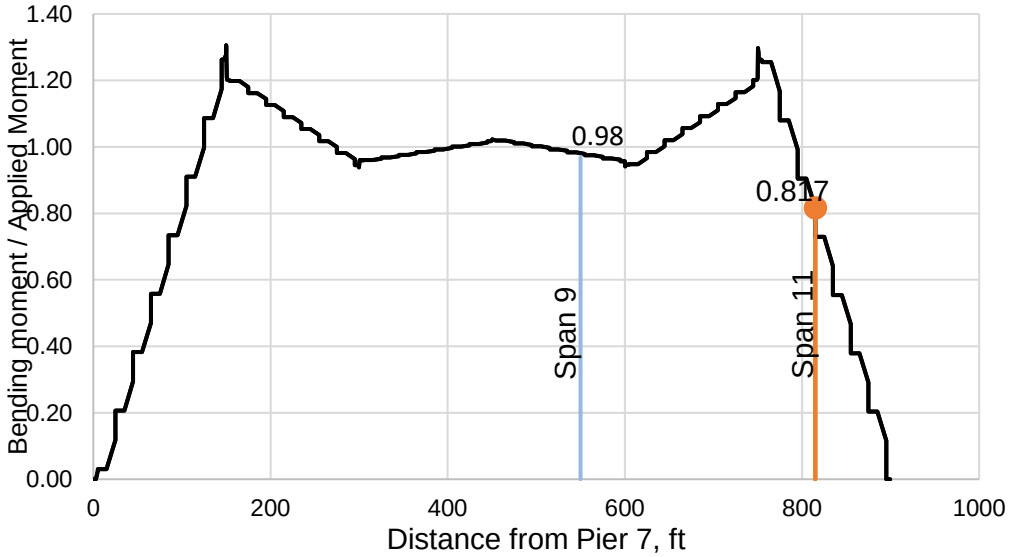

Figure 3.21: Thermal Continuity Moment as a Fraction of Applied Moment, Spans 7-12

3.5 Validation of FE Model

The datalogger programs were modified for the case of a super load crossing the bridge. For a super load, it was more desirable to collect data from all dataloggers during the entire time the super load was crossing the bridge. The Data Acquisition System (DAS) was modified to collect the data continuously for the duration of super load crossing. This information was useful for more precise capturing of the crossing and further validation of the finite element model. Since both the load crossings took place in night or early morning, the thermal gradient was expected to be small and it was expected to have minimal effect.

3.5.1 Super Load 1 (SL1)

At approximately midnight on September 23, 2020, a large load shown in Figure 3.22 crossed the Varina-Enon Bridge. The response of the bridge to the load was monitored by three data acquisition systems which are monitored by Virginia Tech.

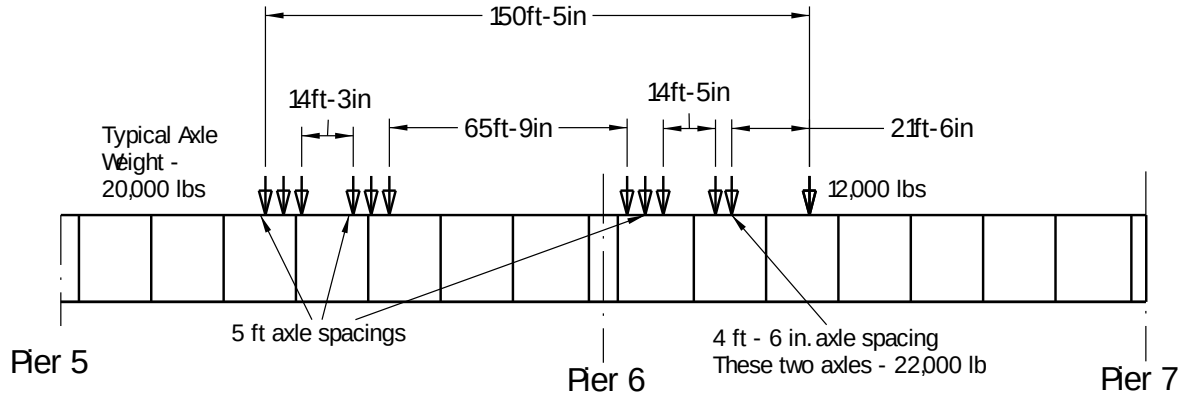

Figure 3.22: Axle Spacings and Loads, shown on two spans for comparison to span length.

As can be seen in the Figure 3.22, There were five axle groupings separated, and the total length of the truck was 150 ft – 5 in. The rear axle group carried a total of 120,000 lb. so did the front axle group, for a total of 240,000 lb.

3.5.2 Super Load 2 (SL2)

On December 22, 2020, a series of heavy loads were crossed over the Varina-Enon Bridge to further investigate the performance of the bridge under heavy live loads. These live loads were modeled in the FE

model also. Two different load combinations were used for these live loads. For the load combination 1 (LC1) two lowboys were used in extreme left and middle lane while for load combination 2 (LC2) along with the previously used two lowboys, VDOT dump was used in 3rd lane. Load crossings using each load combination was done thrice to ensure accuracy. Figure 3.23 and 3.24 shows the axle loading and Figures for trucks used for these live load tests.

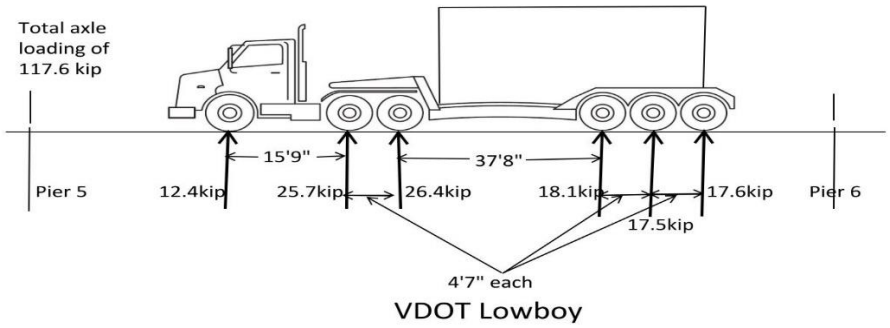

Figure 3.23: Axle Spacings and Loads for SL2 (VDOT Lowboys)

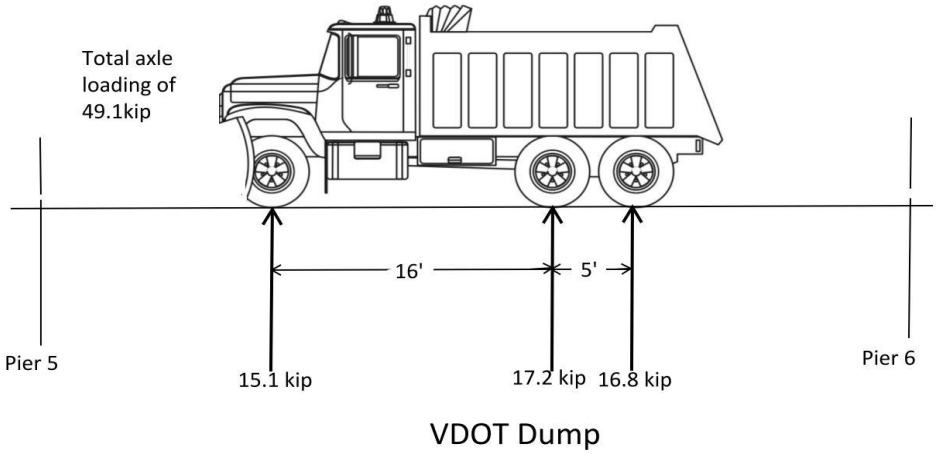

Figure 3.24: Axle Spacings and Loads for SL2 (VDOT Dumps)

Chapter 4. Results and Discussion

Results obtained following the methodology in previous chapters are presented in this chapter. In the first section, validation of FE model done by Brodsky (2020) is shown along with the validation using the two super load crossings discussed in section 3.4.

The prestress losses predicted from FE model and calculated using field data at the joint opening locations in Spans 5, 6, 9, and 11 are shown in second section. To understand if the cracking of bridge is expected at all, the third section shows a comparison of "as designed" to "as behaving" of the bridge. Finally, A comparison of FE model results and field data results in presented in fourth section.

4.1 Validation of Finite Element Model

4.1.1 Main Span Validation

4.1.1.1 Previous Validation of Main span

Brodsky (2020) validated the main span using the results obtained during the during live-load tests conducted by Duemmel et al. (1992). Table 4.1 and Table 4.2 show the results obtained through that validation. The percent difference between the results of the FE and the measurements in the field ranges from 7.93 percent to 20.89 percent, which is deemed acceptable. Therefore, the model was considered to adequately represent the actual structure's behavior. For more details on this, refer to Brodsky (2020).

Table 4.1: Measured and Computed Lower Flange Strains in Segment 33 (Brodsky 2020, with permission)

Load Configuration	Segment 33 Lower Flange Strain (με)		Percent Difference
	Live-Load Test Results	FE Model Results	
NBL	-8	-9.27	15.91
SBL	-3.75	-4.35	15.98

Table 4.2: Measured and Computed Upper Flange Strains in Segment 62(Brodsky 2020, with permission)

Load Configuration	Segment 62 Upper Flange Strain (με)		Percent Difference
	Live-Load Test Results	FE Model Results	
NBL	-0.25	-0.20	20.89
SBL	-0.45	-0.41	7.93

4.1.1.2 Validation under super load.

The response of the bridge to the super load 1 (SL1) shown in Figure 3.22 crossing was monitored by three data acquisition systems which are monitored by Virginia Tech. The load was modeled in FE model and results from field data and FE data were compared to validate the main span unit of FE model. Table 4.3 shows the comparison of mid span deflection. There was a 25.27 percent difference between measured deflection and that calculated from the FE model. This is considered satisfactory. The span only deflected about 0.068 in. under the load. The shear crack near pier 14 closed when the truck was directly above the crack location by roughly 0.0004 in. Figure 4.1 shows the plot of typical data obtained during the crossing. As shown in Figure 4.1, the shear crack opens by 0.0003 in. when the truck has crossed the crack location.

Table 4.3: Measured and Computed midspan deflections for span 14

Load Configuration	Midspan deflection (in)		Percent Difference
	Live-Load Test Results	FE Model Results	
NBL	-0.068	-0.091	25.27

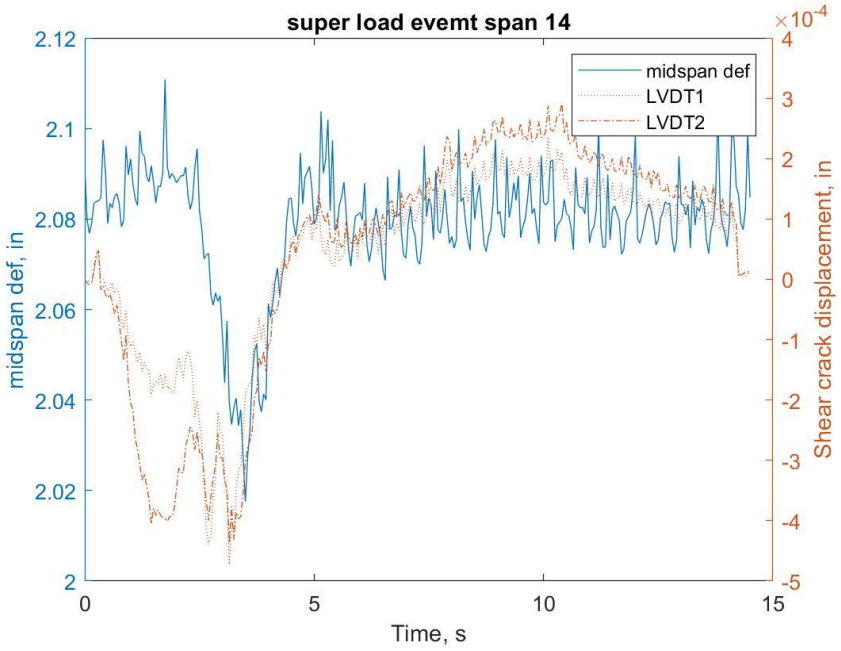

Figure 4.1: Response of Span 14 to the Super load 1(SL1)

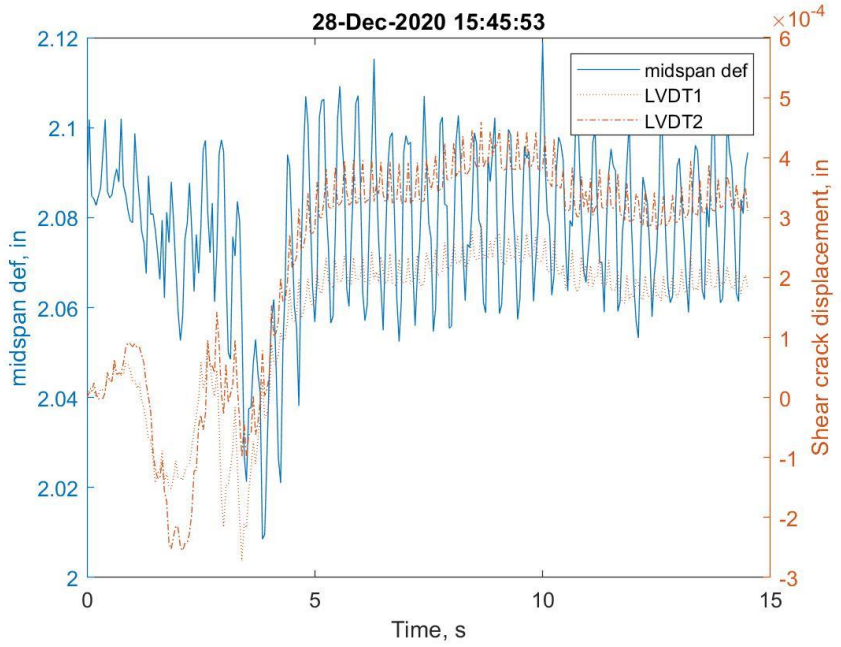

Figure 4.2: Response of Span 14 to the Super load 2(SL2, LC1)

On December 22, 2020, a series of heavy loads (SL2) shown in figure 3.23 and 3.24 were crossed over Varina-Enon Bridge to better investigate the performance of bridge under heavy live loads. These live loads are modeled in the FE model also. The results obtained from field data and FE model were compared to

validate the FE model are shown in Table 4.5. The percentage difference of 20.51% and 28.13% is considered small as the values of deflection are small. Figure 4.2 shows the typical plot of event due to SL2 for Span 14.

Table 4.5: Measured and Computed midspan deflections

Load Configuration	Midspan deflection (in)		Percent Difference
	Live-Load Test Results	FE Model Results	
LC1	0.062	0.078	20.51
LC2	0.069	0.0960	28.13

4.1.2 Approach Span Validation under Super Loads.

During the super load 1 (SL1) crossing on September 23, 2020, the strains were measured at top and bottom of the box girder. The comparison of these strains with those obtained from FE model at the mid-span of Span 6 and at the location of the trigger gauge (0.4L) in Span 6 respectively was investigated to validate the FE model. Figure 4.3 shows the plot of the event for Span 6. It can be seen from Figure 4.3 that the event plot has five spikes in the BDI2 gage, which is on the top slab, and each spike represents an axle directly above the gage.

The heavy load crossings that took place on December 22, 2020 (SL2) were also studied in a similar fashion. Two new LVDTs were installed at the bottom of the bottom flange of span 6 in order to compare the joint displacements at the top and bottom of the bottom flange. As seen from Figure 4.4, the crack opening at the top and bottom of the bottom slab are not significantly different. Table 4.6 and Table 4.7 shows the results of this comparison. A typical plot of the event for Span 6 due to SL2 is shown in Figure 4.4.

Table 4.6: Measured and Computed Lower Flange Strains in span 6

Load Configuration	Average of Mid-Span of span 6 strain((με)		Percentage difference
	Live-Load Test Results at bottom of box girder	FE model Results at bottom of box girder	
September 23, 2020	16	23.4	31.62
December 22, 2020(LC1)	23.5	29.1	19.24
December 22, 2020(LC2)	34.1	43.6	21.78

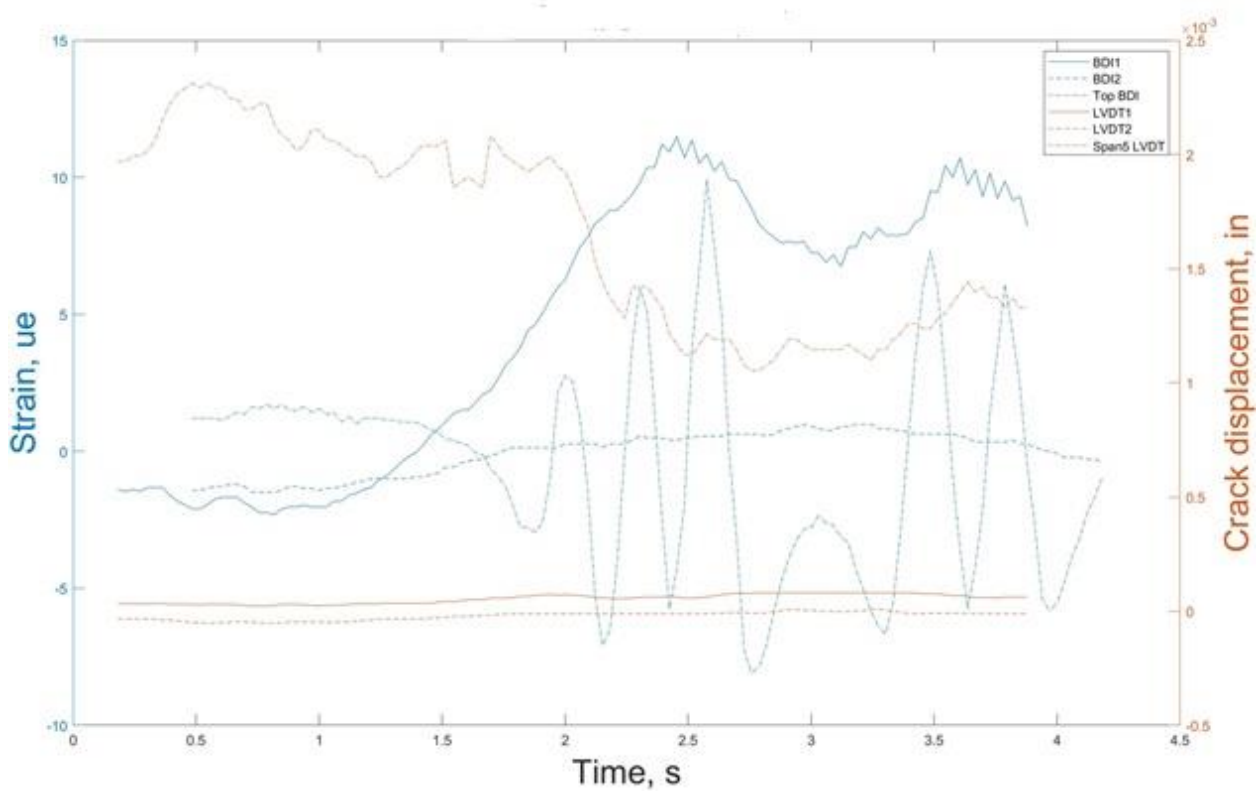

Figure 4.3: Response of Span 6 to the Super load 1(SL1)

Table 4.7: Measured and Computed Lower Flange Strains in span 6 at trigger gauge.

Load Configuration	Average span 6 strain at Trigger (με)				Percentage difference	
	Live-Load Test Results		Finite Element model Results			
	Bottom of box Girder	Top of box Girder	Bottom of box Girder	Top of box Girder	Bottom of box Girder	Top of box Girder
September 23, 2020	17.6	-7.8	27.4	-9.6	35.76	18.75
December 22, 2020(LC1)	31.7	-12.2	34.61	-14.4	8.4	15.27
December 22, 2020(LC2)	36.1	-13.4	49.03	-17.4	26.37	22.9

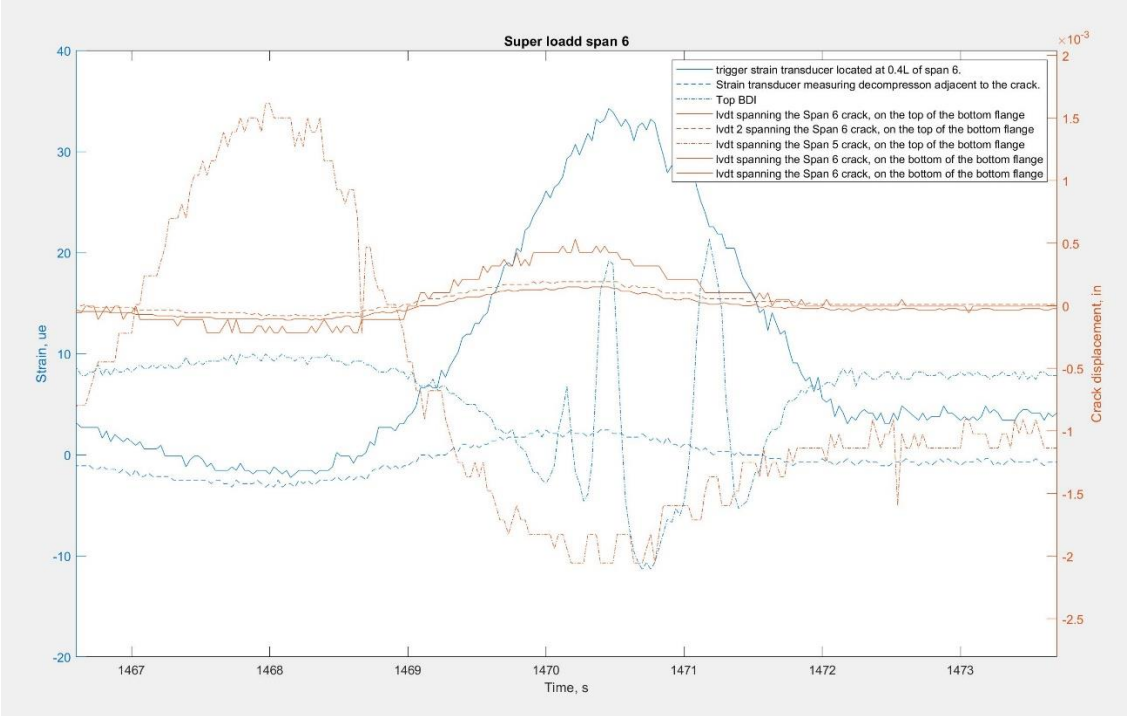

Figure 4.4: Response of Span 6 to the Super load 2(SL2, LC1)

Discrepancies may be due to the fact that linear elastic behavior is assumed by the model, but under heavy loadings, the structure can undergo nonlinear behavior. Furthermore, the crack openings in the bottom flange may have altered the field readings. Overall, comparison of these results confirms the validation of FE model of approach span. Also, the percentage differences listed in Table 4.6 and Table 4.7 are not high as the values are in macrostrains and are very small.

4.2 Effective prestress from FE and Field data

The total loss in prestress is taken as the difference between prestress force at the time of interest and prestress force at time of jacking. A time-dependent, staged-construction analysis using the CEB-FIP ’90 code expressions gave the prestressing force at various times. Anticipated prestress losses according to the CEB-FIP ’90 code expression were given by the finite element model. The average tendon stress profiles obtained from the model for Spans 5, 6, 9, and 11 are shown in Figure 4.5, Figure 4.6, Figure 4.7, and Figure 4.8, respectively. For each joint opening location considered, Table 4.8 presents the jacking stresses, effective prestress values at 12,000 days, and prestress losses obtained from the finite element model. The prestress force while jacking was from the design drawings in Appendix A.

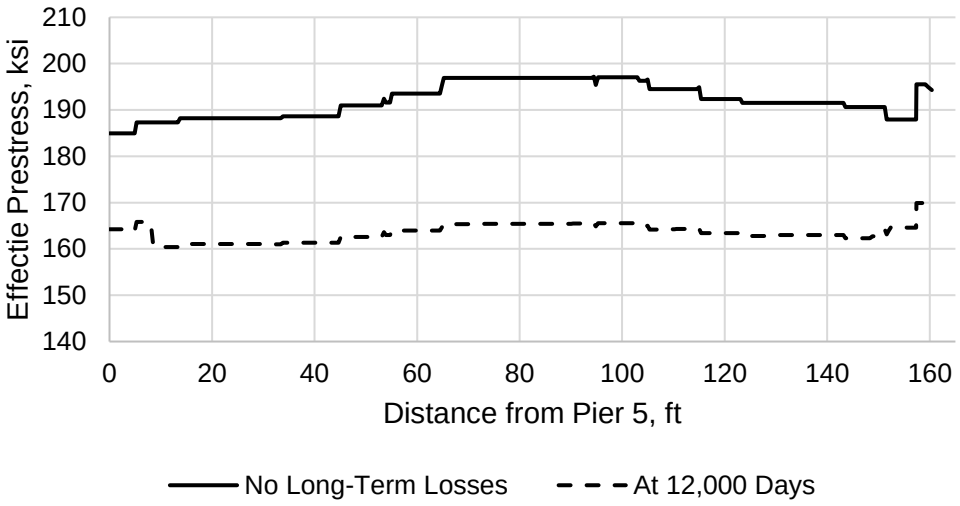

Figure 4.5: Span 5 Average Tendon Profiles

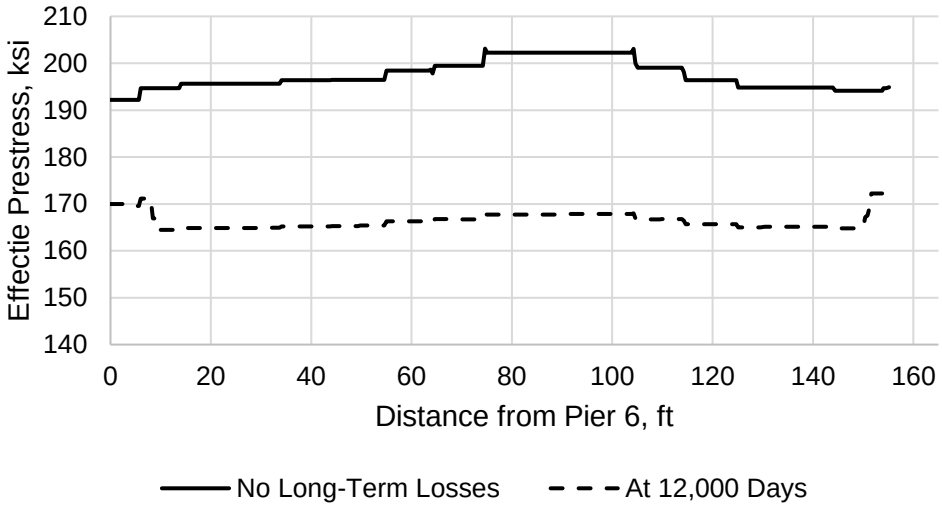

Figure 4.6: Span 6 Average Tendon Profiles

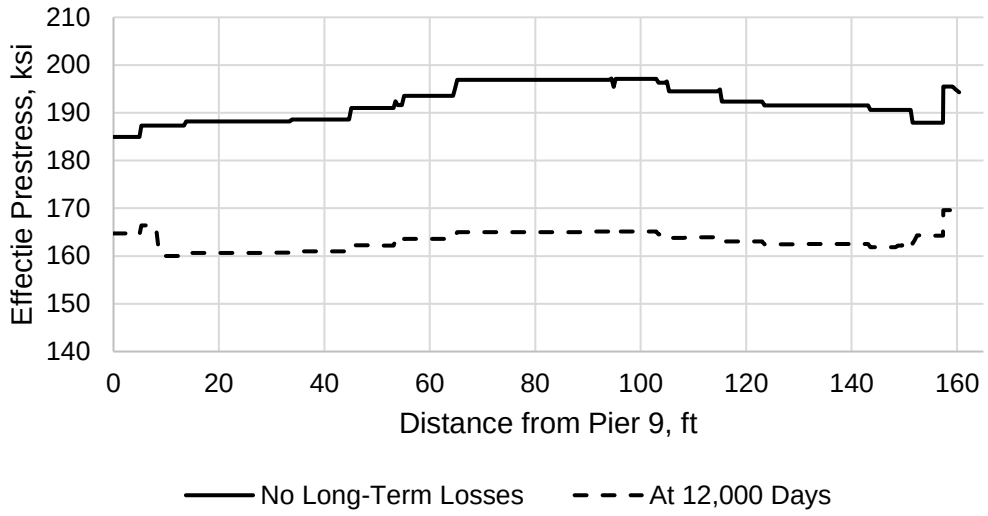

Figure 4.7: Span 9 Average Tendon Profiles

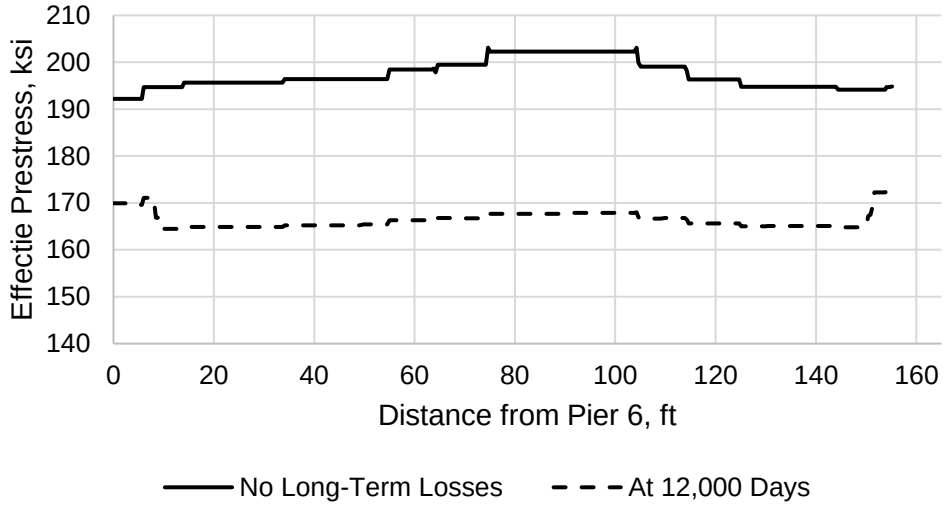

Figure 4.8: Span 11 Average Tendon Profiles

Table 4.8: Prestress Losses per FE Model

Location	Average Jacking Stress (ksi)	Average Prestress at 12,000 Days (ksi)	Average Prestress Loss (ksi)
Section C-C, Span 5	210.3	165.4	44.9
Section A-A, Span 6	213.1	165.3	47.8
Section D-D, Span 9	210.3	165.0	45.3
Section D-D, Span 11	210.3	165.1	45.2

The average prestress force at the end of 12000 days was calculated by integrating the effective prestress curve over the length and then dividing by the length.

According to the method discussed in Chapter 3, the data obtained from field data acquisition system was processed through MATLAB codes to back calculate the effective prestress force from the joint opening data. The effective prestress force was compared with finite element model prestress results.

4.2.1 Span 5 Effective Prestress from Field Data

From a total of 18,124 crack-opening recorded from May 16, 2019 to February 3, 2021, the mean of the effective prestress values obtained for Span 5 at the crack location was (Section C-C) 148.01 ksi. The standard deviation of the data was 6.9 ksi. The most extreme crack opening recorded was 0.0264 in., however most of the cracks were much smaller than this. Figure 4.9 shows the distribution of effective prestress values with corresponding crack openings. In Figure 4.10, a histogram showing the distribution of measured prestress values is depicted.

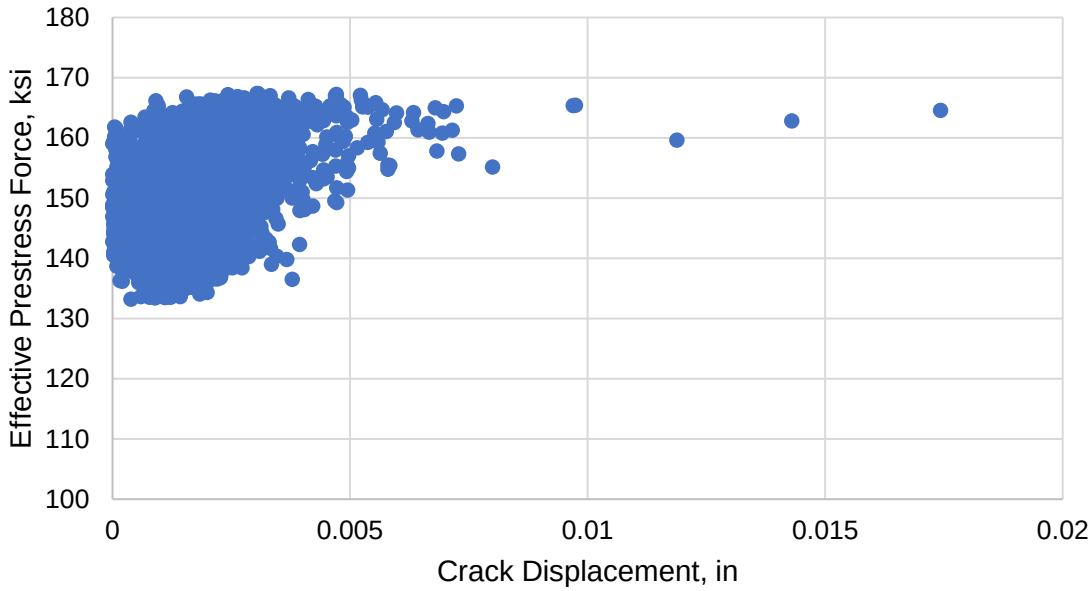

Figure 4.9: Effective Prestress vs. Crack Displacement for all Span 5 Events

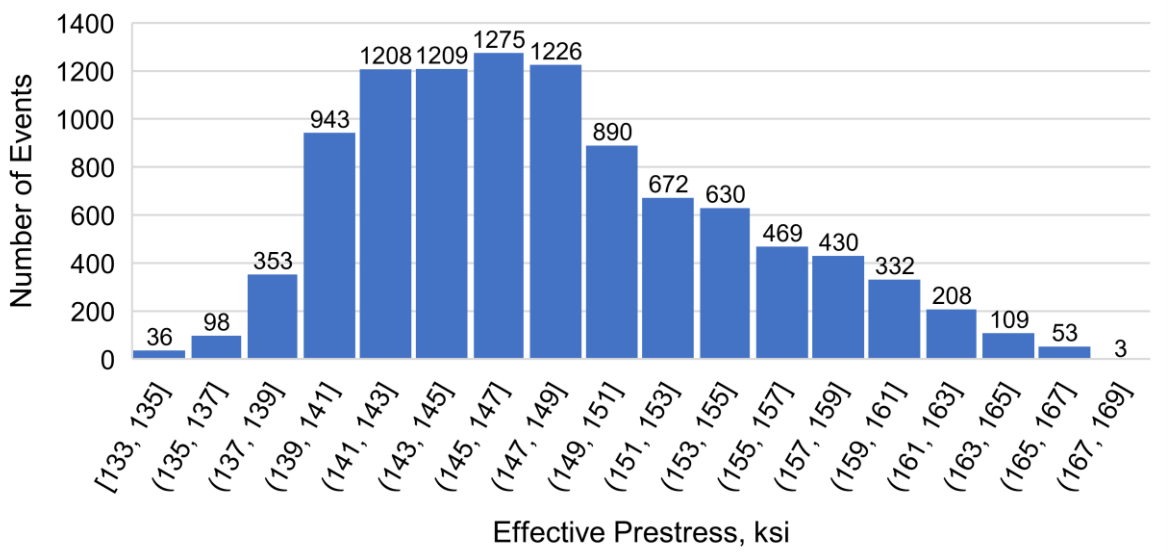

Figure 4.10: Histogram of Prestress Values for all Span 5 Events

The plot in Figure 4.9 shows that as the corresponding crack widths decrease, the scatter of prestress estimates increases. The scatter in the prestress value reaches 30 ksi, as crack openings approach zero. The events with small crack opening were discarded as noise and random selection of a threshold equal to 0.004 in. crack width was selected.

The plot in Figure 4.11 shows the effective prestress values for events with a crack displacement greater than or equal to 0.004 in. The average value of effective prestress forces for these events was 161.1 ksi. The standard deviation of these events is 5.3 ksi and the median is 159 ksi.

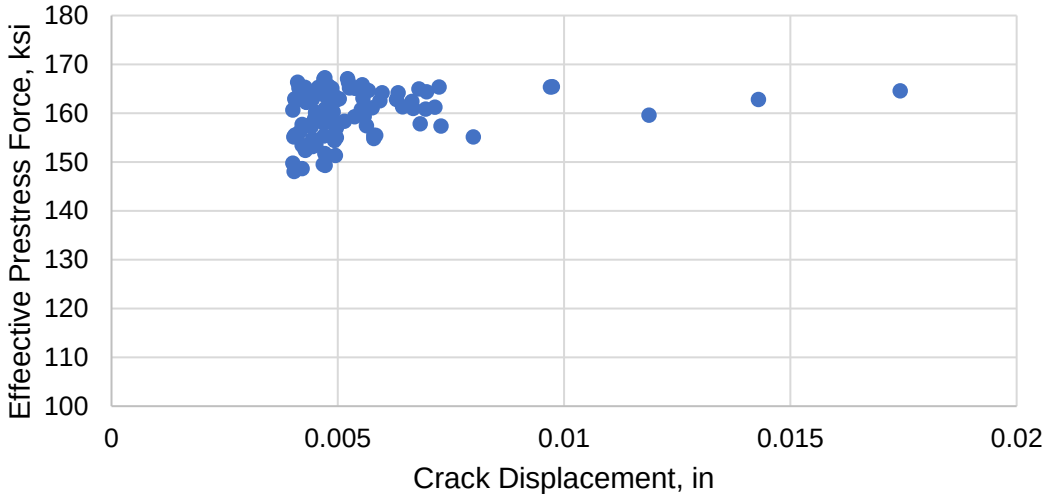

Figure 4.11: Effective Prestress vs. Crack Displacement for Span 5 Events with Corresponding Crack Openings of 0.004 in. or Greater

4.2.2 Span 6 Effective Prestress from Field Data

From a total of 18,124 crack-opening recorded from May 16, 2019 to February 3, 2021, the mean of the effective prestress values obtained for Span 6 at the crack location was (Section A-A) 153.3 ksi. The standard deviation of the data was 6.2 ksi. The most extreme crack opening recorded was 0.01 in., however most of cracks were significantly smaller than this. Figure 4.12 shows the distribution of effective prestress values with corresponding crack width. In Figure 4.13, a histogram showing the distribution of measured prestress values is depicted.

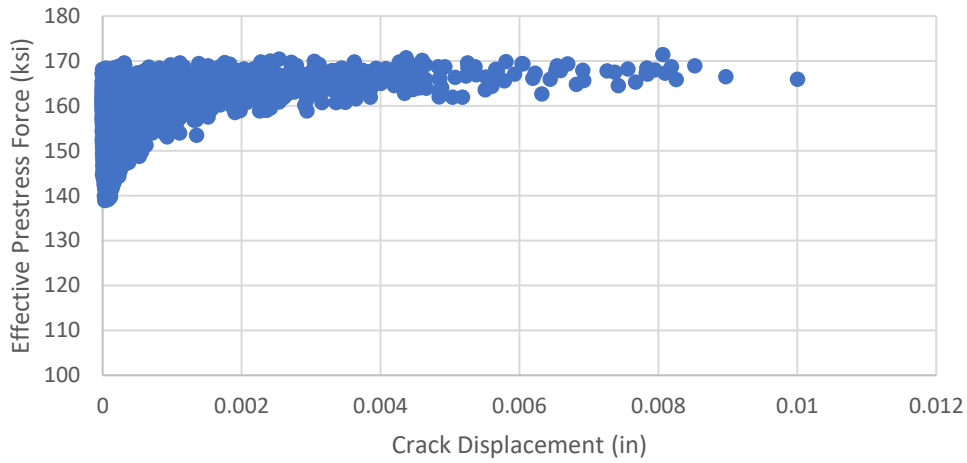

Figure 4.12: Effective Prestress vs. Crack Displacement for all Span 6 Events

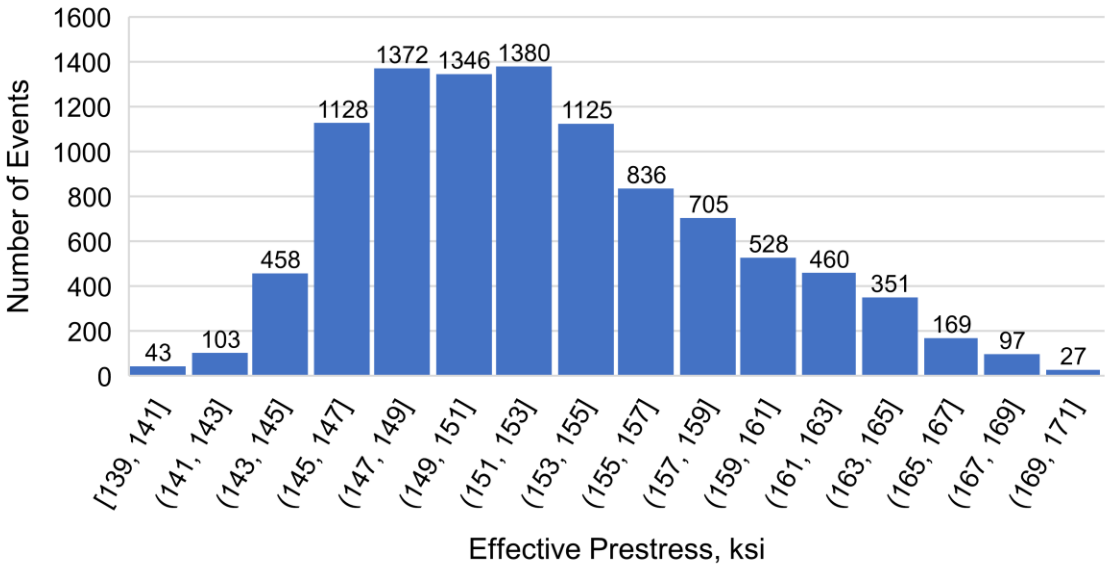

Figure 4.13: Histogram of Prestress Values for all Span 6 Events

Again, the plot in Figure 4.12 shows that as the corresponding crack widths decrease, the scatter of prestress estimates increases. The scatter in the prestress value reaches 30 ksi, as crack openings approach zero. This time the threshold value of crack as can be seen from the Figure 4.11 is 0.002. The events with small crack opening were discarded as noise.

The plot in Figure 4.14 shows the effective prestress values for events with a crack displacement greater than or equal to 0.002 in. The average value of effective prestress forces for these events was 165.7 ksi. The standard deviation of these events is 5.3 ksi and the median is 159 ksi.

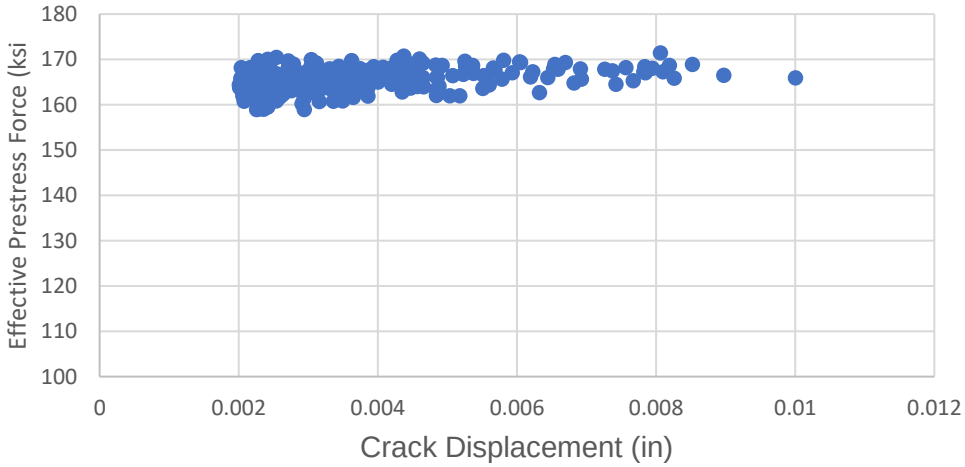

Figure 4.14: Effective Prestress vs. Crack Displacements for Span 6 Events with Corresponding Crack Openings of 0.002 in. or Greater

4.2.3 Span 9 Effective Prestress from Field Data

The data for crack at section D-D on this span was collected from March 12, 2020 to June 3, 2020. A total of 1302 crack-opening events were observed where the mean value of effective prestress force was found to be 155.3 ksi. The standard deviation of the prestress forces was 5.7 ksi. The most extreme crack opening recorded was 0.00151 in., yet again most of cracks were altogether smaller than this. Figure 4.15 shows the distribution of effective prestress values with corresponding. In Figure 4.16, a histogram showing the distribution of measured prestress values is depicted.

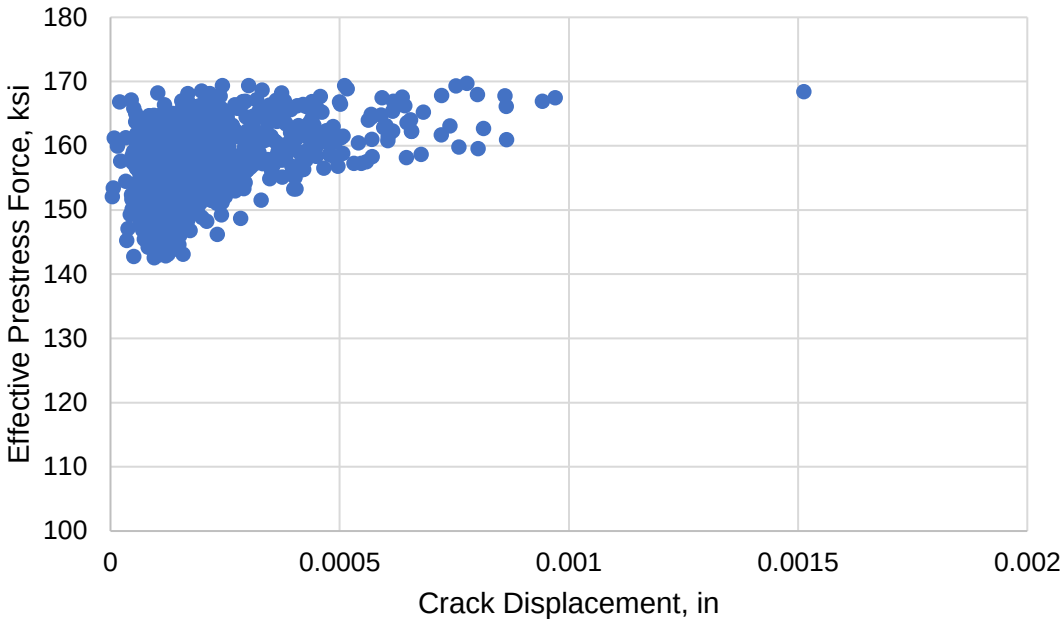

Figure 4.15: Effective Prestress vs. Crack Displacement for all Span 9 Events

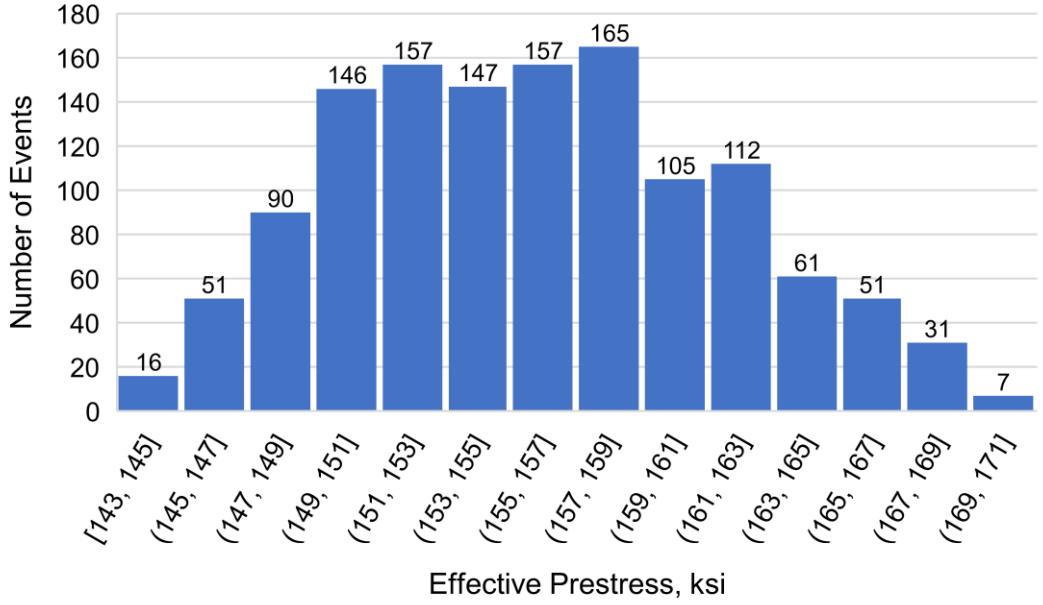

Figure 4.16: Histogram of Prestress Values for all Span 9 Events

Again, the plot in Figure 4.15 shows that as the corresponding crack widths decrease, the scatter of prestress estimates increases. The scatter in the prestress value reaches 25 ksi, as crack openings approach zero. This time the threshold value of crack as can be seen from the Figure 4.17 is 0.0005. The events with small crack opening were discarded as noise.

The plot in Figure 4.17 shows the effective prestress values for events with a crack displacement greater than or equal to 0.0005 in. The average value of effective prestress forces for these events was 165.7 ksi. The standard deviation of these events is 3.6 ksi

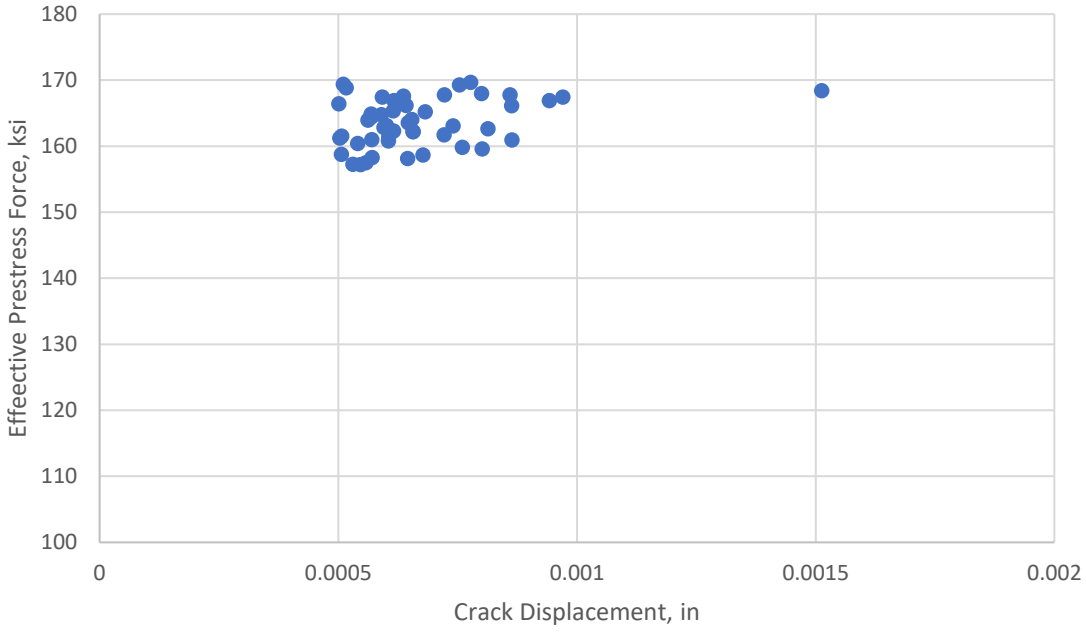

Figure 4.17: Effective Prestress vs. Crack Displacement for Span 9 Events with Corresponding Crack Openings of 0.005 in. or Greater

4.2.4 Span 11 Effective Prestress from Field Data

The data for crack at section G-G on this span was collected from June 12, 2020 to February 3, 2021. A total of 11,401 crack-opening events were observed where the mean value of effective prestress force was found to be 160.1 ksi. The standard deviation of the prestress forces was 3.1 ksi. The most extreme crack opening recorded was 0.0025 in., yet again most of cracks were altogether smaller than this. Figure 4.18 shows the distribution of effective prestress values with corresponding. In Figure 4.19, a histogram showing the distribution of measured prestress values is depicted.

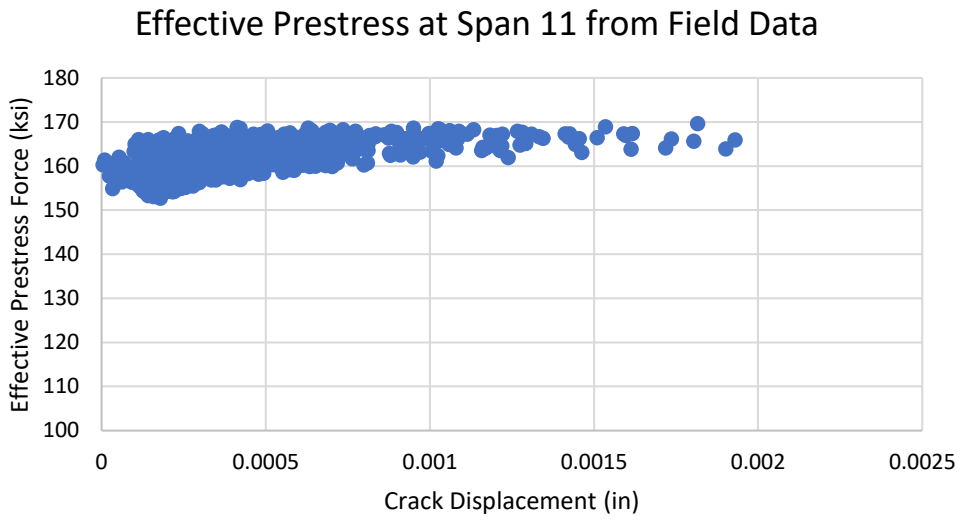

Figure 4.18: Effective Prestress vs. Crack Displacement for all Span 11 Events

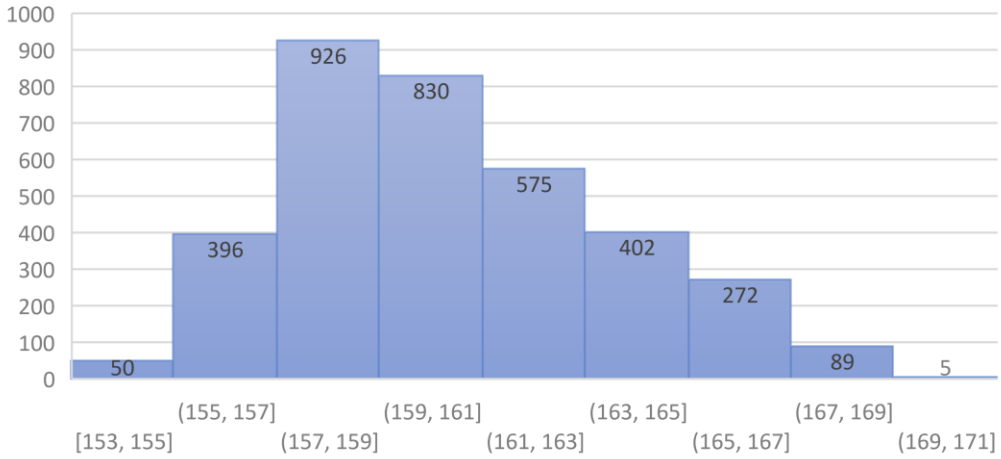

Figure 4.19: Histogram of Prestress Values for all Span 11 Events

Figure 4.18 indicates that, again, there is more scatter in the effective prestress values when the crack displacements are smaller. Events corresponding to crack openings smaller than 0.0004 in. were discarded since the effective prestress calculations begin to converge above this value. Figure 4.20 presents a plot of effective prestress values versus corresponding crack displacements for crack openings greater than or equal 0.0004 in. The average of the effective prestress values for these events is 163.7 ksi with a standard deviation of 2.5 ksi.

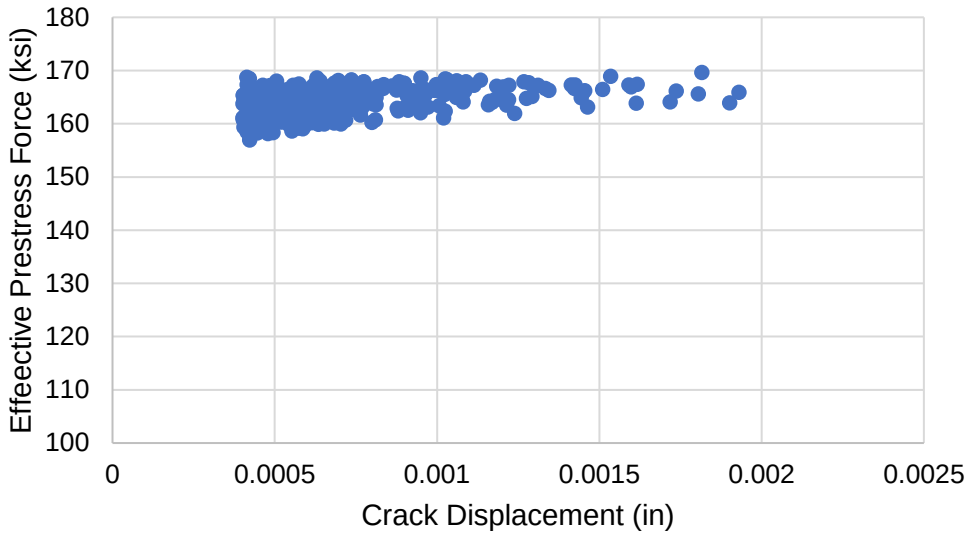

Figure 4.20: Effective Prestress vs. Crack Displacement for Span 11 Events with Corresponding Crack Openings of 0.004 in. or Greater

4.3.5 Field Data Results Summary

Table 4.9 provides a summary of the results obtained from the measurements using field data considering the events with joint-opening greater than threshold values.

Table 4.9: Prestress Losses per Calculations From Field Data

Location	Average Jacking Stress (ksi)	Average Prestress at 12,000 Days (ksi)	Average Prestress Loss (ksi)
Section C-C, Span 5	210.3	160.3	50.0
Section A-A, Span 6	213.1	165.1	48.0
Section D-D, Span 9	210.3	163.6	46.7
Section G-G, Span 11	210.3	163.7	46.6

4.3 "As designed" vs "as Behaving" comparison.

Since the Varina-Enon bridge was deigned according to 1978 specifications, a detailed study was required to be conducted to understand if the "as designed" bridge was expected to crack. Also, it was important to know what were the reasons of crack occurring as there should never have been longitudinal tension anywhere in the bridge, so cracking would not be expected. The factors like excessive prestress loss, level of thermal and live loads needed to be investigated to understand the reasons for this behavior of the bridge.

A comparison of "as designed" bridge with "as behaving" bridge was necessary to understand what might have gone wrong in design that led to the bridge cracking at the various locations.

A. The Loadings according to ASTHO 1978

Highway loadings as shown in Figure 4.21 was used for live load. This will include using the CEB-MC 1978 model for creep and shrinkage, the thermal gradient used is a linear variation with 18-degree F at the top and zero at the bottom with dead load only, and 9-degree F at the top when live load is included, and live loads as HS 20-44(MS 18) as shown in Figure 4.21, Figure 4.22, and Figure 4.23, with impact based on the 1977 AASHTO specification as shown in Figure 4.22.

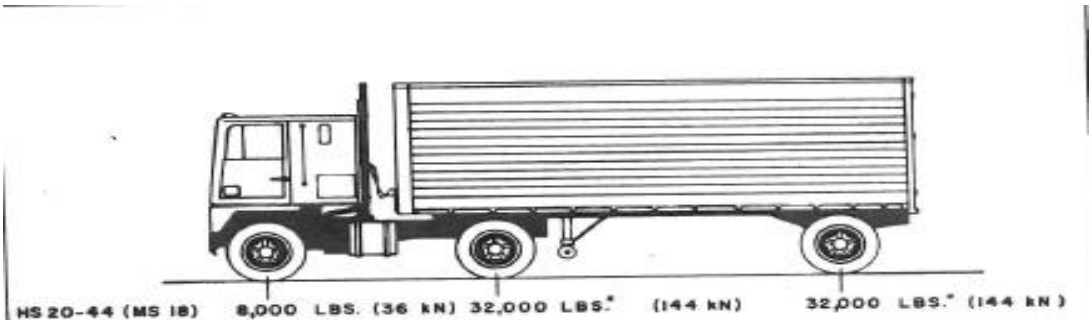

Fig 4.21. Standard HS (MS) Truck

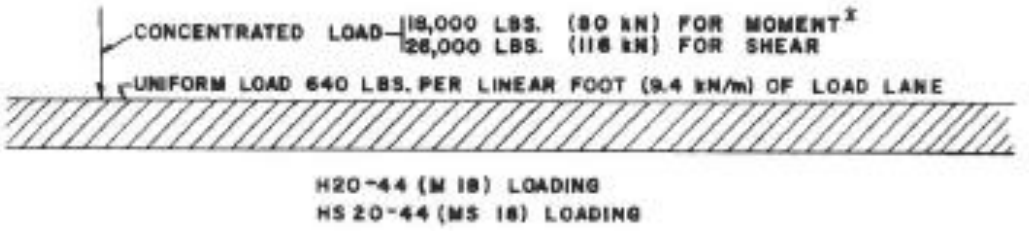

Fig 4.22. Loading Criterion

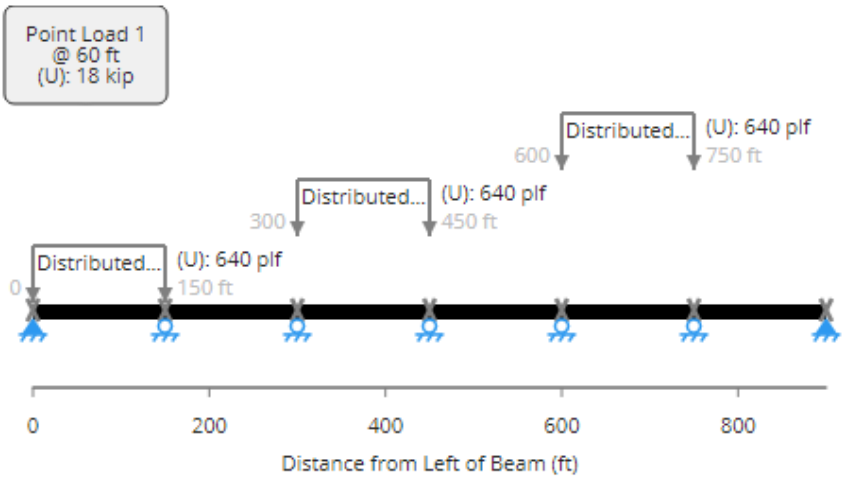

Fig 4.23. Live Load criterion for Span 1 (worst case moment)

4.3.1 "As Designed"

The bridge was designed according to CEB-MC 1978 model for creep and shrinkage, the thermal gradient used was a linear variation with 18-degree F at the top and zero at the bottom with dead load only, and 9-degree F at the top when live load is included. The two load combinations of interest were calculated. Both combinations included all permanent loads and prestress, while the first included live load plus half of the thermal gradient, the second included no live load, but full thermal gradient. The resulting bottom fiber stresses (most tensile) due to these loadings are presented in Figure 4.24. As can be seen in the Figure 4.24, there are no locations where the bottom fiber stress is in tension. The maximum tensile stress occurs with the half thermal gradient load case and is only 30psi. The maximum tensile stress allowed per the plan set was 0 psi. So, this analysis indicates that the allowable stress was not exceeded anywhere across the bridge. Therefore, based on the design assumptions at the time, the analysis indicates that the bottom slab should not have cracked.

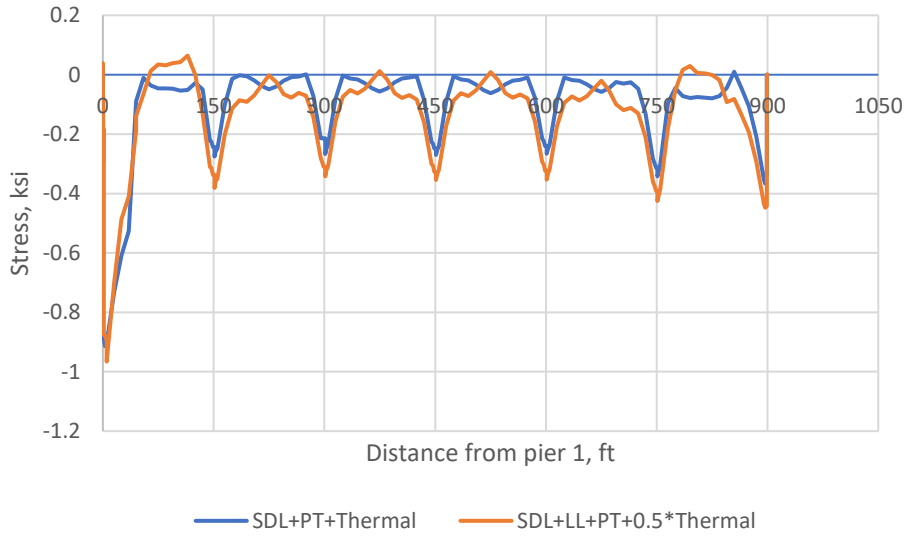

Figure 4.24: Bottom fiber stresses for two load combinations

4.3.2 "As Behaving"

The behavior of bridge aligns more closely with CEB-FIB 1990 model for creep and shrinkage, the thermal gradient used was a non-linear variation. Like previous section, the two load combinations of interest were calculated. Both combinations included all permanent loads and prestress, while the first included live load plus half of the thermal gradient, the second included no live load, but full thermal gradient. The resulting bottom fiber stresses (most tensile) due to these loadings are presented in Figure 4.25. As can be seen in the Figure 4.25, there are several locations where the bottom fiber stress is tensile. Highest tensile stress is 116 psi which is small but is larger than "as designed".

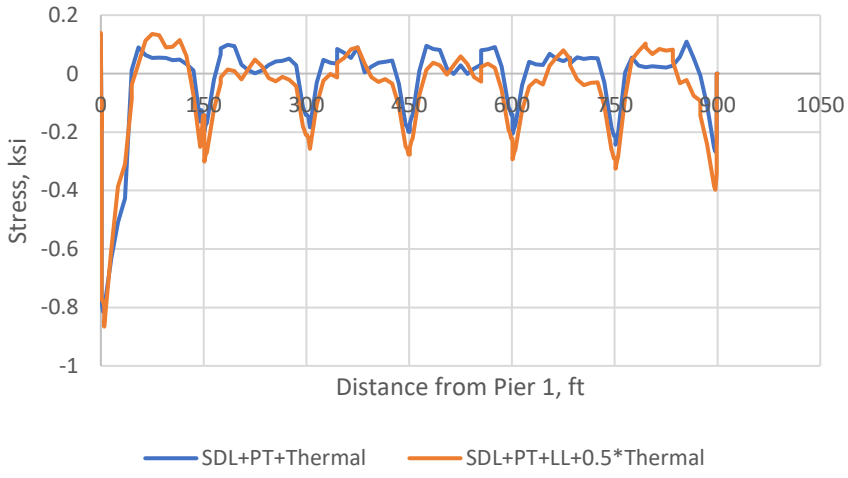

Figure 4.25: Bottom fiber stresses for two load combinations

4.3.3 Comparison of "as Designed" vs "as Behaving."

A comparison of "as designed" and "as behaving" is shown in this section. Figure 4.26 shows the comparison load case (DL+PT+Thermal). It can be seen that the "as behaving" bottom fiber of the bridge have higher tensile stresses when compared to "as designed". Similarly, a comparison of bottom fiber stresses is depicted for load case (DL+PT+0.5Thermal+LL) is shown in figure 4.26.

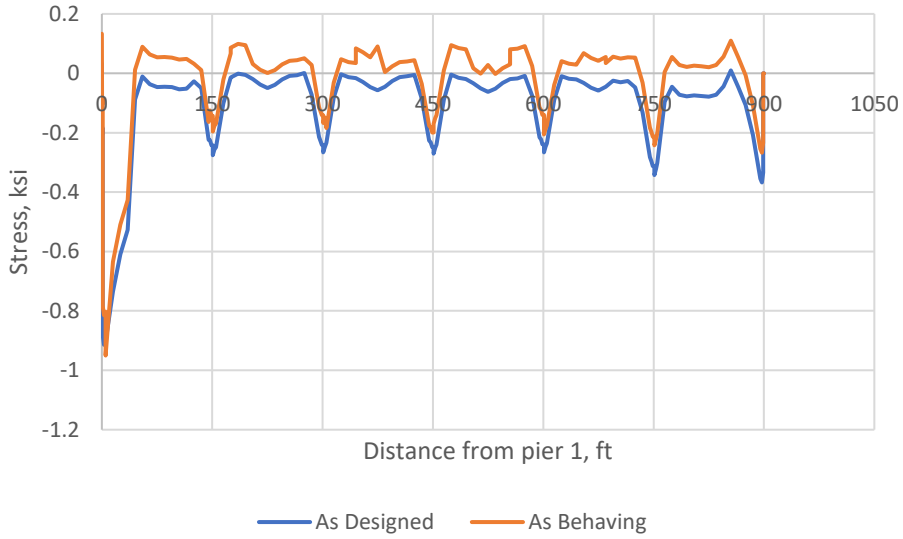

Figure 4.26: Comparison for of bottom fiber stress (DL+PT+Thermal)

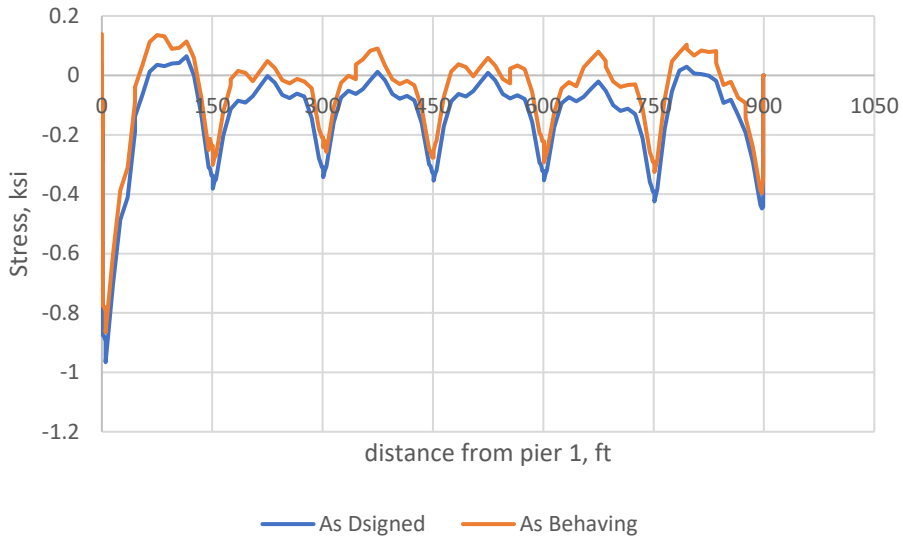

Figure 4.10: Comparison for of bottom fiber stress (DL+PT+0.5Thermal+LL)

4.4 Finite Element and Field Data Comparison

Table 4.10 provides the summary of results obtained from field data and finite element model using CEB-FIP ’90 code expressions. The table also shows the percentage difference between these values. Again, prestress losses were calculated by subtracting the effective prestress values at 12,000 days from the original jacking stresses.

Table 4.10: Finite Element and Field Data Comparison

		Prestress at 12,000 Days (ksi)	% Difference
Section C-C, Span 5	FE Model	165.4	3.08
	Field Data	160.3	
Section A-A, Span 6	FE Model	165.3	0.12
	Field Data	165.1	
Section D-D, Span 9	FE Model	165.0	0.85
	Field Data	163.6	
Section G-G, Span 11	FE Model	165.1	0.84
	Field Data	163.7	

Previous studies for bridge indicated the prestressing force for Span 6 to be 166 ksi in 2014 while as calculated and shown in Table 4.10 for 2020, the value for prestress force is 165.1 ksi. This means the prestress force reduced only 0.84% in the duration of 6 years.

Chapter 5 Summary, Conclusions, and Recommendations for Future Work

5.1 Summary

A flexural crack on the bottom flange of Span 6 of the Varina-Enon Bridge under heavy traffic loads was observed by the Virginia Department of Transportation in the summer 2012. This suggested unanticipated high-tension levels, which could be attributed to many factors, including prestress losses that were greater than expected. This thesis aimed to investigate the longitudinal flexural behavior of the Varina-Enon Bridge by estimating the effective prestress forces at the locations of interest in Spans 5, 6, 9, and 11. Field data from instrumentation in Spans 5, 6, 9, and 11 was used to calculate the effective prestress forces based on the assumption that the total stress when the cracks opened was equal to zero. By performing time-dependent analysis, the FE model was used to validate the field-data performance using CEB-FIP '90 code expressions for creep and shrinkage. The results from the FE model were compared with results from field data which helped in validation of method used to calculate the effective prestress from field data. It also ensured if the prestress losses were in range of expected losses.

Refinement of results was done using a threshold of crack opening to eradicate the noise as lot of scatter was observed for small crack openings. The threshold crack openings for span 5, 6, 9, and 11 were 0.004 in., 0.002 in., 0.0005 in., and 0.0004 in., respectively. The mean value of effective prestress force at the locations of interests in span 5, 6, 9, and 11 were 160.3 ksi, 165.1 ksi, 163.6 ksi and 163.7 ksi. while the corresponding values predicted by the FE model were 165.4 ksi, 165.3 ksi, 165.0 ksi, and 165.1 ksi. There are discrepancies between as designed and as behaving bridge and the later shows higher tensile stresses at the bottom fiber of bridge (most tensile).

5.2 Conclusions

5.2.1 Expected vs measured losses.

Effective prestress estimates from raw field data, including events for all crack openings, show substantially greater prestress losses than the FE model expected. Removal of small crack openings results in reduction of discrepancies between the FE model and raw field data estimates to a great extent. The model overestimates the effective prestress in 2019 by 3.08% at the crack in Span 5, 0.12% at the crack in Span 6, 0.84% at the crack in Span 9, and 0.85% at the crack in Span 11. These differences are considered to be within a reasonable margin of error, indicating good agreement between the finite element model using the CEB MC 90-99 model and field data results. Consequently, it is safe to conclude that method

used to calculate effective prestress forces from the field data is correct and the bridge under study does not experience greater than expected losses.

5.2.2 Bridge performance

The precise prediction of prestress losses is one main feature of the structural assessment of prestressed bridges as it can affect the serviceability and performance of bridge. The Varina-Enon bridge has unbonded post-tensioned tendons and excessive loss of prestress can cause increased deflections and reduction in flexural strength. Earlier studies on Varina-Enon showed that prestress values from field data and FE model aligned more closely when using CEB-FIP ’90 code expressions for long term losses (Lindley 2019) while the bridge was designed according to CEB-FIP ’78 code. This suggests inconsistency while considering the “as designed” bridge. The “as designed” bridge was not expected to crack the analysis of “as behaving” bridge does not explain the reasons of cracking.

Excessive cracking could be one serviceability concern as it can lead to admittance of water which in turn can deteriorate the steel tendons. But since all the crack location are in bottom flanges of the box girder of bridge and the prestressing tendons are grouted in PVC ducts, it is of less concern.

Predictions about the progression of losses in prestress Varina-Enon Bridge can be made by comparing results from 2019 and 2020 data with 2013 and 2014 data. Previous studies for bridge indicated the prestressing force for Span 6 to be 166 ksi in 2014 while as calculated for 2020 the value for prestress force is 165.1 ksi. This means the prestress force reduced only 0.84% in this duration of 6 years which aligns with the assumption of prestress loss reaching asymptotic value after long durations.

5.3 Recommendations for Future Work

The research conducted till now for Varina-Enon bridge scrutinized the prestress losses in Spans 5, 6, 9, and 11. It also studied the defections and shear crack openings in Span 14. The following recommendations are made followed to investigate the performance and conditions of the bridge:

1. The monitoring of prestress losses in Spans 5 and 6 should be continued to study the progression of prestress losses at these locations. As the literature indicates underprediction of long-term losses by CEB-FIP, this progression should be compared with the current models like Bazant’s.
2. The mobile data acquisition system installed in Span 11 should be moved to other crack location throughout the bridge to inspect the prestressing at those crack locations.
3. To evaluate how the progression of prestress losses impacts the potential load rating of the Varina-Enon Bridge, a more detailed analysis should be performed.

4. A more detailed analysis should be performed to evaluate how the progression of prestress losses impacts the potential load rating of the Varina-Enon Bridge,

BIBLIOGRAPHY

ACI 209. (2008). *Guide for Modeling and Calculating Shrinkage and Creep in Hardened Concrete*. American Concrete Institute, Farmington Hills, MI.

ACI 423. (2016). *Guide to Estimating Prestress Loss*. American Concrete Institute.

Bažant, Z. P., and Jirásek, M. (2018). *Creep and Hygrothermal Effects in Concrete Structures*. *Solid Mechanics and its Applications*, Springer Science+Business Media B.V., Dordrecht, The Netherlands.

Duemmel, P. S., Baber, T. T., Barton, F. W., and McKeel, Wallace T., J. (1992). *Field Instrumentation and Measured Response ofthe 1-295 Cable-Stayed Bridge: Part I - Field Study of Live Load Responses*. Richmond, VA

Brodsky, R. A. (2020). *Effective Prestress Evaluation of the Varina-Enon Bridge Using a Long-Term Monitoring System and Finite Element Model* (Doctoral dissertation, Virginia Tech).

F&M Engineers, I. (1993). *Owner's Manual for Inspection and Maintenance of Segmental Concrete Approaches and Main Span*.

Helmicki, A. J., Hunt, V. J., and Nims, D. K. (2012). *Instrumentation of the Maumee River Crossing*. Cincinnati, OH.

Larsa 4D. (2019). "Larsa 4D Reference Manual."

Lindley, S. M. (2019). "Investigation of the Time-Dependent Longitudinal Flexural Behavior of the Varina-Enon Bridge." Virginia Tech.

Lissenden, C. J. I. (1988). "Dynamic Modeling of a Cable-Stayed Bridge During Construction." University of Virginia.

Maguire, M., Moen, C. D., Roberts-Wollmann, C., and Cousins, T. (2015). "Field verification of simplified analysis procedures for segmental concrete bridges." *Journal of Structural Engineering (United States)*, 141(1), 1–11.

Maguire, M., Roberts-Wollmann, C. L., and Cousins, T. (2014). *Live Load Test and Long Term Monitoring of the Varina-Enon Bridge*. Blacksburg, VA.

Nimse, P. S., Nims, D. K., Hunt, V. J., and Helmicki, A. J. (2015). "Use of Construction Stages to Review a Bridge Finite-Element Model." *Journal of Bridge Engineering*, 20(8), 1–14.

Shahawy, M. A., and Arockiasamy, M. (1996a). "Field instrumentation to study the time-dependent behavior in sunshine skyway bridge. I." *Journal of Bridge Engineering*, 1(2), 76–86.

Shahawy, M. A., and Arockiasamy, M. (1996b). "Analytical and measured strains in sunshine skyway bridge. II." *Journal of Bridge Engineering*, 1(2), 87–97.

Xu, X., Huang, Q., Ren, Y., Zhao, D. Y., Yang, J., and Zhang, D. Y. (2019). "Modeling and Separation of

Thermal Effects from Cable-Stayed Bridge Response.” *Journal of Bridge Engineering*, 24(5), 1–16.

Appendix A. Original Drawings of Tendon Profiles

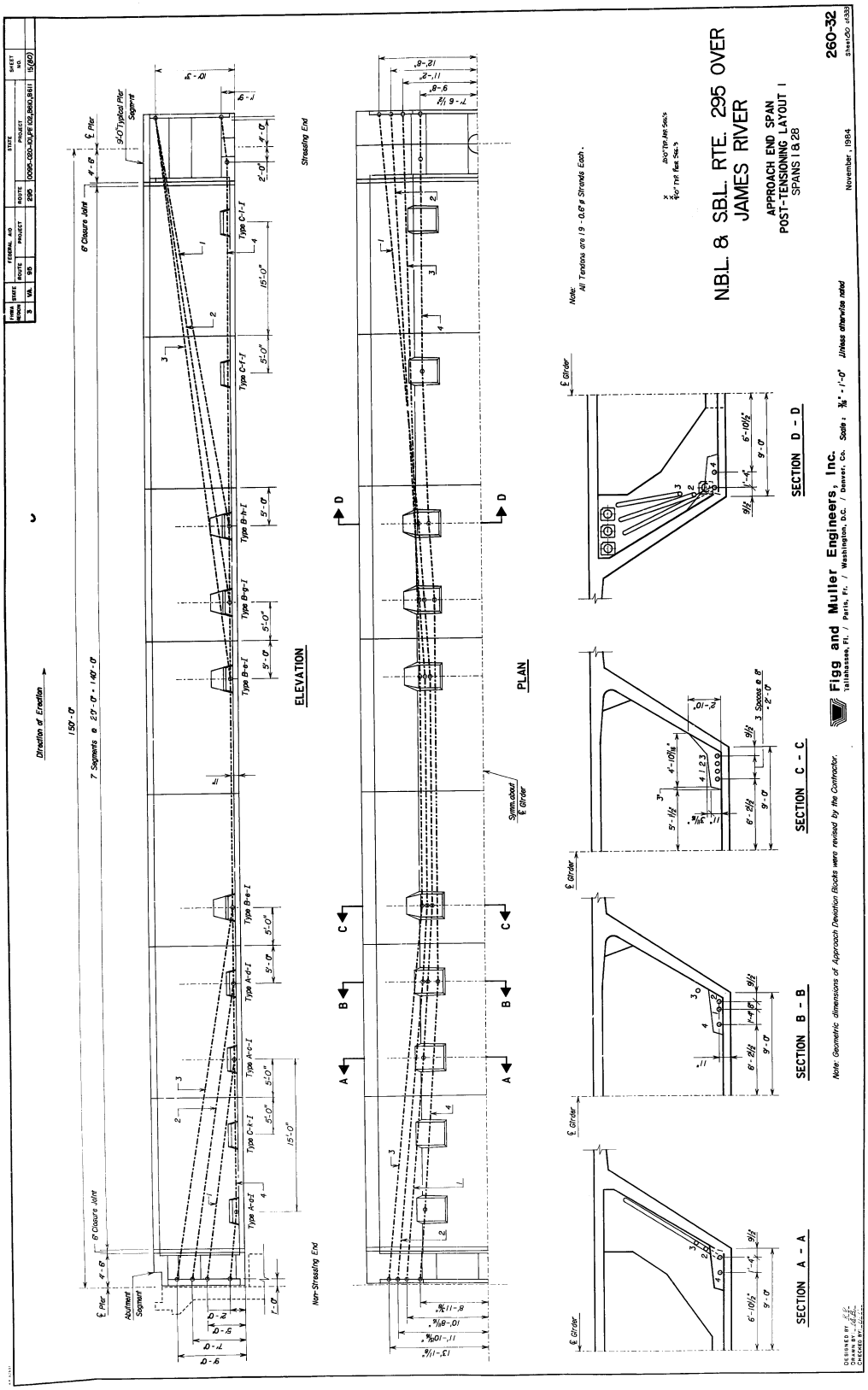

FHWA REGION	STATE	FEDERAL AID ROUTE	FEDERAL AID PROJECT	STATE ROUTE	STATE PROJECT	SHEET NO.
3	VA.	95		295	0095-020-101,PE 102,B610,B611	15(81)

Direction of Fraction →

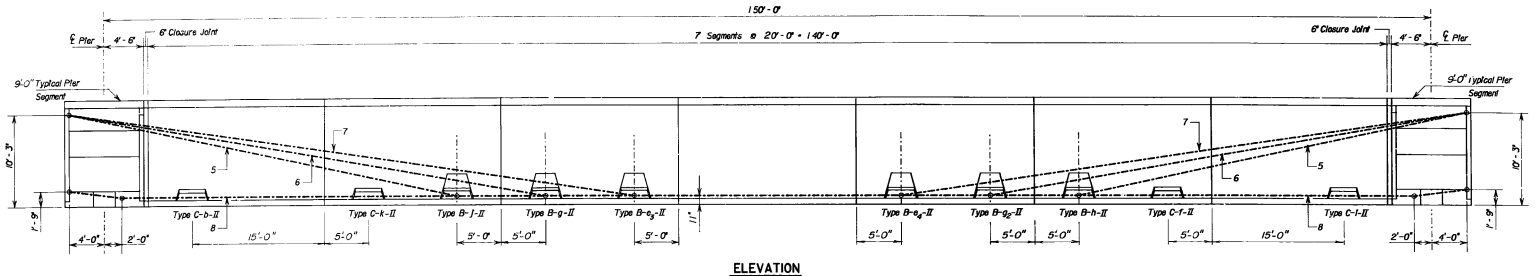

ELEVATION

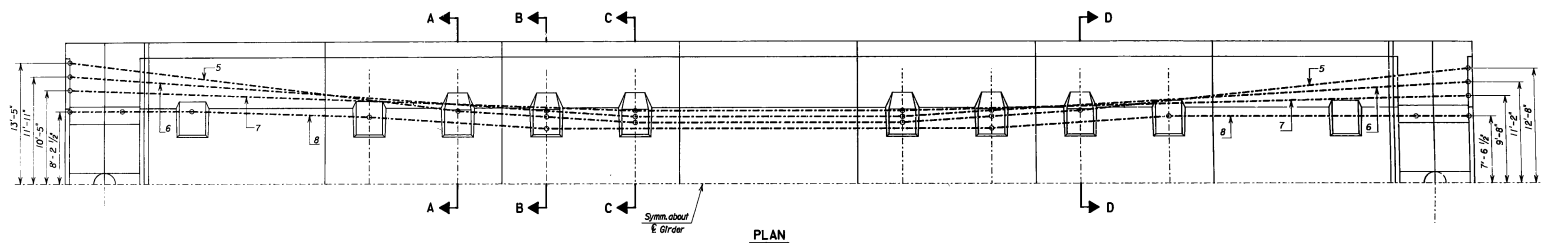

PLAN

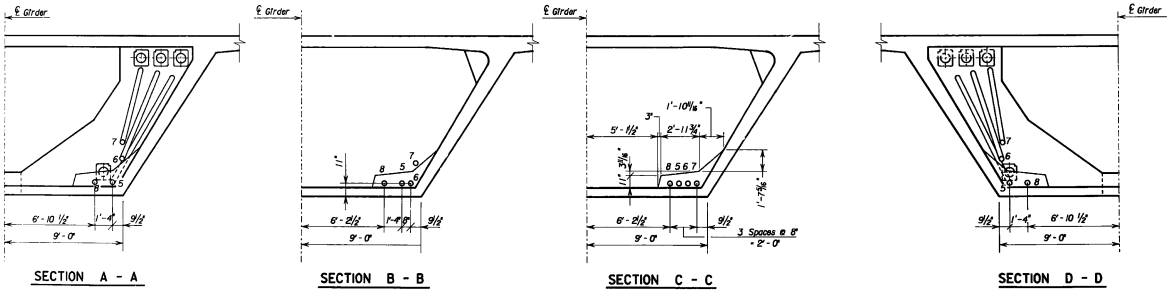

SECTION A - A | SECTION B - B | SECTION C - C | SECTION D - D

Note:
All Tendons are 13 - 0.6" ϕ Strands Each.

20'-0" Typ. Apt. Sec.'s
9'-0" Typ. Post Sec.'s

N.B.L. & S.B.L. RTE. 295 OVER JAMES RIVER

APPROACH TYPICAL SPAN
POST-TENSIONING LAYOUT II
SPANS 2-5, 8-11, 21-23, 26 AND 27

Note: Geometric dimensions of Approach Deviation Blocks were revised by the Contractor.

DESIGNED BY
DRAWN BY
CHECKED BY

Figg and Muller Engineers, Inc.
Tallahassee, Fl. / Paris, Fr. / Washington, D.C. / Denver, Co.

Scale : 3/16" = 1'-0" Unless otherwise noted

November, 1984

260-32
Sheet 67 of 333

FHWA REGION	STATE	FEDERAL AID ROUTE	FEDERAL AID PROJECT	STATE ROUTE	STATE PROJECT	SHEET NO.
3	VA.	95		295	0096-020-101,PE 102,B610,B611	15(82)

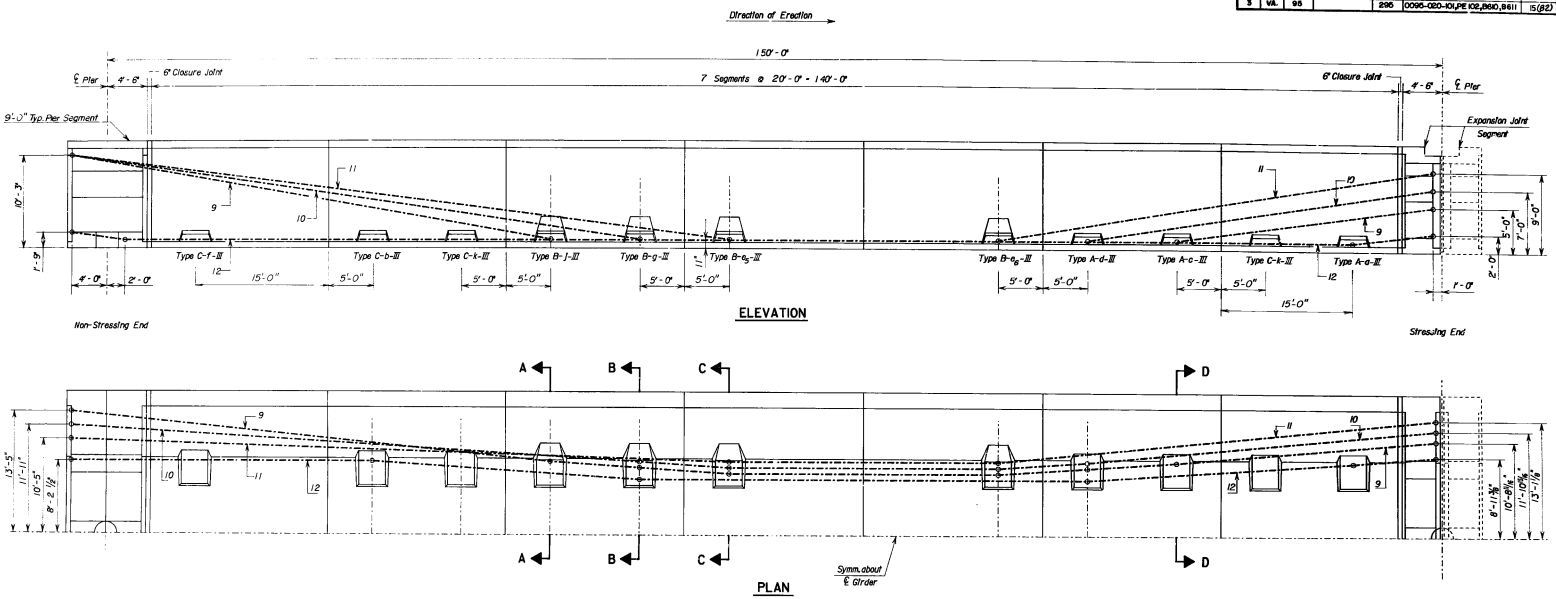

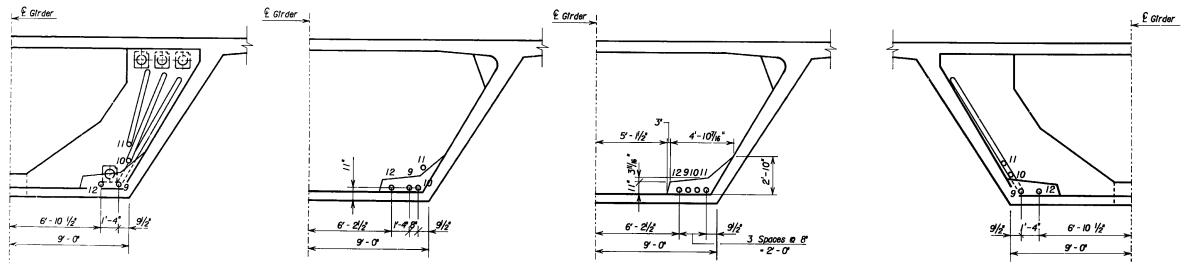

Note:
All Tendons are 19 - 0.6"ø Strands Each.

10'0" TYP. EXP. SEG.'S
9'0" TYP. PIER SEG.'S

N.B.L. & S.B.L. RTE. 295 OVER JAMES RIVER

APPROACH EXPANSION JOINT SPAN POST-TENSIONING LAYOUT III SPANS 6, 12, 20 & 25

DESIGNED BY
DRAWN BY
CHECKED BY

Note: Geometric dimensions of Approach Deviation Blocks were revised by the Contractor.

Figg and Muller Engineers, Inc.
Tallahassee, Fl. / Paris, Fr. / Washington, D.C. / Denver, Co.

Scale : 3/16" = 1'-0" Unless otherwise noted

November, 1984

260-32

Sheet 92 of 333

FHWA REGION	STATE	FEDERAL AID ROUTE	FEDERAL AID PROJECT	STATE ROUTE	STATE PROJECT	SHEET NO.
3	VA.	95		295	0095-020-101,PE 102,R910,B611	15(97)

LONGITUDINAL POST TENSIONING QUANTITIES APPROACH SUPERSTRUCTURE

Span No.	Tendon No.	Tendon Type	Tendon Length (ft)	Tendon Weight (lbs)	Number of Tendons / Girder	Total Weight (lbs)	Stressing Force (kips)
1,28	1	19-0.6" ϕ	153.99	2165	4	8,660	861
	2	19-0.6" ϕ	153.96	2164	4	8,658	865
	3	19-0.6" ϕ	154.03	2165	4	8,662	871
	4	19-0.6" ϕ	152.78	2148	4	8,592	861
2,3,4,5, 8,9,10,11, 21,22,23, 26,27,	5	19-0.6" ϕ	159.74	2245	26	58,370	879
	6	19-0.6" ϕ	159.03	2236	26	58,136	871
	7	19-0.6" ϕ	158.58	2229	26	57,954	865
	8	19-0.6" ϕ	157.30	2211	26	57,486	854
6,12 20,25,	9	19-0.6" ϕ	153.99	2165	8	17,320	889
	10	19-0.6" ϕ	153.96	2164	8	17,317	883
	11	19-0.6" ϕ	154.03	2165	8	17,325	874
	12	19-0.6" ϕ	152.78	2148	8	17,184	868
7,24	13	19-0.6" ϕ	153.99	2165	4	8,660	861
	14	19-0.6" ϕ	153.96	2164	4	8,656	865
	15	19-0.6" ϕ	154.03	2165	4	8,660	871
	16	19-0.6" ϕ	152.78	2148	4	8,592	861

TOTAL WEIGHT BOTH GIRDERS = 740,464 Lbs.

POST TENSIONING QUANTITIES APPROACH SUPERSTRUCTURE

Pier	Bar Size	Length	Weight (Lbs.)	Number of Anchorages	Number of Bars	Total Weight (Lbs.)	Stressing Force (kips)
8	1⅜" ϕ	11.90	66	32	16	1058	166k
9	↑	↑	↑	↑	↑	↑	↑
10	↓	↓	↓	↓	↓	↓	↓
11	↓	↓	↓	↓	↓	↓	↓
12	1⅜" ϕ	11.90	66	32	16	1058	166k
Totals	——	——	——	160	80	5291	——

Note: Totals shown are for One Girder only.

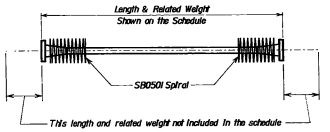

Note : All mild steel reinforcement for Post-tensioning shall be Incidental to the system.

VERTICAL POST TENSIONING QUANTITIES APPROACH SUPERSTRUCTURE

Segment	Tendon No.	Number of Segs./ Girder	Tendon Type	Tendon Length (ft)	Tendon Weight (lbs)	Total Weight (lbs)	Stressing Force (kips)
Typical * Pier	A	34	4 x 0.6" ϕ	28.05	83	2823	185k
	B	34	4 x 0.6" ϕ	26.79	79	2696	↑
	C	34	4 x 0.6" ϕ	26.14	77	2630	
	D	34	4 x 0.6" ϕ	25.50	75	2566	
	A'	34	4 x 0.6" ϕ	28.07	83	2824	
	B'	34	4 x 0.6" ϕ	26.80	79	2696	
	C'	34	4 x 0.6" ϕ	26.14	77	2630	
	D'	34	4 x 0.6" ϕ	25.49	75	2565	
Exp.Jt. Pier	A	6	4 x 0.6" ϕ	28.47	84	505	
	B	6	4 x 0.6" ϕ	26.13	77	464	
	C	6	4 x 0.6" ϕ	26.55	79	474	
	D	6	4 x 0.6" ϕ	26.54	79	474	
	A'	6	4 x 0.6" ϕ	28.46	84	505	
	B'	6	4 x 0.6" ϕ	26.12	77	463	
	C'	6	4 x 0.6" ϕ	26.56	79	474	
	D'	6	4 x 0.6" ϕ	26.53	79	474	
Abut.	A	2	4 x 0.6" ϕ	28.47	84	168	
	B	2	4 x 0.6" ϕ	26.13	77	154	
	C	2	4 x 0.6" ϕ	26.55	79	158	
	D	2	4 x 0.6" ϕ	26.54	79	158	
	A'	2	4 x 0.6" ϕ	28.46	84	168	
	B'	2	4 x 0.6" ϕ	26.12	77	154	
	C'	2	4 x 0.6" ϕ	26.56	79	158	
	D'	2	4 x 0.6" ϕ	26.53	79	158	185k

TOTAL WEIGHT BOTH GIRDERS = 53,078 Lbs.

* 9'-0" Segments
See ✱

N.B.L. & S.B.L. RTE. 295 OVER JAMES RIVER

SUPERSTRUCTURE POST-TENSIONING QUANTITIES AND STRESSING SCHEDULE

DESIGNED BY
DRAWN BY
CHECKED BY

Figg and Muller Engineers, Inc.
Tallahassee, Fl. / Paris, Fr. / Washington, D.C. / Denver, Co.

Scale : N / A Unless otherwise noted

November, 1984

260-32
Sheet 97 of 333

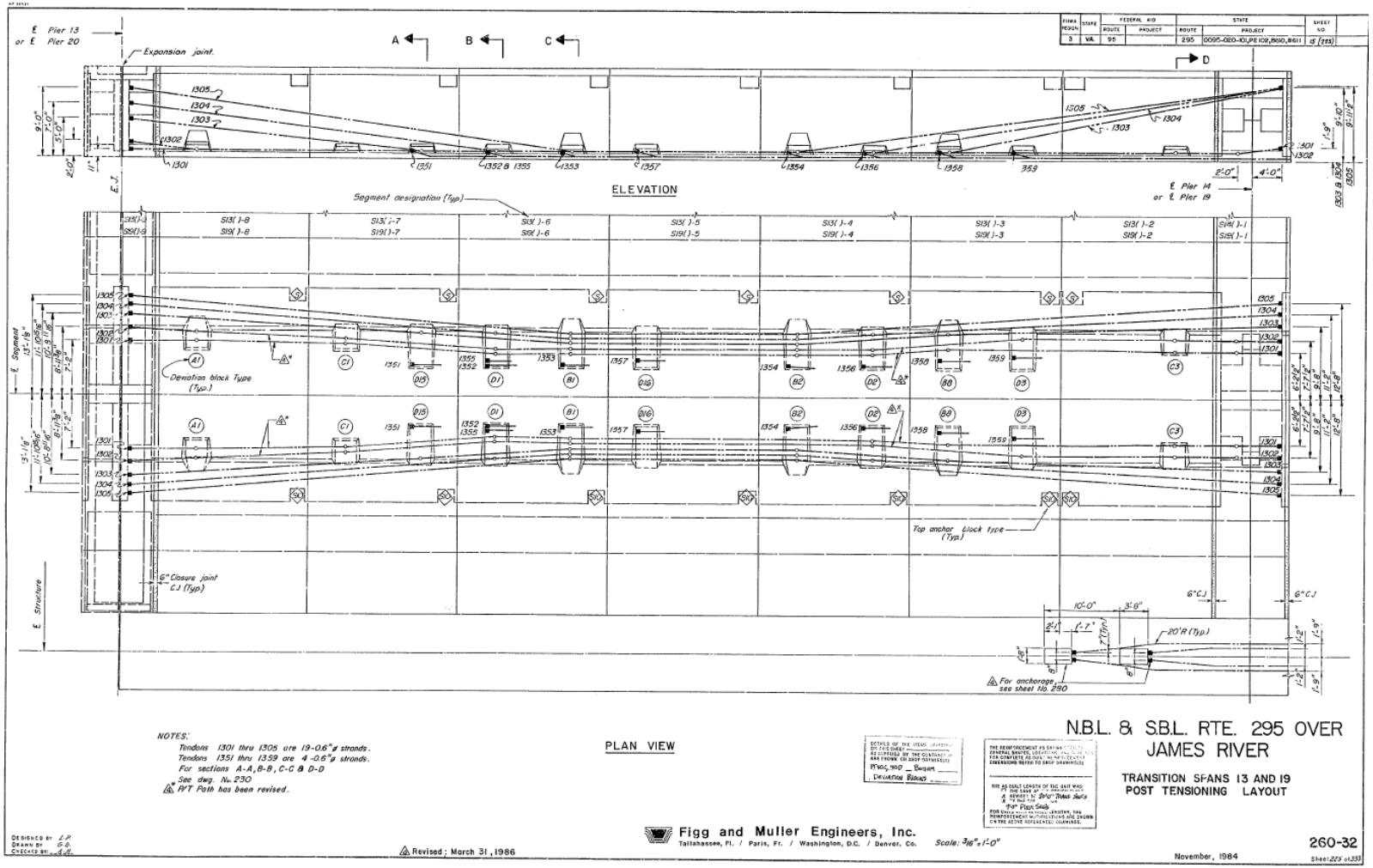

NOTES:
Tendons 1301 thru 1305 are 19-0.6"ϕ strands.
Tendons 1351 thru 1359 are 4-0.6"ϕ strands.
For sections A-A, B-B, C-C & D-D
See dwg. No. 230
Δ* P/T Path has been revised.

N.B.L. & S.B.L. RTE. 295 OVER JAMES RIVER

TRANSITION SPANS 13 AND 19 POST TENSIONING LAYOUT

FHWA REGION	STATE	FEDERAL AID ROUTE	FEDERAL AID PROJECT	STATE ROUTE	STATE PROJECT	SHEET NO
3	VA.	95		295	0095-020-101,PE 102,B660,B611	15 (225)

Figg and Muller Engineers, Inc.
Tallahassee, Fl. / Paris, Fr. / Washington, D.C. / Denver, Co.

Scale: 3/16"=1'-0"

Δ Revised; March 31, 1986

November, 1984

260-32

Sheet 225 of 333

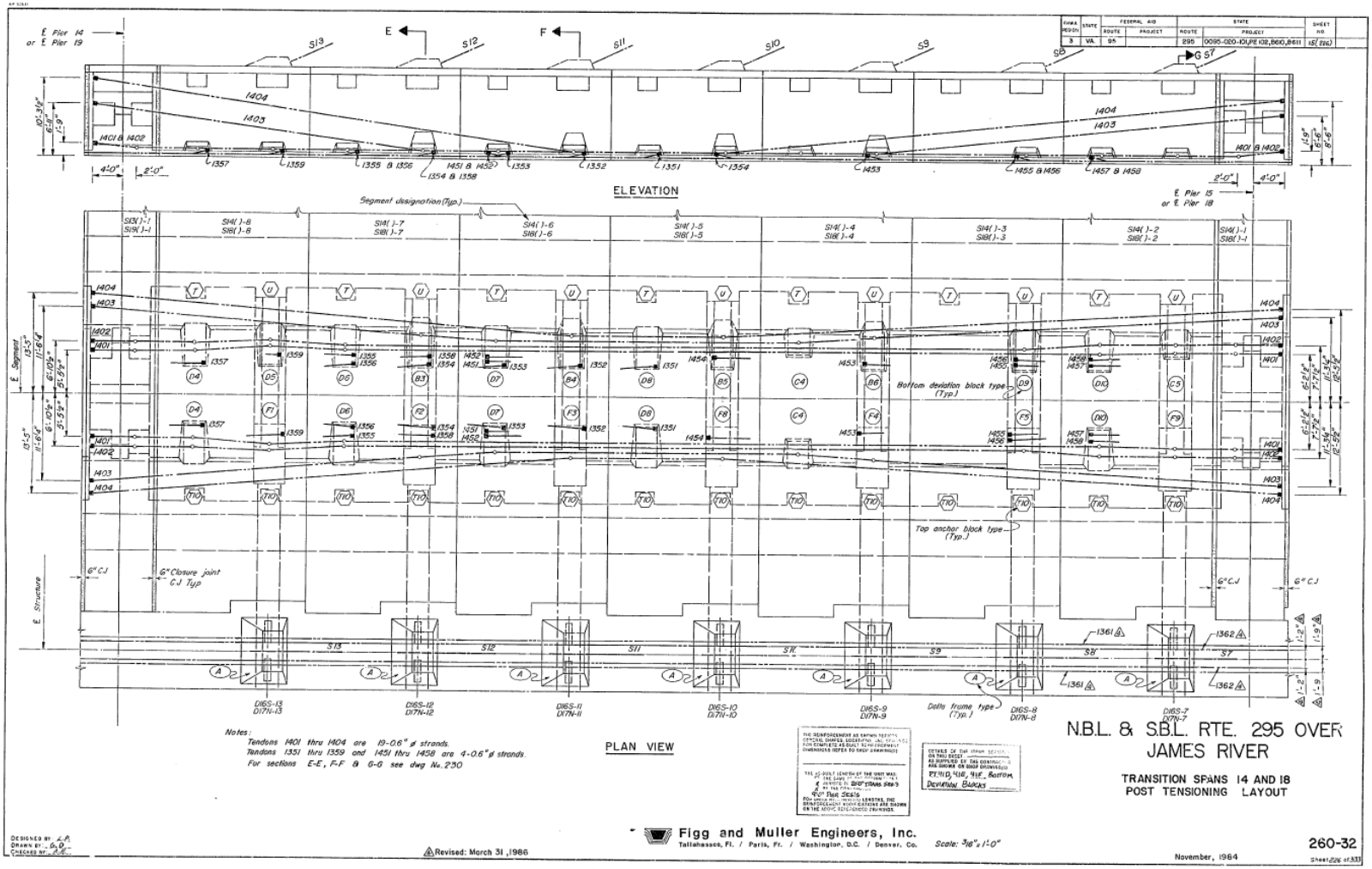
ELEVATION
PLAN VIEW
E Pier 14 or E Pier 19
E Pier 15 or E Pier 18
Segment designation (Typ.)
Bottom deviation block type (Typ.)
Top anchor block type (Typ.)
Dills frame type (Typ.)
Deviation Blocks
6" C.J
6" Closure joint C.J Typ
E Segment
E Structure
Notes:
Tendons 1401 thru 1404 are 19-0.6" ø strands.
Tendons 1351 thru 1359 and 1451 thru 1458 are 4-0.6" ø strands.
For sections E-E, F-F & G-G see dwg No. 230
N.B.L. & S.B.L. RTE. 295 OVER JAMES RIVER
TRANSITION SPANS 14 AND 18
POST TENSIONING LAYOUT
Figg and Muller Engineers, Inc.
Tallahassee, Fl. / Paris, Fr. / Washington, D.C. / Denver, Co.
Scale: 3/16"=1'-0"
November, 1964
260-32
Revised: March 31, 1986

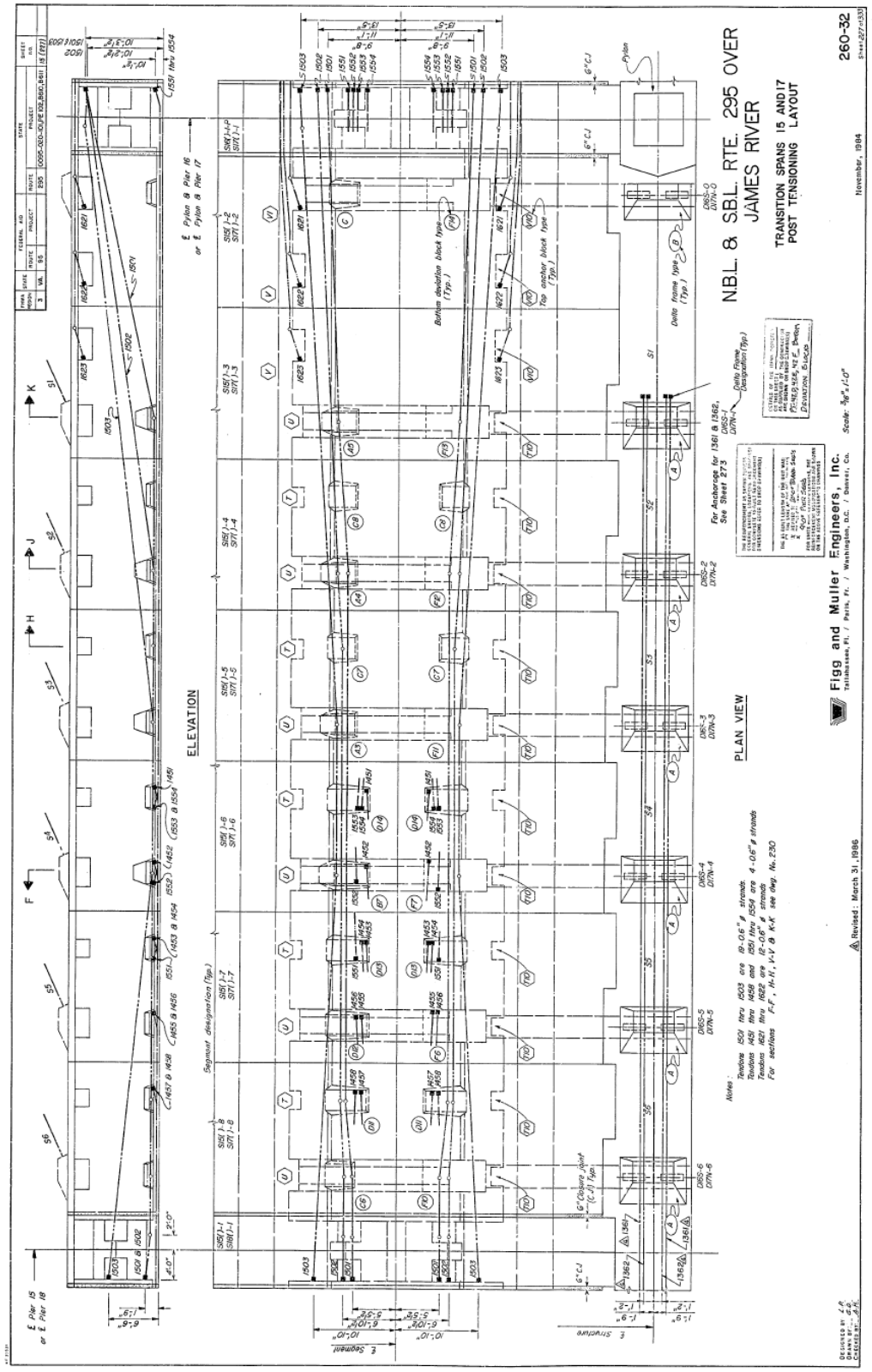
N.B.L. & S.B.L. RTE. 295 OVER JAMES RIVER
TRANSITION SPANS 15 AND 17
POST TENSIONING LAYOUT
260-32
ELEVATION
PLAN VIEW
Figg and Muller Engineers, Inc.
Tallahassee, Fl. / Perth, Ft. / Washington, D.C. / Denver, Co.
Revised: March 31, 1986
November, 1984

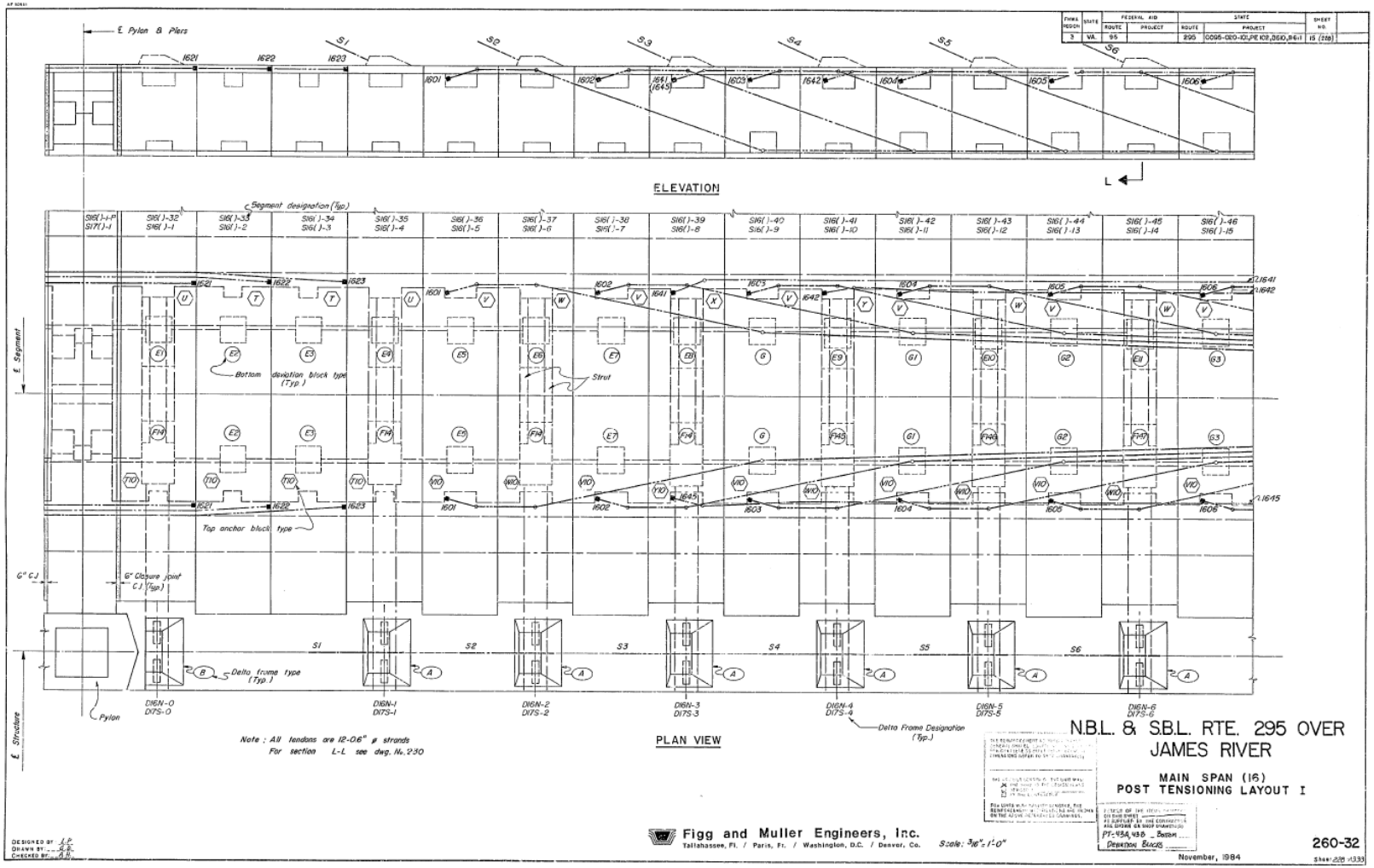
E Pylon & Piers
S1
S2
S3
S4
S5
S6
1621
1622
1623
1601
1602
1641 (1645)
1603
1642
1604
1605
1606
ELEVATION
Segment designation (Typ.)
S16( )-P S17( )-1
S16( )-32 S16( )-1
S16( )-33 S16( )-2
S16( )-34 S16( )-3
S16( )-35 S16( )-4
S16( )-36 S16( )-5
S16( )-37 S16( )-6
S16( )-38 S16( )-7
S16( )-39 S16( )-8
S16( )-40 S16( )-9
S16( )-41 S16( )-10
S16( )-42 S16( )-11
S16( )-43 S16( )-12
S16( )-44 S16( )-13
S16( )-45 S16( )-14
S16( )-46 S16( )-15
E Segment
Bottom deviation block type (Typ.)
Strut
Top anchor block type
6" C.J.
6" Closure joint C.J. (Typ.)
Delta frame type (Typ.)
Pylon
E Structure
DIGN-0 DI7S-0
DIGN-1 DI7S-1
DIGN-2 DI7S-2
DIGN-3 DI7S-3
DIGN-4 DI7S-4
DIGN-5 DI7S-5
DIGN-6 DI7S-6
Delta Frame Designation (Typ.)
Note : All tendons are 12-0.6" ø strands
For section L-L see dwg. No. 230
PLAN VIEW
FIRM REGION 3
STATE VA.
FEDERAL AID ROUTE 95
FEDERAL AID PROJECT
STATE ROUTE 295
STATE PROJECT 0095-020-101,PE 102,B610,B611
SHEET NO. 15 (228)
N.B.L. & S.B.L. RTE. 295 OVER JAMES RIVER
MAIN SPAN (16)
POST TENSIONING LAYOUT I
PT-45A,45B - Bottom
Deviation Blocks
Figg and Muller Engineers, Inc.
Tallahassee, Fl. / Paris, Ft. / Washington, D.C. / Denver, Co.
Scale: 3/16"=1'-0"
November, 1984
260-32
Sheet 226 of 333
DESIGNED BY J.P.
DRAWN BY A.B.
CHECKED BY A.B.

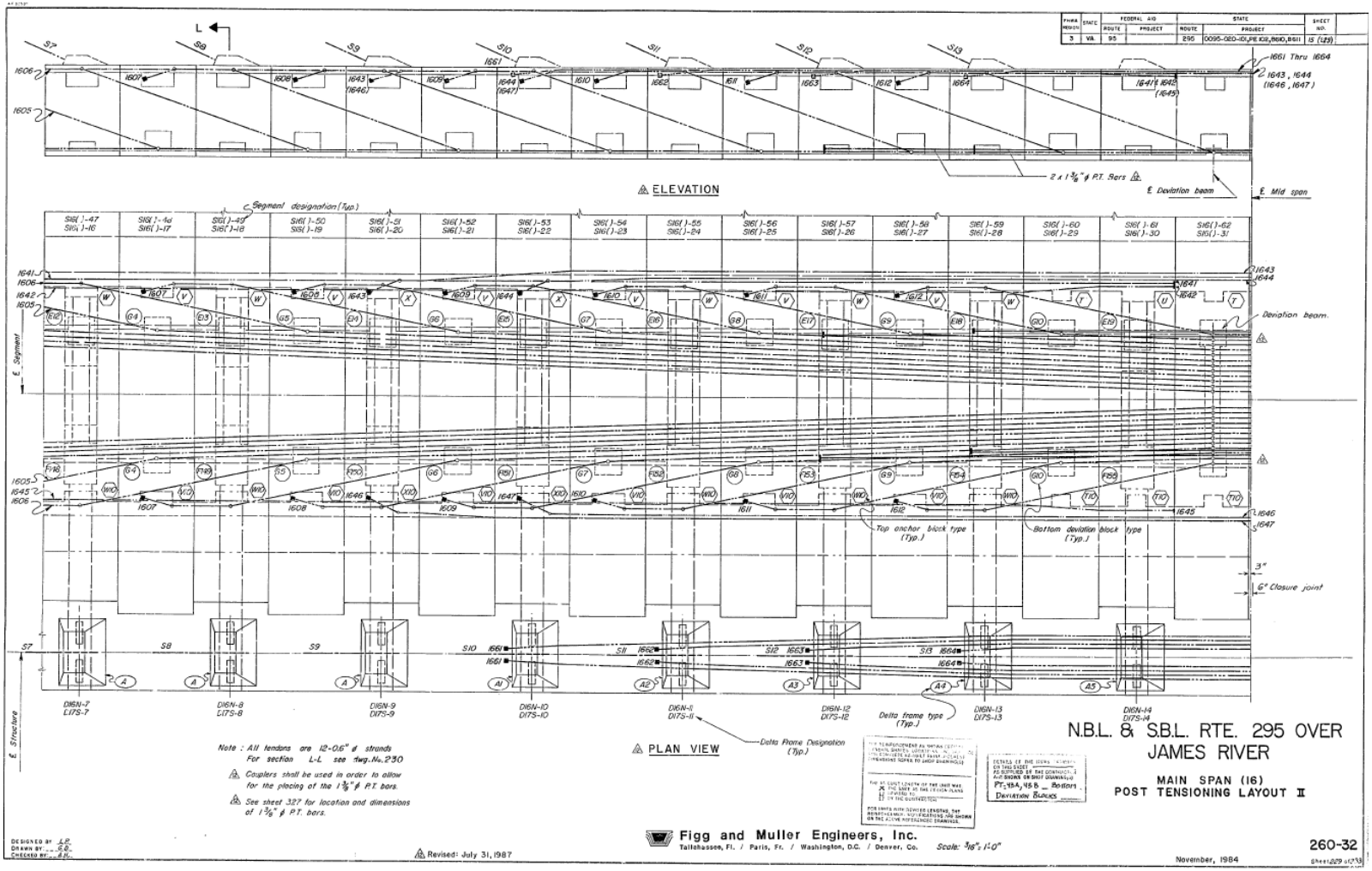
ELEVATION
PLAN VIEW
Segment designation (Typ.)
2 x 1 3/8" ϕ P.T. Bars
E Deviation beam
E Mid span
Deviation beam
Top anchor block type (Typ.)
Bottom deviation block type (Typ.)
3"
6" Closure joint
Delta frame type (Typ.)
Delta Frame Designation (Typ.)
E Segment
E Structure
DIGN-7 LITS-7
DIGN-8 LITS-8
DIGN-9 DITS-9
DIGN-10 DITS-10
DIGN-11 DITS-11
DIGN-12 DITS-12
DIGN-13 LITS-13
DIGN-14 DITS-14
Note : All tendons are 12-0.6" ϕ strands For section L-L see Awg. No. 230
Couplers shall be used in order to allow for the placing of the 1 3/8" ϕ P.T. bars.
See sheet 327 for location and dimensions of 1 3/8" ϕ P.T. bars.
PT-19A, 45B - Bottom Deviation Blocks
N.B.L. & S.B.L. RTE. 295 OVER JAMES RIVER
MAIN SPAN (16)
POST TENSIONING LAYOUT II
Figg and Muller Engineers, Inc.
Tallahassee, Fl. / Paris, Fr. / Washington, D.C. / Denver, Co.
Scale: 3/16"=1'-0"
November, 1984
260-32
Revised: July 31, 1987

FHWA REGION	STATE	FEDERAL AID ROUTE	FEDERAL AID PROJECT	STATE ROUTE	STATE PROJECT	SHEET NO.
3	VA.	95		295	0095-000-101,PE 102,B610,B611	15 (274)

TENDON SCHEDULE

Location	Tendon No.	Tendon Size	Tendon Length (Ft.)	Tendon Weight (Lbs)	Number of Tendon per Location	Number of Location	Total Weight (Lbs.)	Stressing Force (Kips)		Bars/Tendon SB0304	SB0501	SB0502	DB0501
Spans 13,19 (One girder)	1301	19-0.6"ϕ	153.23	2,154.4	2	4	17,235	844			2		
	1302		153.31	2,155.5			17,244						
	1303		154.28	2,169.2			17,354						
	1304		154.35	2,170.0			17,360						
	1305		154.51	2,172.4			17,379						
Spans 14,18 (One girder)	1401		158.19	2,224.6			17,794						
	1402		158.19	2,224.9			17,794						
	1403		158.97	2,235.1			17,881						
	1404		159.42	2,241.4			17,931						
Spans 15,17 (One girder)	1501		159.17	2,237.9			17,903						
	1502		158.83	2,233.1			17,865						
	1503	19-0.6"ϕ	159.05	2,236.2			17,890	844			2		
Spans 13 & 14 or 19 & 18 (One girder)	1351	4-0.6"ϕ	184.0	544.6			4,357	178		2			
	1352		164.0	485.4			3,883						
	1353		144.0	426.2			3,410						
	1354		104.0	307.8			2,462						
	1355		134.0	396.6			3,173						
	1356		84.0	248.6			1,989						
	1357		94.0	278.2			2,226						
	1358		84.0	248.6			1,989						
	1359		54.0	159.8			1,278						
Spans 14 & 15 or 18 & 17 (One girder)	1451		164.0	485.4			3,883						
	1452		154.0	455.8			3,646						
	1453		94.0	278.2			2,226						
	1454		114.0	337.4			2,699						
	1455		64.0	189.4			1,515						
	1456		64.0	189.4			1,515						
	1457		44.0	130.2			1,042						
	1458		44.0	130.2			1,042						
Span 15 (One girder)	1551		116.5	344.8			2,758						
	1552		106.5	315.2			2,522						
	1553		96.5	285.6			2,285						
	1554	4-0.6"ϕ	96.5	285.6			2,285	178		2			
Spans 15 & 16 or 17 & 16 (One girder)	1601	12-0.6"ϕ	67.75	246.4			1,971	533				2	
	1602		67.75	494.0			3,392	533					
	1623		67.75	601.6		4	4,813	533					
	1601		541.0	4,804.1		2	19,216	562					
	1602		501.0	4,448.9			17,796						
	1603		461.0	4,093.7			16,375						
	1604		421.0	3,738.5			14,954						
	1605		381.0	3,383.3			13,533						
	1606		341.0	3,028.1			12,112						
	1607		301.0	2,672.9			10,692						
	1608		260.8	2,315.9			9,264						
	1609		220.8	1,960.7			7,843						
	1610		180.8	1,605.5			6,422						
	1611		140.6	1,250.3			5,001						
	1612		100.6	895.1	9	2	3,580	562					
	1641		257.75	2,022.4	1	4	8,090	533					
	1642		207.75	1,644.8		4	7,379						
	1643		235.5	2,041.2		2	4,182						
	1644		195.5	1736.0		2	3,472						
	1645		227.75	2,022.4		4	8,090						
	1646		235.5	2,091.2		2	4,182						
	1647		195.5	1736.0	1	2	3,472						
Span 16 (Closure strip)	1661		198.0	1758.2	2	1	3,516			2			
	1662		198.0	1,403.0		1	2,806			1			
	1663		118.0	1,047.8		1	2,096			1			
	1664	12-0.6"ϕ	78.0	692.6		1	1,385	533		2			
Expansion joint segment	A	4-0.6"ϕ	88.5	314.4		4	675	178		2			
	B		96.0	77.0		4	616						
	C		29.76	88.1		4	705						
	D		27.25	80.7	2	4	646						
Pier segment 14	14051		29.75	88.1	4	2	705						
	14052		29.25	86.6			693						
	14053		26.5	78.4			627						
	14054/14055		26.125	77.3			618						
Pier segment 15	15051		26.875	79.6			637						
	15052		29.25	86.6			693						
	15053		29.25	86.6			693						
	15054/15055		26.875	79.6			637						
Pier segment 16	16051		27.75	82.1			657						
	16052		29.29	86.6			693						
	16053	4-0.6"ϕ	26.75	79.2	4	2	634	178		2			

DESIGNED BY JC
DRAWN BY JCG
CHECKED BY AM

BAR BENDING DIAGRAMS

(All dimensions are out-to-out)

Mark	A	B	C	D
SS 0301	7"	3"	8"	7"
SS 0302	3"	3"	11.1"	7"

SS0301, SS0302

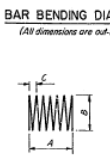

Mark	A	B	C
SB0304	10'5"	8"	13⅝"
SB0501	11'3"	11'2"	2'6"
SB0502	2'3"	1'6"	3"
DB0502	2'3"	1'6"	3"
DB0501	1'2⅛"	1'2⅛"	2'3⅛"

△ SB 0304, SB 0501, SB 0502, DB 0501, DB0502

BAR LIST

Mark	No.	Length	Pin Ø	Location	Bent	Str.
SB0304	~~848~~	16'-9"	—	Segment	•	
SB0501	184	29'-4"	—		•	
SB0502	~~282~~	5'-10"	—		•	
DB0502	336	5'-10"	—		•	
SB0301	24	4'-9"	2⅛"		•	
SB0302	24	7'-0"	2⅛"	Segment	•	
△ 216	864					
DB0501	16	29'-9"			•	

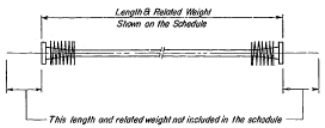

* ESTIMATED QUANTITIES △

Item	Unit	Quantity
Epoxy Coated Reinforcing Steel	Lbs.	—
Reinforcing Steel	Lbs.	~~41,791~~
		△ 41,516 ~~41,882~~ △

NOTE: * Reinforcing steel behind post tensioning anchorages is incidental to the post tensioning quantities.

Location	Tendon No.	Tendon Size	Tendon Length (Ft.)	Tendon Weight (Lbs.)	Number of Tendon per Location	Number of Location	Total Weight (Lbs.)	Stressing Force (Kips)		Bars/Tendon SB0304	SB0501	SB0502	SB0302
Pier segment 16	16054/16055	4-0.6"ϕ	26.0	77.0	4	2	616	178		2			
Pier segment 17	17051		27.75	82.1			657						
	17052		29.25	86.6			693						
	17053		26.75	79.2			634						
	17054/17055		26.0	77.0			616						
Pier segment 18	18051		26.875	79.6			637						
	18052		29.25	86.6			693						
	18053		29.25	86.6			693						
	18054/18055		26.875	79.6			637						
Pier segment 19	19051		29.75	88.1			705						
	19052		29.25	86.6			693						
	19053		26.5	78.4			627						
	19054/19055	4-0.6"ϕ	26.125	77.3	4	2	618	178		2			
Delta frame	—	9-0.6"ϕ	55.33	368.5	2	58	42,746	400				2	
	—	12-0.6"ϕ	66.0	586.1	1	58	33,993	500				2	
	—	3-0.6"ϕ	18.0	40.0	3	4	480	133			2	2	
						Subtotal	555,120						
Post tensioning bar		1¾"ϕ PT bar	13.8	41.5	2	60	4,980	102					
Stay anchorage segment		1¾"ϕ PT bar	13.8	41.5	4	4	664	102					
Segment S16(1)-30 & 61	1												
Spans 13 & 19, 14 & 18, 15 & 17 (Closure Strip)	1362	4-0.6"ϕ	283.8	840.0	2	2	3,360	178		2			
	1361	4-0.6"ϕ	298.6	883.9	2	2	3,535	178		2			
		1¾"ϕ PT bar	40	222.4	3	4	2,668	166 *					
		1¾"ϕ PT bar	20	111.2	3	104	34,694	166 *					
Seg. Mid Span (4)		1¾"ϕ PT bar	74' / 114'		2 / 2	2 / 2	3,136	189					

△ * See Sheets 229 & 273 for location.

Total weight tendons : ~~1,001,571 Lbs.~~ 1,008,466 Lbs. △

Total weight PT bars : ~~5,222 Lbs. 42,586 Lbs.~~ △ 45,722 Lbs.

* After Anchor Set △

N/A

N.B.L. & S.B.L. RTE. 295 OVER JAMES RIVER

MAIN SPAN UNIT
POST TENSIONING QUANTITIES

Figg and Muller Engineers, Inc.
Tallahassee, Fl. / Paris, Fr. / Washington, D.C. / Denver, Co.

△ Revised : July 31, 1987
△ Revised: April 20, 1987
△ Revised: March 25, 1987
△ Revised: March 31, 1986

November, 1984

260-32

Sheet 274 of 333

Appendix B. Original Main Span Construction Drawings

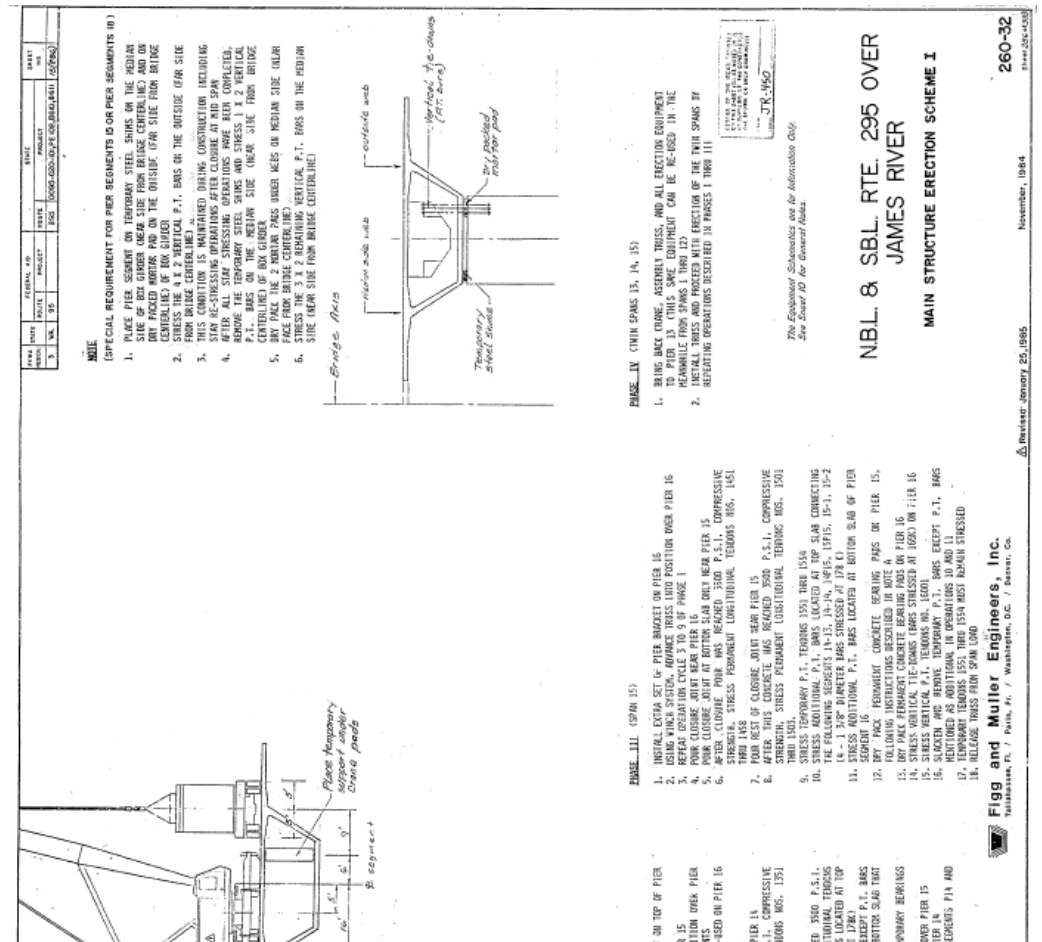

FHWA REGION	STATE	FEDERAL AID ROUTE	FEDERAL AID PROJECT	STATE ROUTE	STATE PROJECT	SHEET NO.
3	WA	90		295	0095-020-ICL,PE 108,B&B,B411	(1/287)

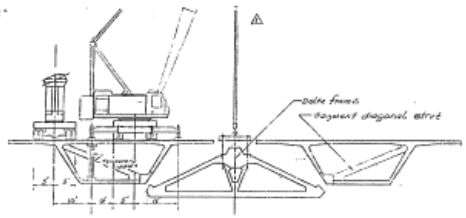

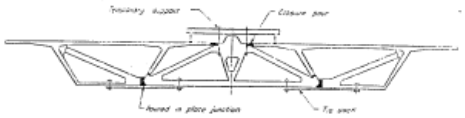

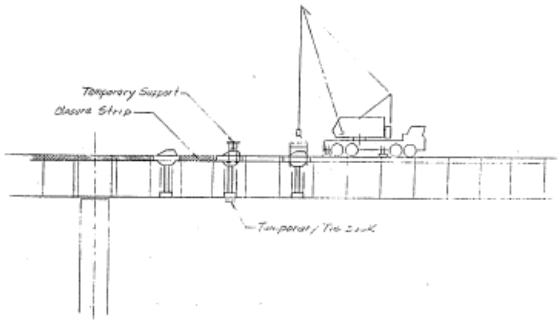

PHASE V

1. THE 3 SPAN TWIN STRUCTURE IS NOW COMPLETED, TRUSS MAY BE REMOVED
2. KEEP ON DECK HANDLING EQUIPMENT FOR DELTA FRAMES CONNECTING SEGMENTS OF SPANS 14 AND 15 TWIN STRUCTURE
3. BRING DELTA FRAME WITH TRAILER TRUCKS OVER THE DECK TO PROPER LOCATION TO BE LIFTED BY THE CRANE
4. USING THE CRANE LIFT AND ROTATE DELTA FRAME 90° ALLOWING IT TO BE LOWERED IN BETWEEN THE TWO STRUCTURES. ONCE THE DELTA FRAME IS BELOW DECK ROTATE IT BACK AND LIFT IT TO ITS FINAL POSITION
5. INSTALL TEMPORARY SUPPORT TO HOLD IT IN PLACE
6. POUR JUNCTION BETWEEN DELTA FRAME AND DIAGONAL STRUT INSIDE SEGMENTS
7. INSTALL FORMWORK UNDER SEGMENT FLANGES
8. POUR CONCRETE IN GAP BETWEEN DELTA FRAME AND SEGMENT ON EACH SIDE AT TOP SLAB LEVEL
9. AFTER THE CONCRETE OF DIAGONAL JUNCTION AND GAP AT TOP SLAB HAS REACHED 2500 P.S.I. COMPRESSIVE STRENGTH, STRESS CONTINUITY TRANSVERSE TENDON IN TOP SLAB (4-0.6" DIAMETER - TENDONS STRESSED AT 175 K)
10. THEN STRESS TRANSVERSE DIAGONAL TENDON ANCHORED IN SEGMENT BOTTOM SLAB (12 X 0.6" DIAMETER TENDON STRESSED AT 524 K)
11. REMOVE TEMPORARY SUPPORT FROM DELTA FRAME AND FORMWORK UNDER FLANGES
12. PROCEED TO ERECTION OF NEXT DELTA FRAME WITH THE SAME OPERATION PREVIOUSLY DESCRIBED
13. AFTER ALL DELTA FRAMES HAVE BEEN ERECTED INSTALL FORMWORK AND POUR CLOSURE STRIP REMAINING BETWEEN DELTA FRAMES AND THE FILL CLOSURE STRIP AT SPAN 13
14. STRESS ALL REMAINING TRANSVERSE CONTINUITY TENDONS ON SPANS 13 - 14 - 15.
15. REMOVE FORMWORK
16. CONSTRUCTION OF APPROACH IS NOW TERMINATED AND THE EQUIPMENT FOR CONSTRUCTION OF UPPER PART OF PYLON AND THE 630 FT MAIN SPAN CAN BE BROUGHT ON SITE OVER THE DECK.
    NOTE: LOW PART OF PYLON AND UPPER PART OF PYLON UP TO LAST SEGMENT BEFORE FIRST STAY CAN BE CONSTRUCTED DURING PHASES I THRU V. CANTILEVER SEGMENTS IN MAIN SPAN 16-1, 16-2, 16-3 CAN BE ERECTED AT END OF PHASES III AND IV, DURING WORK DESCRIBED IN PHASE V

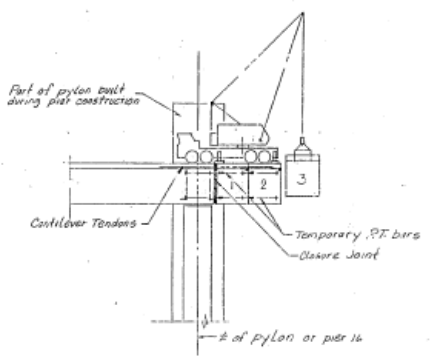

PHASE VI

1. THE 3 FIRST CANTILEVER SEGMENTS CAN BE BROUGHT OVER THE DECK BY TRAILER TRUCK, ALL THE OTHERS WILL BE ERECTED WITH BEAM AND WINCH METHOD.
2. POSITION CRANE ON TOP OF PIER 16
3. LIFT AND PLACE SEGMENT 16-1
4. PRIOR TO STRESSING TEMPORARY P.T. BARS BETWEEN 16-1 AND PIER SEGMENT P16 INSTALL SHIMS FOR CAST IN PLACE CLOSURE JOINT
5. ADJUST SEGMENT AND POUR CLOSURE CONCRETE
6. AFTER CONCRETE WAS REACHED 2500 P.S.I. COMPRESSIVE STRENGTH, STRESS CANTILEVER TENDON 16Z1 AT 533 K
   NOTE: SAME PRECEDING OPERATIONS CAN BE MADE SIMULTANEOUSLY OR SUCCESSIVELY ON TWIN GIRDER (TYPICAL TO ERECTION OF EACH SEGMENT)
7. AFTER BOTH SEGMENTS 16-1 ARE ERECTED AND CANTILEVER TENDONS ARE FULLY STRESSED MOVE CRANE OVER SEGMENT 16-1
8. LIFT AND PLACE SEGMENT 16-2 WITH CRANE
9. PRIOR TO ASSEMBLING WITH TEMPORARY P.T. BARS, APPLY EPOXY ON ONE FACE OF SEGMENT MATCHING WITH 16-1.
10. STRESS TEMPORARY P.T. BARS BETWEEN SEGMENT 16-1 AND SEGMENT 16-2 (FOR TEMPORARY P.T. BARS STRESSING AND AND SLACKENING SEE SPECIAL SHEETS 328 THRU 333.
11. REPEAT PRECEDING OPERATIONS 7-8-9-10 FOR ERECTION OF SEGMENTS 16-3

JR 830, 828

The Equipment Schematics are for Information Only. See Sheet 10 for General Notes.

N.B.L. & S.B.L. RTE. 295 OVER JAMES RIVER

MAIN STRUCTURE ERECTION SCHEME II

DESIGNED BY JP
DRAWN BY JC
CHECKED BY JP

Figg and Muller Engineers, Inc.
Tallahassee, Fl. / Paris, Fr. / Washington, D.C. / Denver, Co.

260-32
Sheet (287 of 880)

⚠ Revised: January 25, 1985

November, 1984

FHWA REGION	STATE	FEDERAL AID ROUTE	FEDERAL AID PROJECT	STATE ROUTE	STATE PROJECT	SHEET NO
3	VA.	95		295	0095-020-101,PE102,B501,B511 (0/2988)	

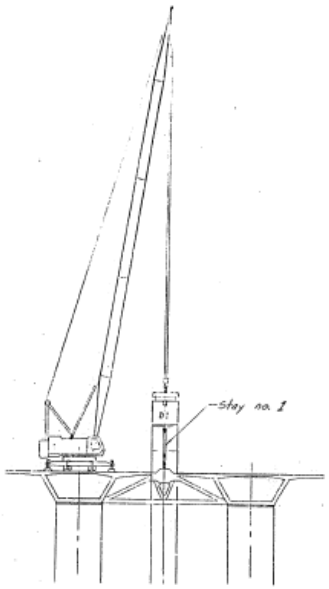

12. REMOVE CRANE FROM CANTILEVER
13. POSITION NEW CRANE NEAR PYLON FOR ERECTION OF STAYS AND PYLON SEGMENTS

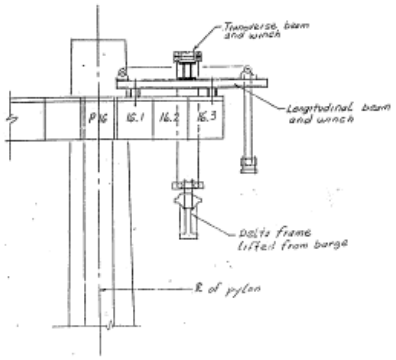

14. INSTALL BEAMS AND WINCHES EQUIPMENT ON BOTH GIRDERS OVER SEGMENTS 16-3
15. USING BEAM AND WINCH LIFT DELTA FRAME TYPE B FROM BARGE AND PLACE IT IN ITS PROPER POSITION NEAR PYLON
16. HOLD IT IN PLACE WITH TEMPORARY SUPPORT
17. CAST IN PLACE JUNCTION BETWEEN DELTA FRAME AND SEGMENT DIAGONALS
18. CAST IN PLACE GAP BETWEEN DELTA FRAME AND SEGMENT TOP SLAB EDGES
19. AFTER THIS CONCRETE HAS REACHED 2500 P.S.I. COMPRESSIVE STRENGTH, STRESS TOP SLAB TRANSVERSE CONTINUITY TENDONS THRU TOP OF DELTA FRAME
20. THEN STRESS TRANSVERSE DIAGONAL TENDONS ANCHORED AT BOTTOM SLAB OF SEGMENTS
21. RELEASE DELTA FRAME FROM TEMPORARY SUPPORT

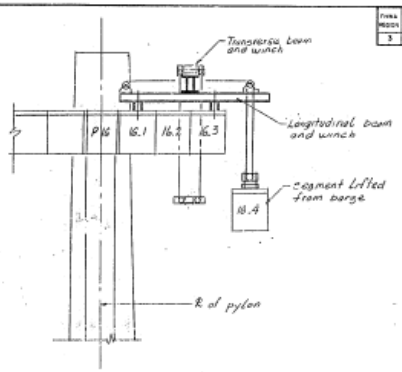

22. LIFT SEGMENTS 16-4 WITH BEAM AND WINCH
23. PRIOR TO ASSEMBLING WITH TEMPORARY P.T. BARS APPLY EPOXY ON ONE FACE MATCHING WITH SEGMENT ALREADY ERECTED
24. STRESS TEMPORARY P.T. BARS.
25. USING BEAM AND WINCH LIFT DELTA FRAME TYPE A AND PLACE IT IN ITS PROPER POSITION IN BETWEEN SEGMENTS 16-4
26. HOLD IT IN PLACE WITH TEMPORARY SUPPORT
27. CAST IN PLACE JUNCTION BETWEEN DELTA FRAME AND SEGMENT DIAGONALS
28. CAST IN PLACE GAP BETWEEN DELTA FRAME AND SEGMENT TOP SLAB EDGES AND CLOSURE STRIP BEHIND
29. AFTER THIS CONCRETE HAS REACHED 2500 P.S.I. COMPRESSIVE STRENGTH, STRESS TOP SLAB TRANSVERSE CONTINUITY TENDON THRU TOP OF DELTA FRAME AND CLOSURE STRIP BEHIND
30. THEN STRESS TRANSVERSE DIAGONAL TENDON ANCHORED AT BOTTOM SLAB OF SEGMENTS
31. REMOVE TEMPORARY SUPPORT FROM DELTA FRAME

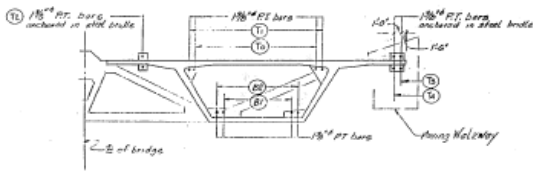

Main Span Temporary P.T. bar Location

SEE SHEETS 328 THRU 333 FOR INSTALLATION AND REMOVAL OF P.T. BARS.

JR 880,821

The Equipment Schematics are for Information Only. See Sheet 10 for General Notes.

N.B.L. & S.B.L. RTE. 295 OVER JAMES RIVER

MAIN STRUCTURE ERECTION SCHEME III

DESIGNED BY LP
DRAWN BY
CHECKED BY

Figg and Muller Engineers, Inc.
Tallahassee, Fl. / Paris, Fr. / Washington, D.C. / Denver, Co.

November, 1984

260-32

Sheet 289 of 333

FROM FEDERAL	STATE	FEDERAL AID ROUTE	FEDERAL AID PROJECT	STATE ROUTE	STATE PROJECT	SHEET NO
3	VA	95		295	(009-080-101,PE 100,B661,B611	260-32

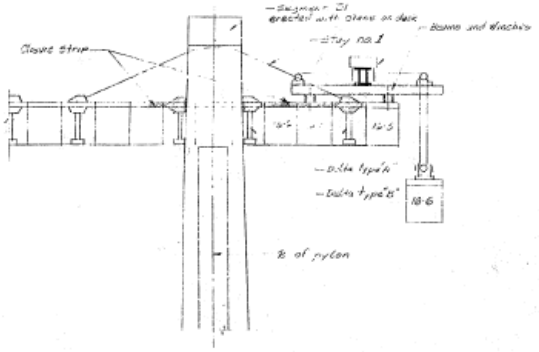

32. BRING STAY NO. 1 OVER THE DECK AND THREAD BOTH ENDS THRU THEIR ANCHORAGES IN DELTA FRAMES
33. USING CRANE POSITIOGED NEAR PYLON LIFT STAY NO. 1 AND PLACE IT IN ITS SADDLE PROVIDED IN PYLON SEGMENT C (SEGMENT C WAS ERECTED DURING CONSTRUCTION PHASES OF LOWER PART OF PYLON) AND STRESS STAY NO. 1 FROM BOTH ENDS (SEE SCHEDULE FOR STAY STRESSING FORCES)
34. APPLY EPOXY ON TOP OF PYLON SEGMENT C, LIFT AND PLACE PYLON SEGMENT D1 ON TOP OF PYLON SGMENT C AND STRESS TEMPORARY P.T. BARS.
35. USING BEAM AND WINCH, LIFT CANTILEVER SEGMENTS 16-5, 16-6 AND ASSEMBLE IT WITH THE SAME PROCEDURE DESCRIBED PREVIOUSLY IN OPERATIONS 21-22-23-24
36. LIFT AND PLACE DELTA FRAME CONNECTING WITH SEGMENTS 16-6 WITH THE SAME PROCEDURE DESCRIBED IN OPERATIONS 25-26 AND BE FOLLOWED WITH OPERATIONS 27, 28, 29, 30, 31
37. BRING STAY NO. 2 AND REPEAT SAME OPERATIONS AS FOR STAY NO. 1
38. APPLY EPOXY ON TOP OF PYLON SEGMENT D1 AND PLACE PYLON SEGMENT D2
39. STRESS TEMPORARY P.T. BARS
40. REPEAT FULL OPERATION CYCLE FOR ERECTING ALL OTHER CANTILEVER SEGMENTS, STAYS AND PYLON SEGMENTS UNTIL CANTILEVER SEGMENTS 16-30, STAY NO. 13 AND PYLON SEGMENT "E" IS ERECTED
41. STRESS VERTICAL P.T. TENDON IN PYLON FROM TOP OF PYLON SEGMENT "E" AND INSTALL PYLON CAP
42. INSTALL AND STRESS DECK TENDONS 16A1, 16A2, 16A8, AT 535 K
43. ERECT CANTILEVER SEGMENT 31

STAY	F STAY
1	1184 K
2	1645 K
3	1726 K
4	1620 K
5	1599 K
6	1551 K
7	1552 K
8	1557 K
9	1571 K
10	1564 K
11	1605 K
12	1633 K
13	1662 K

STAY STRESSING

FOR SEQUENCE OF STAY STRESSING, REFER TO SHEETS 328 THRU 335.

RESTRESS THE STAYS TO THE FOLLOWING FORCES

STAY		
1	~~2370 K~~	NO RESTRESSING
2	~~2370 K~~	2370 K
3	~~2370 K~~	2370 K
4	~~2370 K~~	2370 K
5	~~2370 K~~	2340 K
6	~~2370 K~~	2310 K
7	~~2370 K~~	2280 K
8	~~2370 K~~	2200 K
9	~~2370 K~~	2120 K
10	~~2370 K~~	2020 K
11	~~2370 K~~	1920 K
12	~~2370 K~~	1820 K
13	~~2370 K~~	~~2080 K~~ 2050 K

The Equipment Schematics are for Information Only. See Sheet 10 for General Notes.

LETTER OF THE ITEMS CONTAINED ON THIS SHEET IS A NOTE OF 'S' OR SUPPLIED BY THE CONTRACTOR ARE SHOWN ON MICRO FILM ONLY

JK 8/21/86

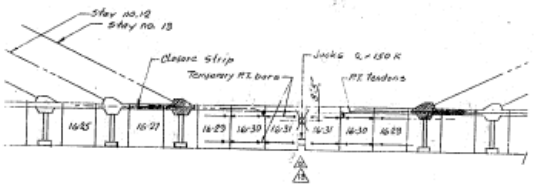

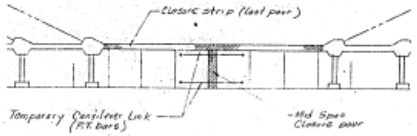

44. THE SOUTH CANTILEVER OF THE MAIN SPAN IS NOW COMPLETED AND ERECTION EQUIPMENT CAN BE REMOVED
THE NORTH CANTILEVER OF THE MAIN SPAN AND THE TRANSITION SPANS 17-18-19 ARE TO BE CONSTRUCTED THE SAME WAY AS THE SOUTH SIDE BY REPEATING ALL OPERATIONS OF PHASES I TO VI.
45. LINE UP NORTH AND SOUTH CANTILEVER. INSTALL JACKS IN CLOSURE GAP AT MID SPAN
46. INFLATE JACKS TO OBTAIN 300 K FOR A TOTAL OF 2 JACKS PER BOX GIRDER (SEE SKETCH FOR JACK LOCATION)
47. PLACE SHIM (AS SHOWN ON SKETCH) RELEASE JACKS AND REMOVE THEM
48. USE P.T. BARS TO LINK BOTH CANTILEVERS TEMPORARILY

46. INSTALL FORMWORK AND POUR MIDSPAN CLOSURE GAP
~~49. AFTER MID SPAN CLOSURE HAS REACHED 4500 P.S.I. COMPRESSIVE STRENGTH, INSTALL DECK CONTINUITY TENDONS AND PERMANENT P.T. BARS AND STRESS THEM IN THIS ORDER: 1601, 1602, 1603, PERMANENT PT. BARS (2 PER WEB), 1604, 1605 AND BALANCE OF TENDONS.~~
51. SLACKEN AND REMOVE REMAINING TEMPORARY P.T. BARS
52. GROUT ALL TENDONS
53. AFTER TRAFFIC BARRIER AND CONCRETE OVERLAY HAVE BEEN COMPLETED RE STRESS ALL STAYS TO THEIR FINAL FORCES (SEE SCHEDULE)
50. AFTER MID SPAN CLOSURE HAS REACHED 4500 P.S.I. COMPRESSIVE STRENGTH, INSTALL DECK CONTINUITY TENDONS AND PERMANENT P.T. BARS AND STRESS THEM IN THIS ORDER: 1601, 1602, 1603, PERMANENT PT. BARS (2 PER WEB), 1604, 1605 AND BALANCE OF TENDONS.

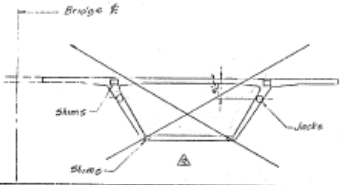

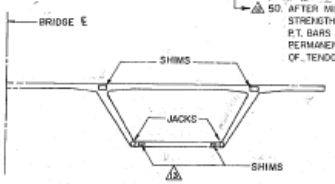

N.B.L. & S.B.L. RTE. 295 OVER JAMES RIVER

MAIN STRUCTURE ERECTION SCHEME IV

DESIGNED BY L.P.
DRAWN BY ...
CHECKED BY ...

Figg and Muller Engineers, Inc.
Tallahassee, Fl. / Paris, Fr. / Washington, D.C. / Denver, Co.

Revised: August 21, 1987
Revised: July 31, 1987

November, 1984

260-32

GENERAL NOTES

1. THE ERECTION SEQUENCE WHICH FOLLOWS DEPICTS THE PROGRESSIVE CANTILEVER CONSTRUCTION OF THE MAINSPAN BEGINNING AT PIER 16. THE SEQUENCE OF ERECTION IS IDENTICAL FOR MAINSPAN CONSTRUCTION BEGINNING AT PIER 17.
2. COUPLERS AND ANCHOR PLATES FOR P.T. BARS ARE DENOTED AS:

   PLATE —— COUPLER
3. PERMANENT P.T. TENDON NUMBERS ARE AS DESIGNATED IN THE POST-TENSIONING DRAWINGS.
4. FOR LOCATION AND DESIGNATION OF TEMPORARY P.T. BARS SEE SHEET 327.
5. CABLE STAYS WHICH ARE CONTINUOUS THROUGH THE PYLON, SHALL BE STRESSED SIMULTANEOUSLY AT BOTH ENDS

FHWA REGION	STATE	FEDERAL AID ROUTE	FEDERAL AID PROJECT	STATE ROUTE	STATE PROJECT	SHEET NO
3	VA	95		295	0095-020-10,PE102,B610,B611 (5)208	

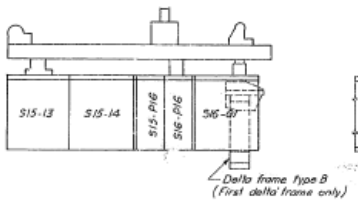

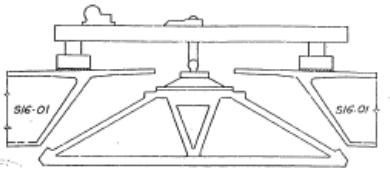

PHASE 2- DELTA FRAME ASSEMBLY

(CONSTRUCTION PHASES IDENTICAL FOR ALL DELTA FRAMES IN MAIN SPAN)

(A) LIFT DELTA FRAME FROM BARGE
(B) POUR CAST IN PLACE JOINTS IN TOP SLAB AND PLACE PACK MORTAR AT DELTA FRAME/SEGMENT BOTTOM CONNECTION
(C) WHEN CIP CONCRETE STRENGTH REACHES 3500 PSI, STRESS ALL TRANSVERSE TOP SLAB CONTINUITY TENDONS AND DELTA FRAME TRANSVERSE POST-TENSIONING OF SEGMENTS S16-01.

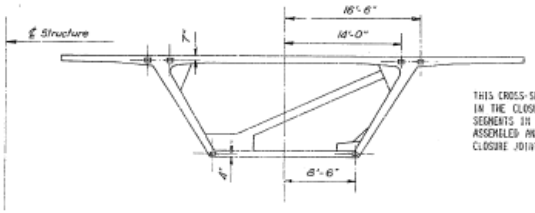

THIS CROSS-SECTION SHOWS THE LOCATION OF 6 - 6" X 8" SHIMS PLACED IN THE CLOSURE JOINTS BETWEEN THE PIER SEGMENTS AND THE FIRST SEGMENTS IN CANTILEVER. ONCE THE FIRST CANTILEVER SEGMENTS ARE ASSEMBLED AND ORIENTED TO GIVE THE FINAL ROADWAY ALIGNMENT, THE CLOSURE JOINTS ARE POURED.

LOCATION OF SHIMS

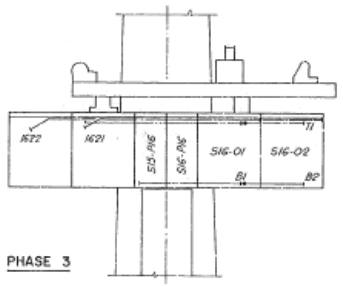

PHASE 3

(A) MOVE BEAM AND WINCH TO SEGMENTS S16-01
(B) LIFT SEGMENTS S16-02 FROM BARGE
(C) COUPLE AND STRESS P.T. BARS T1 AND B2 IN SEGMENT S16-02
(D) STRESS TENDONS 1622
(E) STRESS P.T. BARS B1 BETWEEN SEGMENTS S15-P16 AND S16-01

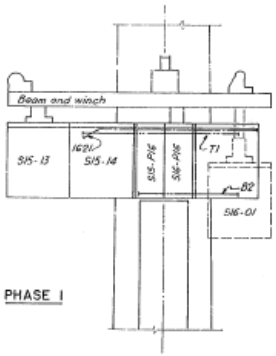

PHASE 1

(A) ASSEMBLE BEAM AND WINCH ABOVE PIER 16
(B) SECURE SHIMS TO FREE FACE OF SEGMENTS S16-P16
(C) LIFT SEGMENTS S16-01 WITH BEAM AND WINCH FROM BARGE
(D) STRESS P.T. BARS T1 BETWEEN SEGMENTS S15-14 AND S16-01 AND P.T. BARS B2 BETWEEN SEGMENTS S15-P16 AND S16-01
(E) ADJUST SEGMENTS S16-01 TO REQUIRED ELEVATIONS
(F) POUR CLOSURE JOINTS
(G) WHEN CIP JOINT CONCRETE STRENGTH HAS REACHED 2500 PSI STRESS TENDONS 1621 FROM CANTILEVER END.

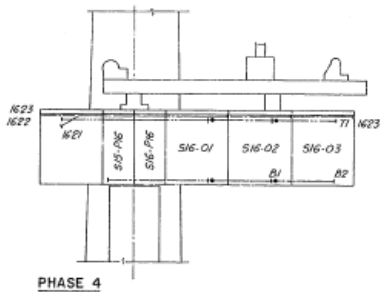

PHASE 4

JR-820

(A) ADVANCE BEAM AND WINCH TO SEGMENTS S16-02
(B) LIFT SEGMENTS S16-03 FROM BARGE
(C) COUPLE AND STRESS P.T. BARS T1 AND B2 IN SEGMENTS S16-03
(D) STRESS TENDONS 1623
(E) COUPLE AND STRESS P.T. BARS B1 IN SEGMENTS S16-02

The Equipment Schematics are for Information Only See Sheet 10 for General Notes.

N.B.L. & S.B.L. RTE. 295 OVER JAMES RIVER

MAIN SPAN
ERECTION SEQUENCE I

DESIGNED BY J.P.
DRAWN BY J.B.
CHECKED BY J.C.

Figg and Muller Engineers, Inc.
Tallahassee, Fl. / Paris, Fr. / Washington, D.C. / Denver, Co.

No scale

November, 1984

260-32

REGION	STATE	FEDERAL AID		STATE		SHEET NO
		ROUTE	PROJECT	ROUTE	PROJECT	
3	VA.	95		295	0009-080-819,PE 02,B60,B611	19 OF 33

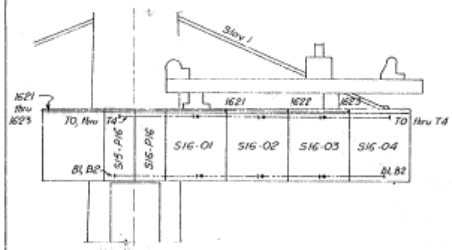

PHASE 5

(A) ADVANCE BEAM AND WINCH TO SEGMENTS S16-03
(B) LIFT SEGMENTS S16-04 FROM BARGE
(C) COUPLE AND STRESS P.T. BARS T1 AND B2 IN SEGMENTS S16-04
(D) STRESS P.T. BARS T0, T2, T3, T4 FROM SEGMENTS S15-P16 TO SEGMENTS S16-04
(E) COUPLE AND STRESS P.T. BAR B1 IN SEGMENTS S16-04
(F) LIFT DELTA FRAME OF SEGMENTS S16-04
(G) PLACE DRY PACKED MORTAR BETWEEN DELTA FRAME AND SEGMENT WEBS
(H) POUR CIP CONCRETE CLOSURE IN TOP SLAB FOR SEGMENTS S16-02, S16-03, S16-04
(I) WHEN THE CIP CONCRETE REACHES A MINIMUM COMPRESSIVE STRENGTH OF 3500 PSI, STRESS THE 1200.6" STRAND TENDON OF THE DELTA FRAME AND ALL TRANSVERSE CONTINUITY POST TENSIONING OF SEGMENTS S16-02, S16-03, S16-04
(J) ASSEMBLE STAY 1 AND STRESS TO 1480 KIPS
(K) REMOVE P.T. BARS T1 FROM SEGMENTS S15-14

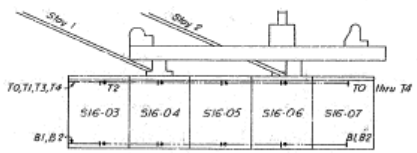

PHASE 8

(A) ADVANCE BEAM AND WINCH TO SEGMENTS S16-06
(B) LIFT SEGMENTS S16-07 FROM BARGE
(C) COUPLE AND STRESS P.T. BARS T3 AND B2 IN SEGMENTS S16-07
(D) COUPLE AND STRESS P.T. BARS T0, T2, T3, T4 IN SEGMENTS S16-07
(E) COUPLE AND STRESS P.T. BAR B1 IN SEGMENTS S16-07

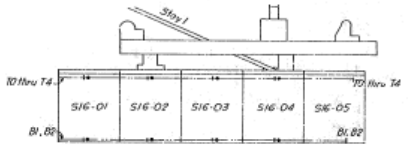

PHASE 6

(A) ADVANCE BEAM AND WINCH TO SEGMENTS S16-04
(B) LIFT SEGMENTS S16-05 FROM BARGE
(C) COUPLE AND STRESS P.T. BARS T1 AND B2 IN SEGMENTS S16-05
(D) COUPLE AND STRESS P.T. BARS T0, T2, T3, T4 IN SEGMENTS S16-05
(E) COUPLE AND STRESS P.T. BARS B1 IN SEGMENTS S16-05

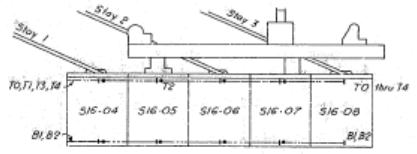

PHASE 9

(A) ADVANCE BEAM AND WINCH TO SEGMENTS S16-07
(B) LIFT SEGMENTS S16-08 FROM BARGE
(C) COUPLE AND STRESS P.T. BARS T3 AND B2 IN SEGMENTS S16-08
(D) COUPLE AND STRESS P.T. BARS T0, T2, T3, T4 IN SEGMENTS S16-08
(E) COUPLE AND STRESS P.T. BAR B1 IN SEGMENTS S16-08
(F) LIFT DELTA FRAME OF SEGMENTS S16-08
(G) PLACE DRY PACKED MORTAR BETWEEN DELTA FRAME AND SEGMENT WEBS
(H) POUR CIP CONCRETE CLOSURE IN TOP SLAB FOR SEGMENTS S16-07 AND S16-08
(I) WHEN THE CIP CONCRETE REACHES A MINIMUM COMPRESSIVE STRENGTH OF 3500 PSI, STRESS THE 1200.6" STRAND TENDON OF THE DELTA FRAME AND ALL TRANSVERSE CONTINUITY POST TENSIONING OF SEGMENTS S16-07 AND S16-08
(J) ASSEMBLE STAY 3 AND STRESS TO 1480 KIPS
(K) REMOVE P.T. BARS T2 FROM SEGMENTS S16-03 THRU S16-04

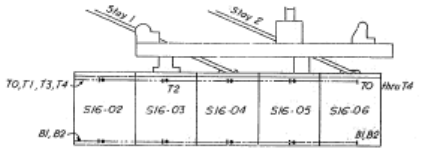

PHASE 7

(A) ADVANCE BEAM AND WINCH TO SEGMENTS S16-05
(B) LIFT SEGMENTS S16-06 FROM BARGE
(C) COUPLE AND STRESS P.T. BARS T1 AND B2 IN SEGMENTS S16-06
(D) COUPLE AND STRESS P.T. BARS T0, T2, T3, T4 IN SEGMENTS S16-06
(E) COUPLE AND STRESS P.T. BAR B1 IN SEGMENTS S16-06
(F) LIFT DELTA FRAME OF SEGMENTS S16-06
(G) PLACE DRY PACKED MORTAR BETWEEN DELTA FRAME AND SEGMENT WEBS
(H) POUR CIP CONCRETE CLOSURE IN TOP SLAB FOR SEGMENTS S16-05 AND S16-06
(I) WHEN THE CIP CONCRETE REACHES A MINIMUM COMPRESSIVE STRENGTH OF 3500 PSI, STRESS THE 1200.6" STRAND TENDON OF THE DELTA FRAME AND ALL TRANSVERSE CONTINUITY POST TENSIONING OF SEGMENTS S16-05 AND S16-06
(J) ASSEMBLE STAY 2 AND STRESS TO 1480 KIPS
(K) REMOVE P.T. BARS T2 FROM SEGMENTS S15-P16 THRU S16-02

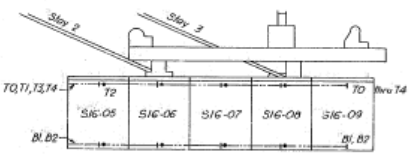

PHASE 10

DETAILS OF THIS ITEM DIFFERED ON THIS SHEET (IF IN AGREEMENT) TO BE SUPPLIED BY THE CONTRACTOR AND SHOWN ON SHOP DRAWINGS

JR-921

(A) ADVANCE BEAM AND WINCH TO SEGMENTS S16-08
(B) LIFT SEGMENTS S16-09 FROM BARGE
(C) COUPLE AND STRESS P.T. BARS T3 AND B2 IN SEGMENTS S16-09
(D) COUPLE AND STRESS P.T. BARS T0, T2, T3, T4 IN SEGMENTS S16-09
(E) COUPLE AND STRESS P.T. BAR B1 IN SEGMENTS S16-09

The Equipment Schematics are for Information Only! See Sheet 10 for General Notes.

N.B.L. & S.B.L. RTE. 295 OVER JAMES RIVER

MAIN SPAN ERECTION SEQUENCE II

DESIGNED BY LP
DRAWN BY JR
CHECKED BY J.C.

Figg and Muller Engineers, Inc.
Tallahassee, Fl. / Paris, Fr. / Washington, D.C. / Denver, Co.

No scale

November, 1984

260-32

Sheet 329 of 333

FHWA REGION	STATE	FEDERAL AID ROUTE	FEDERAL AID PROJECT	STATE ROUTE	STATE PROJECT	SHEET NO
3	VA	95		295	0099-020-101,PE 102,B660,B611	15 (380)

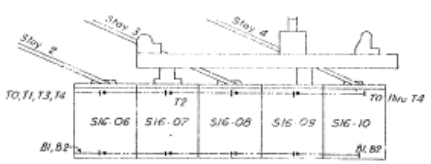

PHASE 11

(A) ADVANCE BEAM AND WINCH TO SEGMENTS S16-09
(B) LIFT SEGMENTS S16-10 FROM BARGE
(C) COUPLE AND STRESS P.T. BARS T1 AND B2 IN SEGMENTS S16-10
(D) COUPLE AND STRESS P.T. BARS T0, T2, T3, T4 IN SEGMENTS S16-10
(E) COUPLE AND STRESS P.T. BAR B1 IN SEGMENTS S16-10
(F) LIFT DELTA FRAME OF SEGMENTS S16-10
(G) PLACE DRY PACKED MORTAR BETWEEN DELTA FRAME AND SEGMENT WEBS
(H) POUR CIP CONCRETE CLOSURE IN TOP SLAB FOR SEGMENTS S16-09 AND S16-10
(I) WHEN THE CIP CONCRETE REACHES A MINIMUM COMPRESSIVE STRENGTH OF 3500 PSI, STRESS THE 12X0.6" STRAND TENDON OF THE DELTA FRAME AND ALL TRANSVERSE CONTINUITY POST TENSIONING OF SEGMENTS S16-09 AND S16-10
(J) ASSEMBLE STAY 4 AND STRESS TO 1480 KIPS
(K) REMOVE P.T. BARS T2 FROM SEGMENTS S16-05 THRU S16-06. REMOVE P.T. BARS T3 AND T4 FROM SEGMENTS S15-P16 THROUGH S16-02.

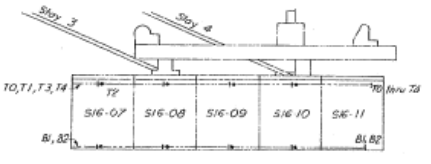

PHASE 12

(A) ADVANCE BEAM AND WINCH TO SEGMENTS S16-10
(B) LIFT SEGMENTS S16-11 FROM BARGE
(C) COUPLE AND STRESS P.T. BARS T1 AND B2 IN SEGMENTS S16-11
(D) COUPLE AND STRESS P.T. BARS T0, T2, T3, T4 IN SEGMENTS S16-11
(E) COUPLE AND STRESS P.T. BAR B1 IN SEGMENTS S16-11

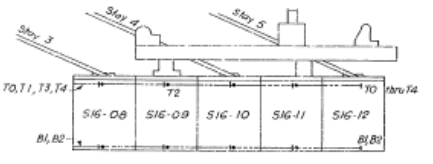

PHASE 13

(A) ADVANCE BEAM AND WINCH TO SEGMENTS S16-11
(B) LIFT SEGMENTS S16-12 FROM BARGE
(C) COUPLE AND STRESS P.T. BARS T1 AND B2 IN SEGMENTS S16-12
(D) COUPLE AND STRESS P.T. BARS T0, T2, T3, T4 IN SEGMENTS S16-12
(E) COUPLE AND STRESS P.T. BAR B1 IN SEGMENTS S16-12
(F) LIFT DELTA FRAME OF SEGMENTS S16-12
(G) PLACE DRY PACKED MORTAR BETWEEN DELTA FRAME AND SEGMENT WEBS
(H) POUR CIP CONCRETE CLOSURE IN TOP SLAB FOR SEGMENTS S16-11 AND S16-12
(I) WHEN THE CIP CONCRETE REACHES A MINIMUM COMPRESSIVE STRENGTH OF 3500 PSI, STRESS THE 12X0.6" STRAND TENDON OF THE DELTA FRAME AND ALL TRANSVERSE CONTINUITY POST TENSIONING OF SEGMENTS S16-11 AND S16-12
(J) REMOVE P.T. BARS B1 FROM SEGMENTS S15-P16 THROUGH S16-02
(K) SLACKEN TENDONS 1551 THROUGH 1554
(L) REMOVE P.T. BARS OF PIER SEGMENT P15 AND P.T. BARS IN TOP SLAB OF SEGMENTS S14-13, S14-15, S15-01, S15-02
(M) ASSEMBLE AND STRESS STAY 5 TO 1480 KIPS
(N) REMOVE P.T. BARS T2 FROM SEGMENTS S16-07 AND S16-08. REMOVE P.T. BARS T3 AND T4 FROM SEGMENTS S16-03 AND S16-04.

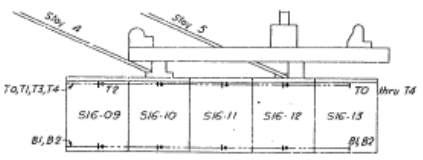

PHASE 14

(A) ADVANCE BEAM AND WINCH TO SEGMENTS S16-12
(B) LIFT SEGMENTS S16-13 FROM BARGE
(C) COUPLE AND STRESS P.T. BARS T1 AND B2 IN SEGMENTS S16-13
(D) COUPLE AND STRESS P.T. BARS T0, T2, T3, T4 IN SEGMENTS S16-13
(E) COUPLE AND STRESS P.T. BAR B1 IN SEGMENTS S16-13

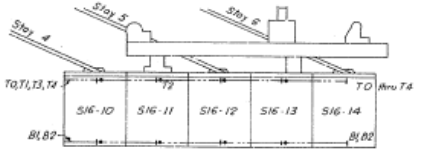

PHASE 15

(A) ADVANCE BEAM AND WINCH TO SEGMENTS S16-13
(B) LIFT SEGMENTS S16-14 FROM BARGE
(C) COUPLE AND STRESS P.T. BARS T1 AND B2 IN SEGMENTS S16-14
(D) COUPLE AND STRESS P.T. BARS T0, T2, T3, T4 IN SEGMENTS S16-14
(E) COUPLE AND STRESS P.T. BAR B1 IN SEGMENTS S16-14
(F) LIFT DELTA FRAME OF SEGMENTS S16-14
(G) PLACE DRY PACKED MORTAR BETWEEN DELTA FRAME AND SEGMENT WEBS
(H) POUR CIP CONCRETE CLOSURE IN TOP SLAB FOR SEGMENTS S16-13 AND S16-14
(I) WHEN THE CIP CONCRETE REACHES A MINIMUM COMPRESSIVE STRENGTH OF 3500 PSI, STRESS THE 12X0.6" STRAND TENDON OF THE DELTA FRAME AND ALL TRANSVERSE CONTINUITY POST TENSIONING OF SEGMENTS S16-13 AND S16-14
(J) REMOVE P.T. BARS B1 FROM SEGMENTS S16-3 AND S16-4
(K) ASSEMBLE AND STRESS STAY 6 TO 1480 KIPS
(L) REMOVE P.T. BARS T2 FROM SEGMENTS S16-09 AND S16-10
REMOVE P.T. BARS T3 AND T4 FROM SEGMENTS S16-05 AND S16-06
REMOVE P.T. BARS T0 AND T1 FROM SEGMENTS S15-P16 THROUGH S16-02

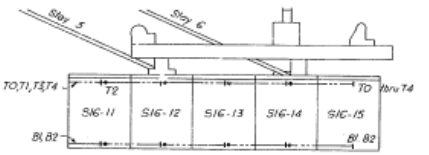

PHASE 16

JR-822

(A) ADVANCE BEAM AND WINCH TO SEGMENTS S16-14
(B) LIFT SEGMENTS S16-15 FROM BARGE
(C) COUPLE AND STRESS P.T. BARS T1 AND B2 IN SEGMENTS S16-15
(D) COUPLE AND STRESS P.T. BARS T0, T2, T3, T4 IN SEGMENTS S16-15
(E) COUPLE AND STRESS P.T. BAR B1 IN SEGMENTS S16-15

The Equipment Schematics are for Information Only
See Sheet 10 for General Notes.

N.B.L. & S.B.L. RTE. 295 OVER JAMES RIVER

MAIN SPAN
ERECTION SEQUENCE III

DESIGNED BY E.P
DRAWN BY J.R.
CHECKED BY J.C.

Figg and Muller Engineers, Inc.
Tallahassee, Fl. / Paris, Fr. / Washington, D.C. / Denver, Co.

No scale

November, 1984

260-32

FHWA REGION	STATE	FEDERAL AID		STATE		SHEET
		STATE	PROJECT	ROUTE	PROJECT	NO
3	VA	95		295	0095-020-101,PE 102,B610,B611	15(33)

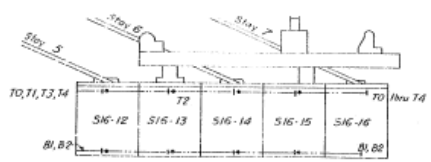

PHASE 17

(A) ADVANCE BEAM AND WINCH TO SEGMENTS S16-15
(B) LIFT SEGMENTS S16-16 FROM BARGE
(C) COUPLE AND STRESS P.T. BARS T1 AND B2 IN SEGMENTS S16-16
(D) COUPLE AND STRESS P.T. BARS T0, T2, T3, . . IN SEGMENTS S16-16
(E) COUPLE AND STRESS P.T. BAR B1 IN SEGMENTS S16-16
(F) LIFT DELTA FRAME OF SEGMENTS S16-16
(G) PLACE DRY PACKED MORTAR BETWEEN DELTA FRAME AND SEGMENT WEBS
(H) POUR CIP CONCRETE CLOSURE IN TOP SLAB FOR SEGMENTS S16-15 AND S16-16
(I) WHEN THE CIP CONCRETE REACHES A MINIMUM COMPRESSIVE STRENGTH OF 3500 PSI, STRESS THE 12X0.6" STRAND TENDON OF THE DELTA FRAME AND ALL TRANSVERSE CONTINUITY POST TENSIONING OF SEGMENTS S16-15 AND S16-16
(J) REMOVE P.T. BARS B1 FROM SEGMENTS S16-05 AND S16-06
(K) ASSEMBLE AND STRESS STAY 7 TO 1480 KIPS
(L) REMOVE P.T. BARS T2 FROM SEGMENTS S16-11 AND S16-12
REMOVE P.T. BARS T3 AND T4 FROM SEGMENTS S16-07 AND S16-08
REMOVE P.T. BARS T0 AND T1 FROM SEGMENTS S16-03 AND S16-04

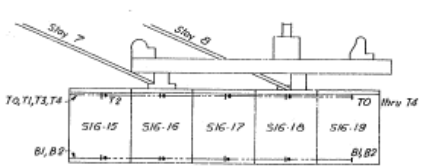

PHASE 20

(A) ADVANCE BEAM AND WINCH TO SEGMENTS S16-18
(B) LIFT SEGMENTS S16-19 FROM BARGE
(C) COUPLE AND STRESS P.T. BARS T1 AND B2 IN SEGMENTS S16-19
(D) COUPLE AND STRESS P.T. BARS T0, T2, T3, T4 IN SEGMENTS S16-19
(E) COUPLE AND STRESS P.T. BAR B1 IN SEGMENTS S16-19

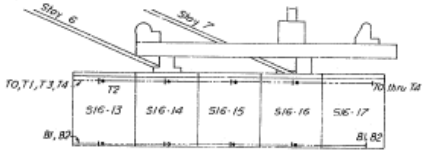

PHASE 18

(A) ADVANCE BEAM AND WINCH TO SEGMENTS S16-16
(B) LIFT SEGMENTS S16-17 FROM BARGE
(C) COUPLE AND STRESS P.T. BARS T1 AND B2 IN SEGMENTS S16-17
(D) COUPLE AND STRESS P.T. BARS T0, T2, T3, T4 IN SEGMENTS S16-17
(E) COUPLE AND STRESS P.T. BAR B1 IN SEGMENTS S16-17

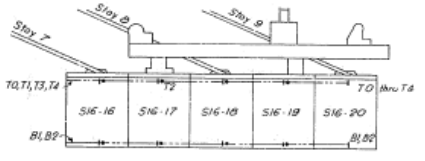

PHASE 21

(A) ADVANCE BEAM AND WINCH TO SEGMENTS S16-19
(B) LIFT SEGMENTS S16-20 FROM BARGE
(C) COUPLE AND STRESS P.T. BARS T1 AND B2 IN SEGMENTS S16-20
(D) COUPLE AND STRESS P.T. BARS T0, T2, T3, T4 IN SEGMENTS S16-20
(E) COUPLE AND STRESS P.T. BAR B1 IN SEGMENTS S16-20
(F) LIFT DELTA FRAME OF SEGMENTS S16-20
(G) PLACE DRY PACKED MORTAR BETWEEN DELTA FRAME AND SEGMENT WEBS
(H) POUR CIP CONCRETE CLOSURE IN TOP SLAB FOR SEGMENTS S16-19 AND S16-20
(I) WHEN THE CIP CONCRETE REACHES A MINIMUM COMPRESSIVE STRENGTH OF 3500 PSI, STRESS THE 12X0.6" STRAND TENDON OF THE DELTA FRAME AND ALL TRANSVERSE CONTINUITY POST TENSIONING OF SEGMENTS S16-19 AND S16-20
(J) REMOVE P.T. BARS B1 FROM SEGMENTS S16-09 AND S16-10
REMOVE P.T. BARS B2 FROM SEGMENTS S16-01 AND S16-02
(K) ASSEMBLE AND STRESS STAY 9 TO 1480 KIPS
(L) REMOVE P.T. BARS T2 FROM SEGMENTS S16-15 AND S16-16
REMOVE P.T. BARS T3 AND T4 FROM SEGMENTS S16-11 AND S16-12
REMOVE P.T. BARS T0 AND T1 FROM SEGMENTS S16-07 AND S16-08

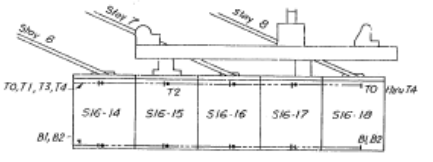

PHASE 19

(A) ADVANCE BEAM AND WINCH TO SEGMENTS S16-17
(B) LIFT SEGMENTS S16-18 FROM BARGE
(C) COUPLE AND STRESS P.T. BARS T1 AND B2 IN SEGMENTS S16-18
(D) COUPLE AND STRESS P.T. BARS T0, T2, T3, T4 IN SEGMENTS S16-18
(E) COUPLE AND STRESS P.T. BAR B1 IN SEGMENTS S16-18
(F) LIFT DELTA FRAME OF SEGMENTS S16-18
(G) PLACE DRY PACKED MORTAR BETWEEN DELTA FRAME AND SEGMENT WEBS
(H) POUR CIP CONCRETE CLOSURE IN TOP SLAB FOR SEGMENTS S16-17 AND S16-18
(I) WHEN THE CIP CONCRETE REACHES A MINIMUM COMPRESSIVE STRENGTH OF 3500 PSI, STRESS THE 12X0.6" STRAND TENDON OF THE DELTA FRAME AND ALL TRANSVERSE CONTINUITY POST TENSIONING OF SEGMENTS S16-17 AND S16-18
(J) REMOVE P.T. BARS B1 FROM SEGMENTS S16-07 AND S16-08
REMOVE P.T. BARS B2 FROM SEGMENTS S15-P16 AND S16-P16
(K) ASSEMBLE AND STRESS STAY 8 TO 1480 KIPS
(L) REMOVE P.T. BARS T2 FROM SEGMENTS S16-13 AND S16-14
REMOVE P.T. BARS T3 AND T4 FROM SEGMENTS S16-09 AND S16-10
REMOVE P.T. BARS T0 AND T1 FROM SEGMENTS S16-05 AND S16-06

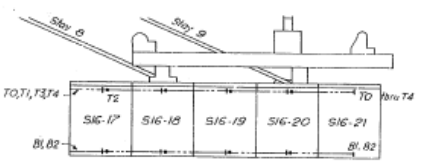

PHASE 22

JR-825

(A) ADVANCE BEAM AND WINCH TO SEGMENTS S16-20
(B) LIFT SEGMENTS S16-21 FROM BARGE
(C) COUPLE AND STRESS P.T. BARS T1 AND B2 IN SEGMENTS S16-21
(D) COUPLE AND STRESS P.T. BARS T0, T2, T3, T4 IN SEGMENTS S16-21
(E) COUPLE AND STRESS P.T. BAR B1 IN SEGMENTS S16-21

The Equipment Schematics are for Information Only
See Sheet 10 for General Notes

N.B.L. & S.B.L. RTE. 295 OVER JAMES RIVER

MAIN SPAN
ERECTION SEQUENCE IV

DESIGNED BY LP
DRAWN BY JR
CHECKED BY MG

Figg and Muller Engineers, Inc.
Tallahassee, Fl. / Paris, Fr. / Washington, D.C. / Denver, Co.

No scale

November, 1984

260-32

Sheet 33 of 133

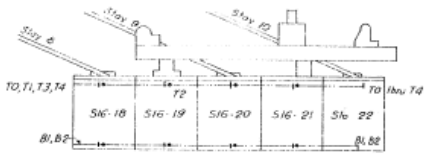

PHASE 23

(A) ADVANCE BEAM AND WINCH TO SEGMENTS S16-21
(B) LIFT SEGMENTS S16-22 FROM BARGE
(C) COUPLE AND STRESS P.T. BARS T1 AND B2 IN SEGMENTS S16-22
(D) COUPLE AND STRESS P.T. BARS T0, T2, T3, T4 IN SEGMENTS S16-22
(E) COUPLE AND STRESS P.T. BAR B1 IN SEGMENTS S16-22
(F) LIFT DELTA FRAME OF SEGMENTS S16-22
(G) PLACE DRY PACKED MORTAR BETWEEN DELTA FRAME AND SEGMENT WEBS
(H) POUR CIP CONCRETE CLOSURE IN TOP SLAB FOR SEGMENTS S16-21 AND S16-22
(I) WHEN THE CIP CONCRETE REACHES A MINIMUM COMPRESSIVE STRENGTH OF 3500 PSI, STRESS THE 12X0.6" STRAND TENDON OF THE DELTA FRAME AND ALL TRANSVERSE CONTINUITY POST TENSIONING OF SEGMENTS S16-21 AND S16-22
(J) REMOVE P.T. BARS B1 FROM SEGMENTS S16-11 AND S16-12
REMOVE P.T. BARS B2 FROM SEGMENTS S16-03 AND S16-04
(K) ASSEMBLE AND STRESS STAY 10 TO 1480 KIPS
(L) REMOVE P.T. BARS T2 FROM SEGMENTS S16-17 AND S16-18
REMOVE P.T. BARS T3 AND T4 FROM SEGMENTS S16-13 AND S16-14
REMOVE P.T. BARS T0 AND T1 FROM SEGMENTS S16-09 AND S16-10

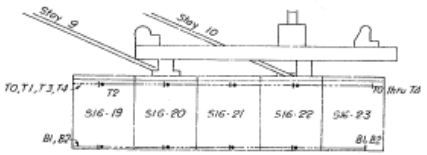

PHASE 24

(A) ADVANCE BEAM AND WINCH TO SEGMENTS S16-22
(B) LIFT SEGMENTS S16-23 FROM BARGE
(C) COUPLE AND STRESS P.T. BARS T1 AND B2 IN SEGMENTS S16-23
(D) COUPLE AND STRESS P.T. BARS T0, T2, T3, T4 IN SEGMENTS S16-23
(E) COUPLE AND STRESS P.T. BAR B1 IN SEGMENTS S16-23

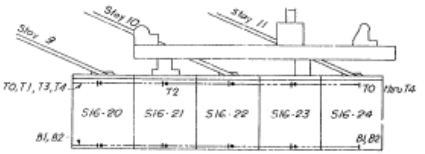

PHASE 25

(A) ADVANCE BEAM AND WINCH TO SEGMENTS S16-23
(B) LIFT SEGMENTS S16-24 FROM BARGE
(C) COUPLE AND STRESS P.T. BARS T1 AND B2 IN SEGMENTS S16-24
(D) COUPLE AND STRESS P.T. BARS T0, T2, T3, T4 IN SEGMENTS S16-24
(E) COUPLE AND STRESS P.T. BAR B1 IN SEGMENTS S16-24
(F) LIFT DELTA FRAME OF SEGMENTS S16-24
(G) PLACE DRY PACKED MORTAR BETWEEN DELTA FRAME AND SEGMENT WEBS
(H) POUR CIP CONCRETE CLOSURE IN TOP SLAB FOR SEGMENTS S16-23 AND S16-24
(I) WHEN THE CIP CONCRETE REACHES A MINIMUM COMPRESSIVE STRENGTH OF 3500 PSI, STRESS THE 12X0.6" STRAND TENDON OF THE DELTA FRAME AND ALL TRANSVERSE CONTINUITY POST TENSIONING OF SEGMENTS S16-23 AND S16-24
(J) REMOVE P.T. BARS B1 FROM SEGMENTS S16-13 AND S16-14
REMOVE P.T. BARS B2 FROM SEGMENTS S16-05 AND S16-06
(K) ASSEMBLE AND STRESS STAY 11 TO 1480 KIPS
(L) REMOVE P.T. BARS T2 FROM SEGMENTS S16-19 AND S16-20
REMOVE P.T. BARS T3 AND T4 FROM SEGMENTS S16-15 AND S16-16
REMOVE P.T. BARS T0 AND T1 FROM SEGMENTS S16-11 AND S16-12

FHWA REGION	STATE	ROUTE	PROJECT	ROUTE	PROJECT	SHEET NO.
3	VA	95		295	0095-020-101,PE-102,B610,B611	9 (132)

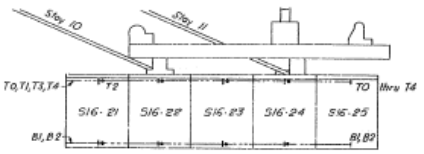

PHASE 26

(A) ADVANCE BEAM AND WINCH TO SEGMENTS S16-24
(B) LIFT SEGMENTS S16-25 FROM BARGE
(C) COUPLE AND STRESS P.T. BARS T1 AND B2 IN SEGMENTS S16-25
(D) COUPLE AND STRESS P.T. BARS T0, T2, T3, T4 IN SEGMENTS S16-25
(E) COUPLE AND STRESS P.T. BAR B1 IN SEGMENTS S16-25

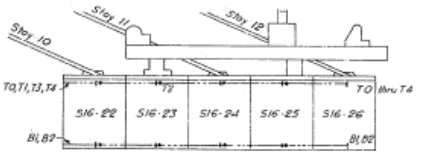

PHASE 27

(A) ADVANCE BEAM AND WINCH TO SEGMENTS S16-25
(B) LIFT SEGMENTS S16-26 FROM BARGE
(C) COUPLE AND STRESS P.T. BARS T1 AND B2 IN SEGMENTS S16-26
(D) COUPLE AND STRESS P.T. BARS T0, T2, T3, T4 IN SEGMENTS S16-26
(E) COUPLE AND STRESS P.T. BAR B1 IN SEGMENTS S16-26
(F) LIFT DELTA FRAME OF SEGMENTS S16-26
(G) PLACE DRY PACKED MORTAR BETWEEN DELTA FRAME AND SEGMENT WEBS
(H) POUR CIP CONCRETE CLOSURE IN TOP SLAB FOR SEGMENTS S16-25 AND S16-26
(I) WHEN THE CIP CONCRETE REACHES A MINIMUM COMPRESSIVE STRENGTH OF 3500 PSI, STRESS THE 12X0.6" STRAND TENDON OF THE DELTA FRAME AND ALL TRANSVERSE CONTINUITY POST TENSIONING OF SEGMENTS S16-25 AND S16-26
(J) REMOVE P.T. BARS B2 FROM SEGMENTS S16-07 AND S16-08
(K) ASSEMBLE AND STRESS STAY 12 TO 1480 KIPS
(L) REMOVE P.T. BARS T2 FROM SEGMENTS S16-21 AND S16-22
REMOVE P.T. BARS T3 AND T4 FROM SEGMENTS S16-17 AND S16-18
REMOVE P.T. BARS T0 AND T1 FROM SEGMENTS S16-13 AND S16-14

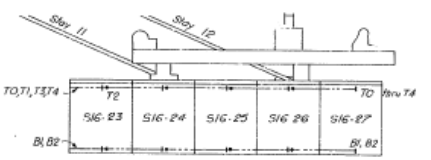

PHASE 28

DETAILS OF THE SEAL SHOWN ON THIS SHEET ARE NOT REQUIRED FOR SUBMITTAL OF THE CONTRACT PLANS ON BASIS DESCRIBED IN THE SPECIAL PROVISIONS

JR-827

(A) ADVANCE BEAM AND WINCH TO SEGMENTS S16-26
(B) LIFT SEGMENTS S16-27 FROM BARGE
(C) COUPLE AND STRESS P.T. BARS T1 AND B2 IN SEGMENTS S16-27
(D) COUPLE AND STRESS P.T. BARS T0, T2, T3, T4 IN SEGMENTS S16-27
(E) COUPLE AND STRESS P.T. BAR B1 IN SEGMENTS S16-27

The Equipment Schematics are for Information Only
See Sheet 10 for General Notes.

N.B.L. & S.B.L. RTE. 295 OVER JAMES RIVER

MAIN SPAN
ERECTION SEQUENCE V

Designed by LP
Drawn by JR
Checked by MG

Figg and Muller Engineers, Inc.
Tallahassee, Fl. / Paris, Fr. / Washington, D.C. / Denver, Co.

No scale

November, 1984

260-32

Sheet 332 of 1339

FHWA REGION	STATE	FEDERAL AID ROUTE	FEDERAL AID PROJECT	STATE ROUTE	STATE PROJECT	SHEET NO
3	VA.	95		295	0095-020-101,PE 101,RW[illegible]	15(333)

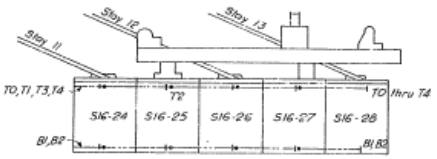

PHASE 29

(A) ADVANCE BEAM AND WINCH TO SEGMENTS S16-27
(B) LIFT SEGMENTS S16-28 FROM BARGE
(C) COUPLE AND STRESS P.T. BARS T1 AND B2 IN SEGMENTS S16-28
(D) COUPLE AND STRESS P.T. BARS T0, T2, T3, T4 IN SEGMENTS S16-28
(E) COUPLE AND STRESS P.T. BAR B1 IN SEGMENTS S16-28
(F) LIFT DELTA FRAME OF SEGMENTS S16-28
(G) PLACE DRY PACKED MORTAR BETWEEN DELTA FRAME AND SEGMENT WEBS
(H) POUR CIP CONCRETE CLOSURE IN TOP SLAB FOR SEGMENTS S16-27 AND S16-28
(I) WHEN THE CIP CONCRETE REACHES A MINIMUM COMPRESSIVE STRENGTH OF 3500 PSI, STRESS THE 12X0.6" STRAND TENDON OF THE DELTA FRAME AND ALL TRANSVERSE CONTINUITY POST TENSIONING OF SEGMENTS S16-27 AND S16-28
(J) REMOVE P.T. BARS B2 FROM SEGMENTS S16-09 AND S16-10
(K) ASSEMBLE AND STRESS STAY 13 TO 1580 KIPS
(L) REMOVE P.T. BARS T2 FROM SEGMENTS S16-25 AND S16-24
REMOVE P.T. BARS T3 AND T4 FROM SEGMENTS S16-19 AND S16-20
REMOVE P.T. BARS T0 AND T1 FROM SEGMENTS S16-15 AND S16-16

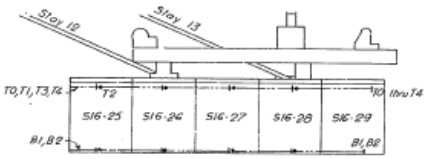

PHASE 30

(A) ADVANCE BEAM AND WINCH TO SEGMENTS S16-28
(B) LIFT SEGMENTS S16-29 FROM BARGE
(C) COUPLE AND STRESS P.T. BARS T1 AND B2 IN SEGMENTS S16-29
(D) COUPLE AND STRESS P.T. BARS T0, T2, T3, T4 IN SEGMENTS S16-29
(E) COUPLE AND STRESS P.T. BAR B1 IN SEGMENTS S16-29

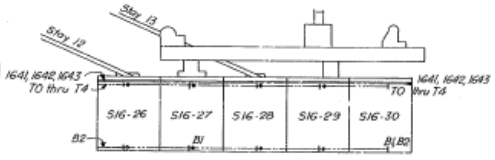

PHASE 31

(A) ADVANCE BEAM AND WINCH TO SEGMENTS S16-29
(B) LIFT SEGMENTS S16-30 FROM BARGE
(C) COUPLE AND STRESS P.T. BARS T1 AND B2 IN SEGMENTS S16-30
(D) COUPLE AND STRESS P.T. BARS T0, T2, T3, T4 IN SEGMENTS S16-30
(E) COUPLE AND STRESS P.T. BAR B1 IN SEGMENTS S16-30
(F) LIFT DELTA FRAME OF SEGMENTS S16-30
(G) PLACE DRY PACKED MORTAR BETWEEN DELTA FRAME AND SEGMENT WEBS
(H) POUR CIP CONCRETE CLOSURE IN TOP SLAB FOR SEGMENTS S16-29 AND S16-30
(I) WHEN THE CIP CONCRETE REACHES A MINIMUM COMPRESSIVE STRENGTH OF 3500 PSI, STRESS THE 12X0.6" STRAND TENDON OF THE DELTA FRAME AND ALL TRANSVERSE CONTINUITY POST TENSIONING OF SEGMENTS S16-29 AND S16-30
(J) STRESS TENDONS 1641, 1642 AND 1643
(K) REMOVE P.T. BARS B1 FROM SEGMENTS S16-15 THROUGH S16-26
REMOVE P.T. BARS B2 FROM SEGMENTS S16-11 THROUGH S16-24
REMOVE P.T. BARS T0 AND T1 FROM SEGMENTS S16-17 AND S16-18

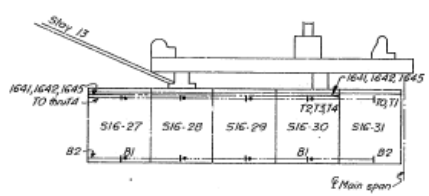

PHASE 32

(A) ADVANCE BEAM AND WINCH TO SEGMENTS S16-30
(B) LIFT SEGMENTS S16-31 FROM BARGE
(C) COUPLE AND STRESS P.T. BARS T1, B2 AND T0 IN SEGMENTS S16-31
(D) POUR CIP CONCRETE CLOSURE IN TOP SLAB OF SEGMENTS S16-31
(E) WHEN THE CIP CONCRETE REACHES A MINIMUM COMPRESSIVE STRENGTH OF 3500 PSI, STRESS ALL TRANSVERSE CONTINUITY POST-TENSIONING OF SEGMENTS S16-31

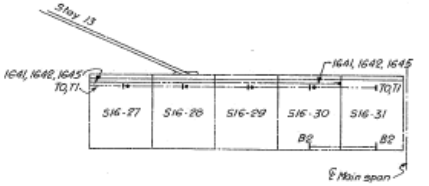

PHASE 33

(A) REMOVE BEAM AND WINCH FROM CANTILEVER, TRANSPORT TO PIER 17, AND BEGIN FOR PROGRESSIVE CANTILEVER CONSTRUCTION
(B) REMOVE ALL P.T. BARS B1
REMOVE P.T. BARS B2 FROM SEGMENTS S16-25 THROUGH S16-29
REMOVE ALL P.T. BARS T2, T3 AND T4
REMOVE P.T. BARS T0 AND T1 FROM SEGMENTS S16-19 THROUGH S16-25

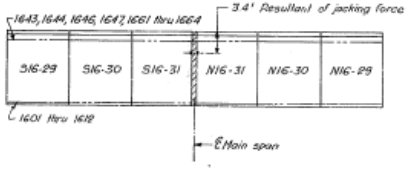

PHASE 34 - MAIN SPAN CLOSURE

(A) PROGRESSIVE CANTILEVER CONSTRUCTION OF PIER 17 IS COMPLETED THROUGH PHASE 32.
(B) REMOVE P.T. BARS IN SEGMENTS S14-07 THROUGH S14-09 AND IN SEGMENTS N18-06 THROUGH N18-08
(C) JACK AT CLOSURE BETWEEN PIER 16 AND 17 CANTILEVERS BY APPLYING A FORCE OF 150K PER WEB (600 KIPS TOTAL). THE JACKS SHALL BE PLACED SUCH THAT THE RESULTANT OF THE JACKING FORCE LIES 3.4 FEET BELOW THE TOP OF THE TOP SLAB
(D) SHIM AND POUR CLOSURE JOINT
(E) WHEN CONCRETE OF CLOSURE JOINT REACHES A MINIMUM COMPRESSIVE STRENGTH OF 2500 PSI, STRESS, IN THE ORDER GIVEN, THE FOLLOWING TENDONS:
1612 - 1644 AND 1647 - 1664 - 1611 - 1610 - 1609
1645 - 1646 - 1663 - 1662 - 1661
1608 - 1607 - 1606 - 1605 - 1604 - 1603 - 1602 - 1601
(F) REMOVE ALL P.T. BARS T0,T1, AND B2.

JR-826

N.B.L. & S.B.L. RTE. 295 OVER JAMES RIVER

MAIN SPAN ERECTION SEQUENCE VI

The Equipment Schematics are for Information Only See Sheet 10 for General Notes.

DESIGNED BY
DRAWN BY
CHECKED BY

Figg and Muller Engineers, Inc.
Tallahassee, Fl. / Paris, Fr. / Washington, D.C. / Denver, Co.

No scale

November, 1984

260-32
Sheet 233 of 329